Progress In Electromagnetics Research, Vol. 170, 17–62, 2021

Advanced Progress on $\chi^{(3)}$ Nonlinearity in Chip-Scale Photonic Platforms

Zhe Kang[1, 2, #], Chao Mei[3, #], Luqi Zhang[4], Zhichao Zhang[4], Julian Evans[2], Yujun Cheng[4], Kun Zhu[5], Xianting Zhang[5], Dongmei Huang[5], Yuhua Li[6], Jijun He[7], Qiang Wu[8], Binbin Yan[4], Kuiru Wang[4], Xian Zhou[3], Keping Long[3], Feng Li[5], Qian Li[9], Shaokang Wang[10], Jinhui Yuan[3, 4, *], P. K. A. Wai[5], and Sailing He[1, 2, *]

(*Invited Review*)

Abstract—$\chi^{(3)}$ nonlinearity enables ultrafast femtosecond scale light-to-light coupling and manipulation of intensity, phase, and frequency. $\chi^{(3)}$ nonlinear functionality in micro- and nano-scale photonic waveguides can potentially replace bulky fiber platforms for many applications. In this Review, we summarize and comment on the progress on $\chi^{(3)}$ nonlinearity in chip-scale photonic platforms, including several focused hot topics such as broadband and coherent sources in the new bands, nonlinear pulse shaping, and all-optical signal processing. An outlook of challenges and prospects on this hot research field is given at the end.

1. INTRODUCTION

The invention of the laser by Maiman in 1960 gave rise to the unprecedented development of the old subject of optics [1]. As one of the largest branches of optics, nonlinear optics which describes the interaction between light and matter has attracted countless research efforts. When the medium whose inner structure is centrosymmetric is exposed to high intensity light, $\chi^{(3)}$ nonlinear processes are the lowest order. This process originates from the electronic polarization caused by the electric-field component of the light, which can be mathematically given by [2]

$$\mathbf{P} = \varepsilon_0 \left(\chi^{(1)} \cdot \mathbf{E} + \chi^{(2)} : \mathbf{EE} + \chi^{(3)} \vdots \mathbf{EEE} + \dots \right) \tag{1}$$

where ε_0 is the dielectric constant in vacuum; E is the complex electric-field amplitude; $\chi^{(1)}$ is the tensor of rank 2 which denotes the linear response to E; $\chi^{(2)}$ and $\chi^{(3)}$ are tensors of ranks 3 and 4 which define

---

Received 21 December 2020, Accepted 13 January 2021, Scheduled 15 January 2021

* Corresponding authors: Jinhui Yuan (yuanjinhui81@bupt.edu.cn), Sailing He (sailing@jorcep.org).

[1] Ningbo Research Institute, Zhejiang University, Ningbo 315000, China. [2] Centre for Optical and Electromagnetic Research, National Engineering Research Center for Optical Instruments, Zhejiang University, Hangzhou 310000, China. [3] Research Center for Convergence Networks and Ubiquitous Services, University of Science and Technology Beijing, Beijing 100083, China. [4] State Key Laboratory of Information Photonics and Optical Communications, Beijing University of Posts and Telecommunications, Beijing 100876, China. [5] Photonics Research Centre, Department of Electronic and Information Engineering, The Hong Kong Polytechnic University, Hung Hom, Hong Kong, China. [6] Department of Physics, City University of Hong Kong, Hong Kong, China. [7] Swiss Federal Institute of Technology Lausanne (EPFL), 1015 Lausanne, Switzerland. [8] Department of Physics and Electrical Engineering, Northumbria University, Newcastle upon Tyne, NE1 8ST, United Kingdom. [9] School of Electronic and Computer Engineering, Peking University, Shenzhen 518055, China. [10] Department of Computer Science and Electrical Engineering, University of Maryland, Baltimore County, Baltimore, MD 21250, USA.

# These authors contributed equally to this work.

the second-order and third-order nonlinear responses, respectively. Compared to the $\chi^{(2)}$ nonlinearity, the excitation of $\chi^{(3)}$ nonlinearity generally requires higher intensity. $\chi^{(3)}$ nonlinearity has much richer physical dynamics since it is higher order. In this paper, we will be focused on the $\chi^{(3)}$ nonlinearity. Basic effects that relate to the $\chi^{(3)}$ nonlinearity include self-phase modulation (SPM), cross-phase modulation (XPM), third-order harmonic generation, four-wave mixing (FWM), two-photon absorption (TPA), stimulated Raman scattering (SRS), stimulated Brillouin scattering (SBS), etc. These effects are induced by different kinds of light-matter interaction. Figure 1 illustrates the processes of light-matter interaction. An input field with specific frequency encounters the molecule and then generates a new field with different frequencies. Taking the nondegenerate FWM as an example, the input frequencies of ω_1 and ω_2 can emit two new frequencies of ω_3 and ω_4. Nevertheless, the energy and momentum are conserved in this process, which indicates the FWM is a Hamilton process. In contrast, some other effects, such as SRS and SBS, only obey momentum conservation law but not energy conservation, and a part of energy is transferred to the mediated phonons.

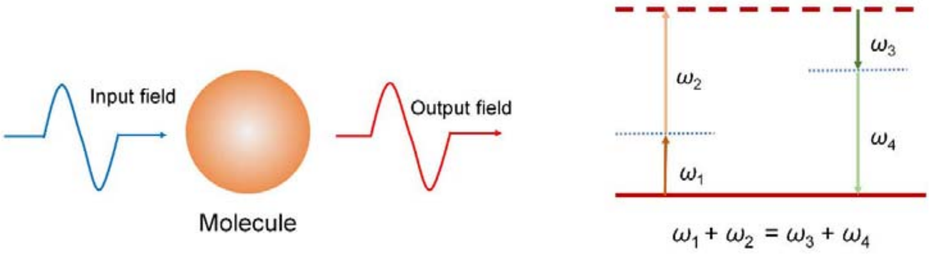

(a) (b)

Figure 1. (a) Skeptical demonstration of light-matter interaction, and (b) typical process of FWM.

SRS was the first studied nonlinear effects in 1962, soon after the invention of laser [3]. After that, Maker et al. found that the refractive indexes of liquids are changed with the intensity of input field [4]. The phenomena of SBS [5] and FWM [6] were observed in 1964 and 1966, respectively. At that time, most nonlinear effects were studied in bulk media, such as liquids, or gases until emergence of optical fiber in 1966 [7]. Optical fiber, especially the low-loss fiber, is an ideal waveguide in which light can directionally propagate. As a result, the light-matter interaction is prolonged in long fibers. Ippen demonstrated the first Raman laser in CS_2-core fiber in early 1970 [8]. A lot of other nonlinear effects were then discovered in silica fibers such as the SBS [9], FWM [10], SPM [11], and XPM [12]. Understanding these nonlinear effects is very important because it then inspired people to theoretically [13] and experimentally [14] find temporal optical soliton. Soliton is one of the most important concepts in nonlinear optics because it stands for an exact balance between SPM and group-velocity dispersion (GVD). This kind of temporally localized wave packet is similar to the time-domain discrete pulse trains in a mode-locked laser. Soliton lasers were then widely studied in optical fibers [15] after the advent of optical solitons. The temporal stability of soliton makes it an ideal tool for communication transmission. The bandwidth-limited soliton communication system was built up [16] in 1986. A natural question is what would happen if the exact balance of the soliton is broken? It has been shown that in this case, other nonlinear phenomena such as dispersive wave [17], soliton fission [18], soliton self-frequency shift (SSFS) [19] can occur. These nonlinear effects could jointly lead to supercontinuum (SC) generation [20]. The property of SC strongly depends on GVD profiles of the waveguides. Unfortunately, conventional single-mode fiber (SMF) cannot provide enough flexibility in GVD engineering because the core diameter of SMF is too large ($8 \sim 10\,\mu\text{m}$) compared with the wavelength which is pumped at the near-infrared region (NIR). In such waveguides, the material dispersion which locates at the normal dispersion region is stronger than geometrical dispersion. To compensate the material dispersion, one needs to reduce the transverse size of SMF to a level that is comparable to pump wavelength. The successful fabrication of photonic crystal fiber (PCF) in 1995 has solved this problem [21]. The core diameter of PCF can be engineered to be only $1 \sim 2\,\mu\text{m}$. The transverse microstructure of PCF can be arranged periodically over much of the cross-section, which provides another possibility to engineer the dispersion by changing the transverse size or structure. So far, PCF has many variants, such as photonic-bandgap fibers [22], holey fibers [23], hole-assisted fibers [24], Bragg fibers [25] and anti-resonant fibers [26]. The materials which are used to make up PCF are also not limited to SiO_2. Gas and liquid with various dispersion profiles are also employed for specific dispersion design. The abundant selection of constituent materials, designable transverse size and structure allow PCFs to open many possibilities in the study of nonlinear optics.

With the rapid development of micro/nano manufacturing technology, waveguide with subwavelength transverse size becomes possible. Recently, the study of nonlinear optics in the micro/nano photonic waveguide (MNPW) has attracted broad interest [27]. Different from cylindrical waveguides such as SMF or PCF, MNPW not only has a smaller transverse size, but also the ability to integrate with photonic circuits. More importantly, MNPWs have the advantage of low energy consumption, flexible dispersion engineering, low cost, wide transparent window, and high nonlinear refractive index. According to the difference in transverse geometrical structure, MNPWs can be classified as ridge (inverse ridge), strip, channel and slot waveguides. Longitudinally propagating electric field in MNPWs can be tightly confined within a rather small area due to the higher refractive index contrast. For example, the refractive index contrast of SMF is almost 100 times smaller than that of a silicon-on-insulator (SOI) waveguide. The effective mode area A_{eff} of MNPW is much smaller, which results in the enhanced light-matter interaction [28]. The nonlinear coefficient $\gamma = 2\pi n_2/(\lambda A_{eff})$ is thus increased, where n_2 is the nonlinear refractive index. While the optical field propagating in SMFs is restricted to the core layer, any desired propagating layer can be achieved for MNPWs by the structure design. While the linear loss of MNPW is much larger than that of fibers, the waveguide length required by nonlinear effects is much shorter due to the large γ. Additionally, the linear loss of MNPWs can be mitigated with proper fabrication [29].

Figure 2 schematically shows the cross sections of typical MNPW waveguides. In contrast to the fiber-based waveguides, the flexible dispersion engineering of MNPWs is reflected in the diversity of transverse geometries with smaller scale down to sub-micrometers and nanometers levels. The dimensions of a microring is also shown in comparison with a coin. The transverse profile of MNPWs including ridge, strip, channel, and slot in Figure 2 means that it cannot be fabricated by simply tapering the preformed bar as for SMFs and PCFs. Techniques of micro/nano fabrication must be employed including the thermal oxidation, sputtering, chemical vapor deposition, flame hydrolysis deposition, ion-assisted deposition, spin-coating, sol-gel technique, etc. [30].

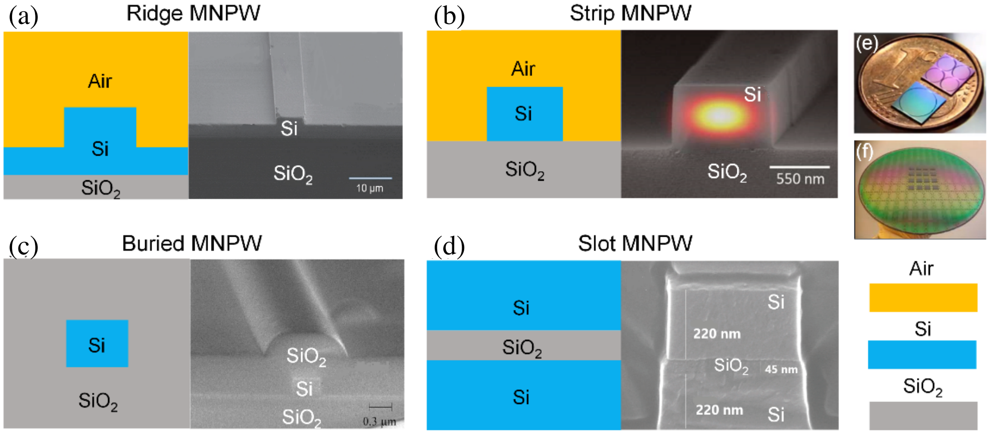

Figure 2. Schematic diagram (left panel) and SEM (right panel) of (a) a ridge MNPW, (b) a strip MNPW, (c) a buried MNPW and (d) a slot MNPW. (e) Microring chips together with 1-cent coin for size comparison, and (f) MNPWs integrated on a 12-inch Si wafer.

Typical $\chi^{(3)}$ nonlinear effects observed in SMFs or PCFs have also been found in MNPWs. For instance, Si waveguides have demonstrated SPM and XPM effects [31, 32]. However, compared with cylindrical waveguides, larger linear loss in MNPWs lowered the efficient of SPM and XPM effects. Si exhibits strong TPA and free-carrier absorption (FCA) at the telecom band [33]. Nonlinear absorptions can be explained by band-gap energy whose half value is smaller than the energy of a single photon at telecom band. As a result, two photons are absorbed for atomic transition. Although TPA effect can be utilized in pulse compressor [34], detector [35] and spectroscopy [36], it degrades the nonlinear efficiency. To avoid this, one method is shifting the pump wavelength from the telecom to mid-infrared region (MIR) to decrease the photon energy. Another method is to use alternative larger bandgap materials such as chalcogenide, highly doped silica, and Si_3N_4 waveguides which show negligible TPA or FCA at telecom band due to the larger band-gap [37]. The $\chi^{(3)}$ nonlinearity of silica fibers is essentially determined by the optical properties of SiO_2. Instead, a MNPW which could be made up by hybrid material ensembles such as Group IV and III-V elements offers versatile nonlinear functionalities. An additional advantage of Si-based MNPWs is the compatibility with complementary metal oxide semiconductor (CMOS) technology, which allows for inclusion in integratable photonic circuits. The application of Group IV elements in nonlinear optics has been reported, including the Si [38], Ge [39], SiGe alloy [40, 41], and Si_3N_4-based MNPWs [42]. For example, Kerr microcomb can be generated efficiently in miniaturized platforms such as Si_3N_4 microresonators [43–45]. Chalcogenide waveguides were also extensively studied because of its large nonlinear refractive index, broadband transparency and excellent thermal stability [46]. It has been used in the all-optical wavelength conversion [47], SC generation [48], and SPM effect [49]. The MNPWs based on III-V elements are also good candidates for nonlinear optics because of their large nonlinearity and broadband transparent window up to 20 μm. The devices based on III-V elements allow for electro-optic control. Among them, AlGaAs [50–52], GaInP [53], AlN [54], and GaN [55] have been widely studied. For example, octave-spanning coherent SC [56] and ultra-efficient frequency comb [57] could be experimentally generated in AlGaAs-on-insulator waveguides and microresonators, respectively.

In this review, we will focus on three hot topics built upon $\chi^{(3)}$ nonlinearity. The first is the development of coherent and broadband sources generation in the new bands presented in Section 2. It includes the SC and SC-based frequency comb generation, Kerr microcombs generation, and intermodal FWM. The second topic is the passive pulse shaping technique by means of $\chi^{(3)}$ nonlinearity, which will be presented in Section 3. Passive pulse shaping includes ultrashort pulse compression (PC), spectral compression (SPC), and parabolic pulse (PP) generation. Finally, Section 4 will cover the application of $\chi^{(3)}$ nonlinearity in all-optical signal processing. The progress on techniques such as all-optical analogy-digital conversion (ADC), logic gate, and radio frequency photonics on MNPWs will be reviewed in detail.

2. COHERENT AND BROADBAND SOURCES OPENED UP IN THE NEW BANDS

Invention and development of coherent sources in the near-infrared bands have led to revolutionary breakthrough in communications, biomedical science, high field physics, attosecond science, precision frequency metrology, etc. Building upon the remarkable success in the near-infrared band, the focus has naturally shifted to other new bands of light wave, i.e., the MIR region (2.5 ∼ 25 μm) known as "fingerprint" region of molecular with also two atmospheric transparent windows (3.5 ∼ 5 μm and 8 ∼ 14 μm) beneficial for remote sensing and Lidar, the visible region (VR) (0.39 ∼ 0.78 μm) for underwater optical communication and illumination, and even ultraviolet region (UVR) (0.01 ∼ 0.39 μm) for biomedicine. Figure 3 shows the optical spectrum ranges from UVR to MIR and typical applications at the new bands. Unfortunately, gain media in these new bands is very rare or even nonexistent. Moreover, the bandwidth of known gain media is rather narrow. For example, the gain bandwidths of Yb-doped and Er-doped mediums are only tens of nanometers with the center wavelengths of 1064 and 1550 nm, respectively. The gain media working in the MIR region are limited within 1.8 to 3.5 μm, as shown in Figure 3. There is no known gain media in VR, UVR, and deep MIR regions, meaning the sources in these new bands cannot be obtained by conventional lasing technology. In order to obtain the coherent sources at these gain-limited regions, one has to resort to the frequency conversion outside a laser cavity. Harnessing nonlinear frequency conversion to transfer frequency components from the well-developed bands becomes the only option.

Compared to the $\chi^{(2)}$-based nonlinearity such as sum and difference frequency generation, $\chi^{(3)}$-based nonlinearity, usually associated with soliton dynamics, is generally superior in conversion efficiency

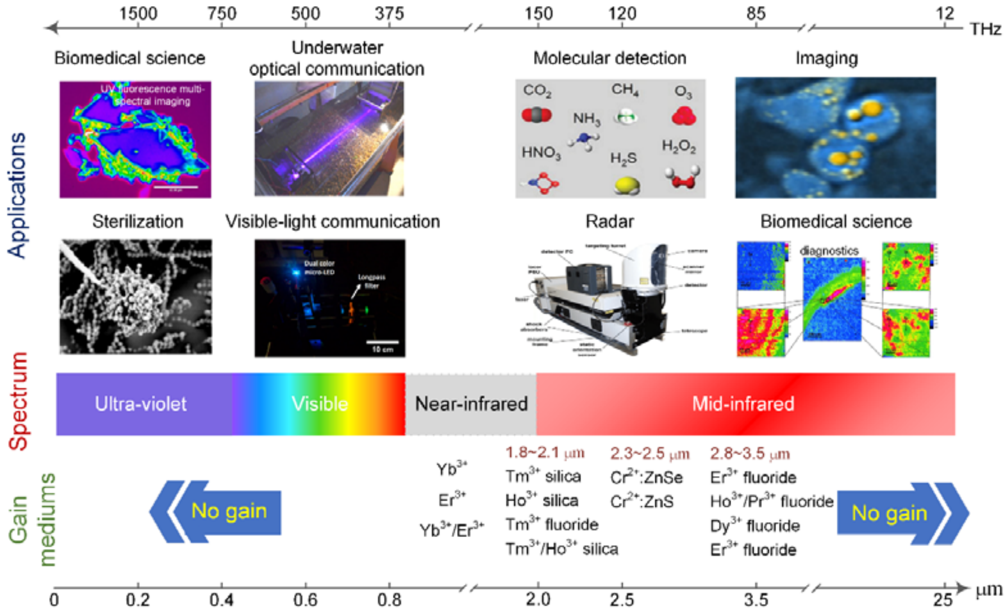

Figure 3. Optical spectrum ranging from UVR to MIR with the corresponding applications in the new bands, and the indication of existing bands with gain mediums.

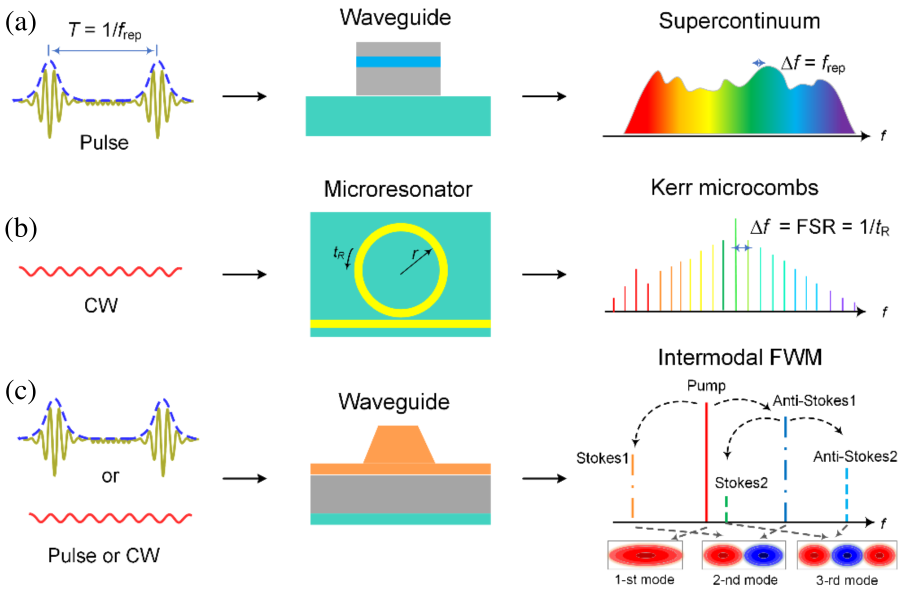

Figure 4. Schematic diagrams for the geneation of SC, Kerr microcombs, and intermodal FWM in chip-scale photonic platforms.

and achievable bandwidth. The schematic diagrams of these techniques are shown in Figure 4. Specifically, the techniques to be focused include SC generation, Kerr microcomb generation, and intermodal FWM. It has been proved that the spectral properties like bandwidth, intensity, as well as coherence can be completely manipulated by tailoring the dispersion and nonlinearity of MNPWs.

SC generation will occur when a strong continuous or pulse source passes through a nonlinear medium. Due to the interaction between linear dispersion and nonlinear effects (such as SPM, XPM, SRS, FWM, MI, soliton fission, self-steepening, etc.), new frequency components are generated to expand the input spectrum. This makes materials with large nonlinear coefficients and wide transparent window desirable. Soliton pulse pumping in the anomalous dispersion region is usually used for ultra-broadband SC generation because the associated soliton fission significantly helps the spectrum broadening. To guarantee a high degree of coherence of spectrum, the pulse width of soliton should be shortened to hundreds of femtoseconds (better $< 100\,\mathrm{fs}$) to construct the scenario of soliton fission dominating the MI effect. Through reasonable dispersion engineering and pump condition selecting, SC could cover from UVR to MIR by more than one octave along with high degree of coherence.

For the generation of Kerr microcomb, high finesse optical microresonator continuously driven by a continuous-wave (CW) pump laser is typically employed. Although pulse driving methods are also available, a CW source is sufficient. This is much different from SC generation in straight MNPWs via injection of pulse with high peak power [58]. Hyper-parametric oscillation (also called cascaded FWM) arises through Kerr nonlinearity and determines broadband frequency combs generation. By scanning either pump frequency or cavity resonance to achieve an effective red-detuned condition, multi-states, e.g., MI, chaotic, and even dissipative Kerr soliton (solitons superimpose on a CW background) states can be achieved. The stable soliton state is what one desires in Kerr microcombs. In particular, the single soliton microcomb shows temporally near few-cycle pulse, broadband and smooth hyperbolic secant shape spectrum in the frequency domain. The coherence of spectrum can be well maintained in this scenario. Nevertheless, several disadvantages including thermal noise destabilization and difficulties in fabricating ultrahigh Q-factor microresonators still wait for better solutions.

In contrast to conventional intramodal FWM that occurs amongst all photons in the same mode, intermodal FWM occurs among all photons in different modes. While the former one has been extensively studied, the latter one has been studied rarely. As most materials have normal dispersion in UVR, VR, or deep MIR, it is impossible to achieve phase matching in these bands for conventional intramodal FWM. In this sense, intermodal FWM in which phase matching condition among different modes does not restricted in anomalous dispersion regime is an excellent alternative. Moreover, while the maximum efficiency of intramodal FWM is achieved near the pump wavelength, the one of intermodal FWM could be achieved far away from the pump wavelength, meaning a broadband range can be reached. Intermodal FWM not only has the advantages in phase matching, but also possesses higher flexibility and better spectral conversion efficiency.

2.1. Supercontinuum and Frequency Comb Generation

Supercontinuum sources are desirable because of their ability in maintaining high spectral brightness in a broad spectral range. SC is particularly exciting for optical metrology, microscopy, optical frequency synthesis, optical coherence tomography, molecular spectroscopy, biomedical science, etc. [59].

Mathematically, SC generation is governed by the generalized nonlinear Schrödinger equation (GNLSE) under the slow varying envelope approximation. For the operation bands in which the half band-gap of nonlinear material is below the photon energy, nonlinear multi-photon absorption (MPA) has to be considered. In addition, for specific semiconductor materials like Si, free carrier induced attenuation (FCA) and dispersion (FCD) also have to be considered. The modified GNLSE is given by [60],

$$\begin{aligned} u_z(z,T) \;=\; & -\frac{1}{2}\left(\alpha+\alpha_{FCA}\right)u+\frac{i\omega_0 n_{FCD}}{c}u+\sum_{k\geq 2} i^{k+1}\frac{1}{k!}\beta_k u_T^{(k)} \\ & +\left(i\gamma-\sum_{n=2}^{4}\frac{1}{n}A_{\mathit{eff}}^{-(n-1)}\beta_{nPA}\left|u\right|^{2(n-2)}\right)\times\left(1+i\tau_s\partial_T\right) \\ & \times\left[u(z,T)\int_0^{\infty}R(t)\left|u(z,T-t)\right|^2dt\right] \end{aligned} \tag{2}$$

where $u(z,T)$ is the envelope of electric field, α the linear loss, and β_k the k-th order dispersion coefficient related to the Taylor series expansion of propagation constant $\beta(\omega)$ at the center frequency ω_0. γ is the nonlinear coefficient, $\tau_s = 1/\omega_0$ the optical shock time connecting with the self-steepening effect, and $R(t)$ the Raman response function. Among them, β_{nPA} represents the n-photon absorption coefficient, and the refractive index changes caused by FCA and FCD are expressed as $\alpha_{FCA} = \sigma N_c$ and $n_{FCD} = \zeta N_c$, respectively. The free carrier coefficients connected with the waveguide materials are represented as σ and ζ, and N_c is the free carrier density. The performance of SC is evaluated by measuring the spectral bandwidth and coherence. Highly coherent SC sources are of significant interest for precision spectroscopy, high resolution optical tomography, Raman spectroscopy, etc. These applications demand the low phase fluctuation of spectrum and broad bandwidth. Mathematically, the interpulse coherence is calculated by [61],

$$g_{12}^{(1)}\left(\lambda, t_1 - t_2\right) = \left| \frac{\left\langle u_i^*\left(\lambda, t_1\right) u_j\left(\lambda, t_2\right)\right\rangle_{i \neq j}}{\sqrt{\left\langle \left|u_i\left(\lambda, t_1\right)\right|^2 \right\rangle \left\langle \left|u_j\left(\lambda, t_2\right)\right|^2 \right\rangle}} \right| \tag{3}$$

where $u(\lambda)$ stands for the amplitude of SC in the frequency domain, and the subscripts i and j represent the pulses at different time slots of t_1 and t_2 inside a pulse train, respectively. The expressions in the angle bracket represent the statistical average of a certain number of shot-to-shot SC pairs with power and phase noises. Different from the interpulse coherence that describes spectral phase fluctuation of a pulse train, the recently developed intrapulse coherence provides a method to measure the spectral phase fluctuation of a single pulse. The intrapulse coherence is given by [62]

$$\Gamma = \frac{\left|\left\langle u_i^2\left(2\lambda\right) u_i^*\left(\lambda\right)\right\rangle\right|}{\left\langle \left|u_i^2\left(2\lambda\right) u_i^*\left(\lambda\right)\right| \right\rangle}. \tag{4}$$

Equation (4) measures the fluctuation of spectral phase difference between a spectral component and its doubling-frequency counterpart. This intrapulse coherence directly estimates the quality of $f - 2f$ self-referencing product, which can be used to control the carrier-envelope offset (f_{CEO}). It has been numerically proved that a SC source with excellent interpulse coherence might has a poor intrapulse coherence [63].

Coherent UVR to VR SC generation has been reported in silica ridge waveguides. Different from fiber platforms, the silica waveguide arrays provide a wide range of emission wavelength choices on a single and compact chip. Oh et al. experimentally demonstrated efficient and coherent dispersive wave generation from UVR to VR in silica waveguides with pumping wavelength of 830 nm [64]. The waveguide array structure and experimental results are shown in Figure 5.

Coherent SC generation can be extended from VR to NIR in various nonlinear materials. In 2019, Liu et al. experimentally generated a VR to NIR SC spanning from 600 to 1050 nm in AlN waveguides [65]. Lafforgue et al. experimentally exploited nitrogen-rich Si_3N_4 waveguides to generate an octave SC spanning from 400 to 1600 nm [66]. Numerical simulations indicated high interpulse coherence of generated SC. If the pump pulse is shorter than 100 fs [59, 67], generated SC would have high interpulse coherence. This conclusion has been confirmed by some experiments operating in the NIR region. For example, Johnson et al. demonstrated the SC generation spanning more than 1.4 octaves in a Si_3N_4 waveguide using sub-100-fs pulses at 1 µm pumping wavelength [68]. A spectral interferometer was used to verify the high degree of interpulse coherence over the majority of spectral bandwidth. In 2017, Okawachi et al. demonstrated a novel approach to produce coherent and directional SC by using cascaded dispersive waves [69]. The scheme is achieved by dispersion engineering in Si_3N_4 waveguides pumped at 1050, 1300 and 1400 nm, respectively. By performing direct detection of the carrier-envelope-offset frequency of femtosecond pump source using an $f - 2f$ interferometer, the coherence properties of generated SC are experimentally confirmed. Different from previous works conducted on SiO_2, Si or Si_3N_4 platforms, Kuyken et al. recently demonstrated SC generation on the AlGaAs-on-insulator platform [70]. The pumped wavelength is located at telecom wavelengths (1555 nm). Superior interpulse coherence within 1450–1750 nm is experimentally validated. Chalcogenide is another suitable substitute for SC generation in the NIR. For instance, Tremblay et al. fabricated low propagation loss $Ge_{23}Sb_7S_{70}$ waveguides (0.56 dB/cm) in a wafer scale process [71]. By careful engineering of the waveguide dispersion, coherent and octave-spanning SC pumped at 1.55 µm with picojoule-level energy is generated. Dave et al. demonstrated the generation of an octave-spanning SC in III-V membrane waveguides on a Si substrate [72]. The waveguide is pumped by a 1550-nm femtosecond source, and the generated SC is measured to be highly coherent.

MIR coherent and broadband SC generation is another hot topic due to its rich application in trace gas sensing, LIDAR, biomedical imaging, etc. In 2018, Singh et al. demonstrated octave-spanning and

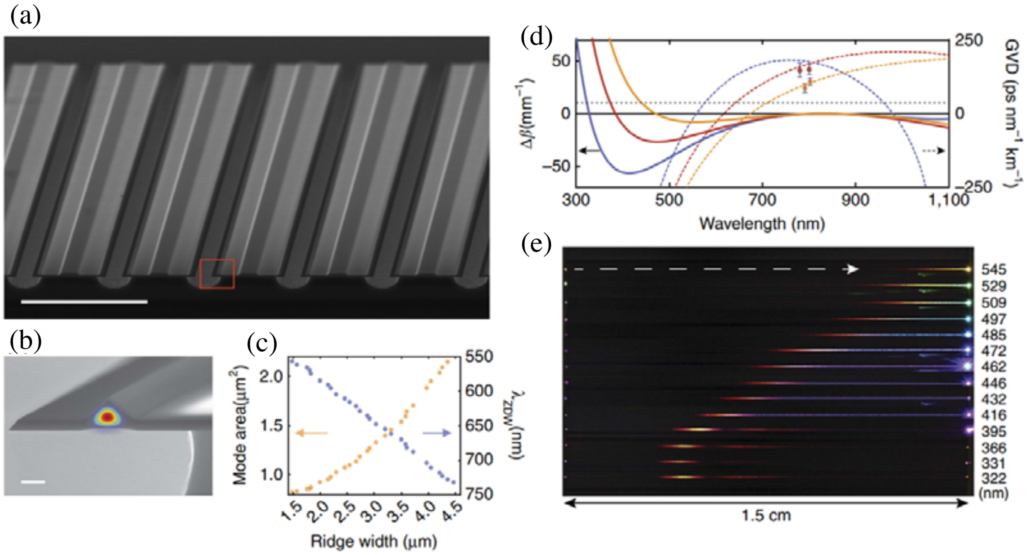

Figure 5. Phase matching condition and direct observation of dispersive wave generation in silica ridge waveguides. (a), (b) SEM images of an array of silica ridge waveguides on a Si chip. The red box in (a) contains a silica waveguide whose cross section is shown in (b); the cross section is superimposed with the calculated mode profile of the TM mode at a wavelength of 830nm. (c) Calculated mode area and zero dispersion wavelength are plotted as the ridge base width varies. (d) Calculated GVD (dashed lines) and phase-matching parameter (solid lines) for dispersive wave generation in TM polarization are plotted as the wavelength varies. Blue, red, and yellow solid and dashed lines correspond to mode areas of 0.83, 1.03, 1.69 mm^2, respectively. (e) UVR-VR dispersive wave generation in a Si chip containing an array of waveguides with varying mode area [64]. Copyright 2017 Nature Publishing Group.

coherent SC generation in SOI from 1.06 μm to beyond 2.4 μm [73]. The coherence of generated SC is measured to be more than an octave. Suspended waveguide structures are promising for deep-MIR SC generation because there is an air gap as the buffer layer between light-guiding region and substrate. As a result, strong mode confinement eliminates mode-leaking loss, and the limitation of transparency window caused by substrate material can be overcome. So far, suspended MNPWs on several material platforms with air gap have been fabricated and utilized for deep-MIR SC generation. For example, Kou et al. experimentally used a suspended rib Si waveguide to achieve a broadband SC spanning from 2 to 5 μm in 2018 [74]. Chiles et al. demonstrated a 2.3 $\sim$ 6.5 μm broadband SC by using a suspended AlGaAs waveguide [75] in 2019. At the same year, Nader et al. achieved an ultra-broadband SC spanning from 2 to 8 μm by using a suspended Si waveguide [76]. The deeply extended SC source was successfully utilized for on-chip dual comb spectroscopy. Figure 6 shows several fabricated suspended platforms for deep-MIR SC generation. MIR SC generation on MNPWs that are not suspended was also reported. The spectral extension in this scenario is mainly limited by the transparency of the substrate. In 2014, Lau et al. experimentally demonstrated coherent octave-spanning MIR SC generation in Si-based MNPWs [77]. They also numerically showed that MPA and FCA are not detrimental to SC generation in the MIR region. In 2016, Xie et al. demonstrated a more than 1.5 octave-spanning and coherent MIR SC covering 1.5 to 3.6 μm by pumping a so-called As_2S_3-silica “double-nanospike” waveguide [78]. In 2018, Sinobad et al. demonstrated an octave SC generation on a $Si_{0.6}Ge_{0.4}$ waveguide [79]. The spectrum of the SC generated covered from 3 to 8.5 μm, almost reaching the limit of Si transparency. In 2019, Sinobad et al. demonstrated coherent and an octave-spanning broad MIR SC generation on an air-cladded SiGe-on-Si waveguide [80]. At the extreme ends of spectrum, high spectral density and coherence can be obtained after dispersion engineering. Theoretical works also contributed to the design and manipulation of deep-MIR SC generation targeted at suspended MNPWs. For example, Yang et al. numerically utilized 700-fs pump pulses with a low peak power of 400 W to pump a suspended Ge-on-Si waveguide at 6.57 μm wavelength [81]. The SC generated was confirmed to span from 2 to 12 μm

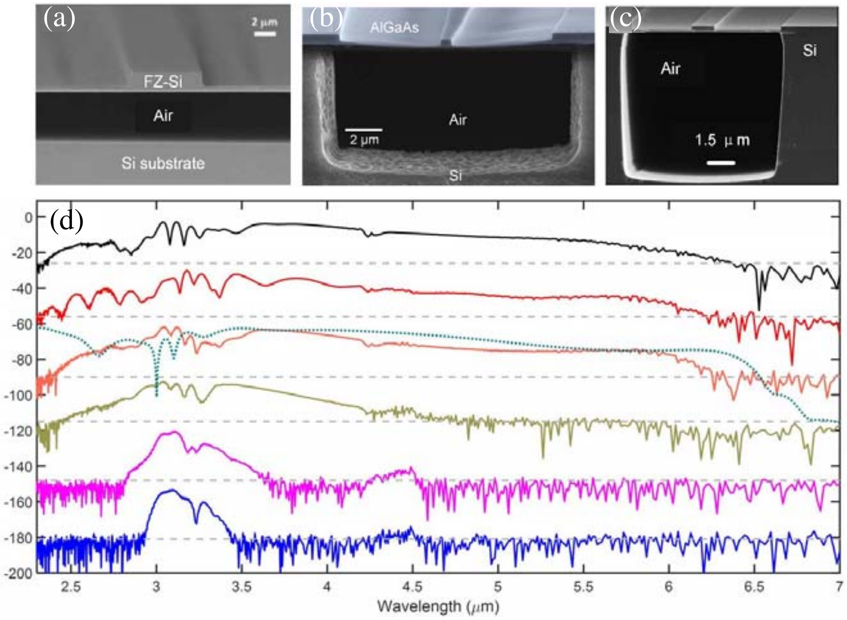

Figure 6. (a) (b) (c) SEM images of suspended waveguides from [74–76], respectively. (d) SCs when the pump wavelength is 3060 nm, experimentally measured spectra with different waveguide-coupled pulse energies (solid curves), and simulated spectrum at 45 pJ waveguide-coupled pulse energy (dotted curve), with a trace-to-trace offset of 30 dB [75]. Copyright 2018 & 2019 OSA.

with excellent coherence in the whole spectrum range. In 2017, Yuan et al. numerically studied SC generation in a 4-mm-long suspended Ge-membrane ridge waveguide pumped by a 180-fs pulse of peak power of 800 W and central wavelength of 4.8 μm [82]. Generation of coherent and ultra-broadband MIR SC spanning from 1.96 to 12 μm is studied. In 2018, Jing et al. numerically studied coherent and broadband SC generation in a 3.1-mm-long suspended As_2S_3 ridge waveguide pumped by a pulse source with a peak power of 450 W [83]. The generated SC covers from 1.0 to 5.6 μm. In 2019, Cheng et al. numerically studied the combination of self-similar PC and coherent SC generation in a specially designed suspended Si waveguide tapers [84]. Simulation results showed that a 1-ps pulse was perfectly compressed to 47.06 fs first, and then used for highly coherent and broadband MIR SC generation. In 2019, Li et al. numerically studied multi-octave MIR SC and frequency comb generation in a suspended As_2Se_3 ridge waveguide [85]. The generated SC spectrum could cover $1.76 \sim 14.42$ μm (more than three octaves) and had excellent coherence. In 2020, Lai et al. numerically designed a T-type Ge waveguide with the all-normal dispersion profile for MIR SC and frequency comb generation [86].

Some recent works show that ultrabroad SC that covers multi-bands from UVR to MIR can be generated by dispersive wave assistance in specially designed MNPWs. In 2019, Yu et al. experimentally demonstrated coherent two-octave SC generation covering $400 \sim 2400$ nm in a 0.5-cm-long x-cut nano-$LiNbO_3$ waveguide with only 100-picojoule-level pump energy [87]. This system also supports SHG generation at 750 nm, which enables directly $f - 2f$ self-referencing detection on single waveguide. In 2020, Lu et al. experimentally demonstrated ultra-broadband SC generation from UVR to MIR in single-crystalline AlN waveguides [88]. Subsequent numerical simulations indicated a high degree of coherence of generated SC around the telecom pump and two dispersive waves. The reported SC generation on different platforms in the new bands are summarized in Figure 7. We note the suspended structures are promising for MIR SC generation, especially in the deep MIR region (> 4 μm). This is because not only the loss induced by the mode-leakage is eliminated, but also the core-cladding refractive index contrast is enhanced which leads to smaller mode area and stronger nonlinear interaction. The core layer of a suspended waveguide is typically a ridge structure, which enables array of holes on the ridge arms for wet-etching of substrate. A core layer of strip structure is also feasible because the suspension can be fabricated as pillar structure. The slot and multi-layer hybrid structures generally lead to flattened

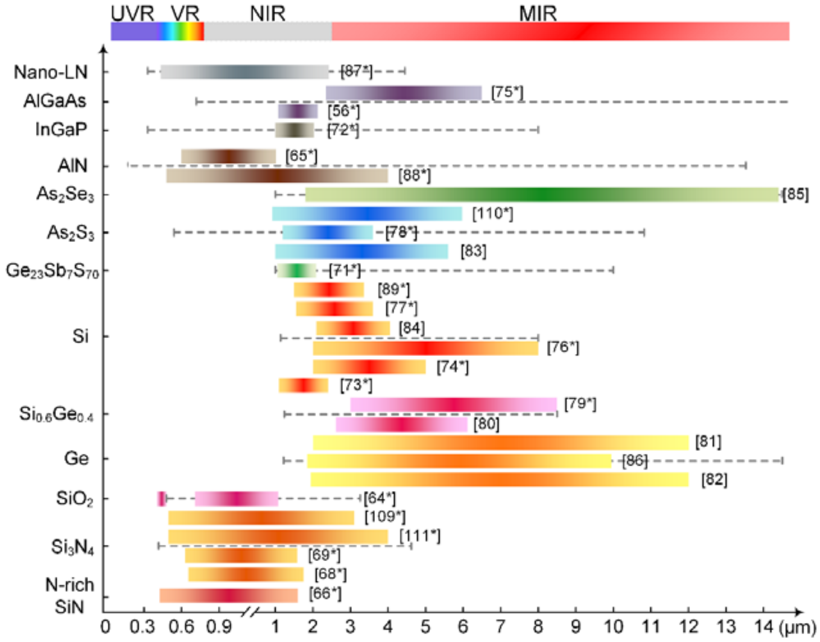

Figure 7. Reported SC generation on different platforms in the new bands. The grey dashed lines indicate the transparent windows of different materials. Experimental studies are marked with '*'.

dispersion with multiple zero-dispersion wavelengths, which is beneficial to broadband SC generation.

Optical frequency comb refers to a coherent source composed of discrete frequency lines with equal frequency interval. Frequency comb sources have found many applications in the fields of metrology, optical, atomic clocks, and high precision spectroscopy. While traditional laser-based frequency comb can be highly coherent, the spectral width is restricted by the gain bandwidth and is rather narrow. SC relates to frequency comb due to the development of $f-2f$ self-referencing technique. The f_{CEO} of a frequency comb can be detected and locked by this technique when the spectrum is octave spanning. This is crucial because most applications like metrology and spectroscopy require absolute frequency accuracy. Pumped by a repetition-rate (f_{rep}) stabilized femtosecond pulse train, the generated SC can be seen as a broad frequency comb with comb line interval equaling to f_{rep}. The f_{CEO} of generated octave-spanning SC can be locked by $f-2f$ technique, which makes SC an ultra-broadband frequency comb source. Experimental results of SC-based optical frequency combs on MNPWs have also been reported. Kuyken et al. experimentally demonstrated an octave-spanning MIR frequency comb generated on a Si nanowire waveguide [108]. The phase-coherent frequency comb was generated with a $-30\,\mathrm{dB}$ spectrum spanning from 1540 up to 3200 nm, and with coupled pump pulse energy as low as 16 pJ. Carlson et al. demonstrated self-referenced and efficient frequency comb on Si_3N_4 waveguide. Compared with conventional approaches that using highly nonlinear fibers, the average power is found to be approximately 10 fold lower [109]. Lee et al. experimentally achieved coherent SC generation in a nanospike chalcogenide-silica hybrid waveguide with pump pulse at 2 μm wavelength. The generated SC enables coherent locking of OPO to the optically referenced pump frequency comb, which results in a composite frequency comb with spectrum spanning $1 \sim 6$ μm [110].

Dispersive wave generation is another efficient method to achieve broadband optical frequency comb in new bands. Dispersive waves are less technologically flexible but more easily achieved than SC, as long as the perturbation of high-order dispersion is considerable. The spectrum of dispersive wave is localized and directional, which avoids energy waste in unwanted frequencies. The central frequency as well as the conversion efficiency of dispersive wave is tunable by tailoring the dispersion of waveguides. Of note, the coherence of pump source can be perfectly inherited by dispersive wave regardless of noise perturbation. Experimentally, in 2018, Guo et al. used a Si_3N_4 nanowire pumped by a 1.55 μm erbium-doped fiber-based femtosecond laser frequency comb to directly generate a MIR dispersive wave frequency comb

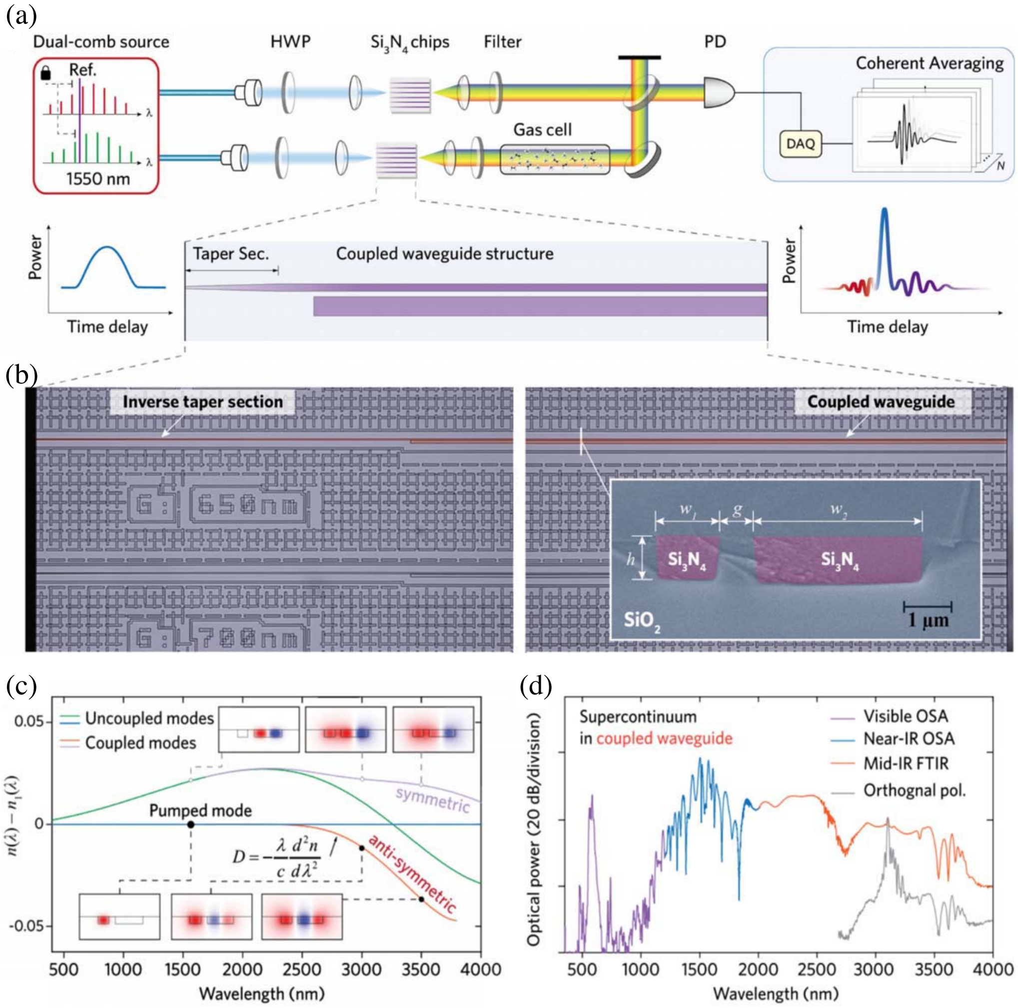

Figure 8. (a) Schematic diagram of the MIR dual-comb gas-phase spectroscopy, in which two MIR frequency combs are generated via coherent supercontinuum process in nanophotonic chip-based Si_3N_4 waveguides, seeded by a mutually locked dual-frequency-comb source at the telecom-band (i.e., ~ 1550 nm). HWP, half-wave plate; PD, (MIR) photodetector. (b) Microscopic pictures of a photonic chip with coupled Si_3N_4 waveguides, corresponding to both the input section, where the beginning of the waveguide contains an inverse taper structure, and the output section has dual-core waveguide structures. The false-colored SEM image of the waveguide cross section is also presented. (c) Calculated effective refractive indices of symmetric (purple curve) and anti-symmetric (orange curve) modes in a dual-core Si_3N_4 waveguide, compared with initial uncoupled modes separated in each core. (d) Experimentally observed supercontinuum generation in a dual-core Si_3N_4 waveguide [112]. Copyright 2020 OSA.

covering from 2.5 to 4 μm [111]. To realize the phase match between dispersive and pump waves, the integrated dispersion β_{int} should be zero. However, it is a little regretful that the conversion efficiency was only around 1%. In 2020, the same group experimentally obtained MIR dual-comb spectroscopy based on dispersive wave generation in dual-core Si_3N_4 nanowires [112]. Figure 8 shows the schematic diagram of the MIR dual-comb spectroscopy, the microscopic and SEM pictures of the dual-core Si_3N_4 waveguide, and the experimental results of the MIR dispersive wave. Two fully stabilized femtosecond laser frequency combs (Menlo comb system, $f_{rep} \sim 250$ MHz) with slight repetition rate difference ($\Delta f_{rep} \approx 320$ Hz) were used as the two pump seeds. The bandwidth of their dual-comb spectrometer covers the functional group region from 2800 to 3600 cm^{-1}, including more than 100,000 comb lines. The excellent performance enables quick and parallel gas-phase detection with a high sensitivity and sub-Doppler spectral resolution. In 2019, Grassani et al. experimentally demonstrated MIR dispersive wave tunable within 3 ∼ 4 µm by pumping the specially designed "top-hat" Si_3N_4 nanowires with a 2 µm fiber laser source [113]. A record-high conversion efficiency of 35% was achieved. The MIR source generated was successfully used for detection of C_2H_2 by absorption spectroscopy. On the same Si_3N_4 platform, in 2020, Tagkoudi et al. experimentally broadened the reachable spectral range of dispersive wave through careful optimization [114]. As a result, the dispersive wave can span the entire 3 ∼ 3.5 µm window without losing conversion efficiency. Table 1 summarizes the optical characteristics of different materials for chip-scale platform as a comparison.

Table 1. Optical characteristics of different materials for chip-scale platform.

Material	Bandgap (eV)	β_{TPA} (m/W) & cut-off λ	β_{3PA} (m^3/W^2) & cut-off λ	n	n_2 (m^2/W)	α (dB/cm)	Refs.
Si	1.1	5×10^{-12} & 2.2 µm	2×10^{-27} (@2.6 µm) & 4.3 µm	3.47	6×10^{-18}	3.4	[89–91]
a-Si:H	1.7	7×10^{-12} & 2.15 µm	/	3.73	1.7×10^{-17}	2.1	[89, 92]
Ge	0.8	6×10^{-10} (@2.8 µm) & 2.83 µm	5×10^{-27} (@4.8 µm) & 5.2 µm	4.3 (@ 3.2 µm)	4.4×10^{-17} (@3.2 µm)	2	[89, 90]
$Si_{0.6}Ge_{0.4}$	1.0	5×10^{-12} (@2.05 µm) & 2.4 µm	2×10^{-27} (@3.2 µm) & 4.3 µm	3.59	1.5×10^{-18} (@4 µm)	1.1 (@4 µm)	[90, 93]
SiO_2	9.0	/	/	1.46	2.6×10^{-20}	/	[94]
Si_3N_4	5.3	/	/	1.98	2.5×10^{-19}	0.5	[95, 96]
SiC	3.26	/	/	2.6	8×10^{-18}	12.8	[97]
AlN	6.2	/	/	2.1	2.3×10^{-19}	0.6	[98]
Ta_2O_5	4.4	/	/	2.05	7.2×10^{-19}	1.5	[99]
TiO_2	3.1	/	/	2.4	3.6×10^{-18}	5	[100]
Diamond	5.5	/	/	2.4	8.2×10^{-20}	0.34	[101]
AlGaAs	1.72	5×10^{-13}	/	3.3	2.6×10^{-17}	1.3	[102, 103]
$LiNbO_3$	3.8	/	/	2.21	2.5×10^{-19}	0.027	[89, 104]
As_2S_3	2.26	6.2×10^{-15}	/	2.43	3.8×10^{-18}	0.05	[89, 160]
As_2Se_3	1.77	1.4×10^{-12}	/	2.81	2.4×10^{-17}	1.4	[105, 106]
Doped silica	/	/	/	1.7	1.15×10^{-19}	0.06	[89, 107]

Note: The parameters without specification are values at 1.55 µm.

2.2. Kerr Microcombs Generation

Generation of Kerr microcombs on chip-scale optical microresonators is a robust and competitive technique for coherent sources generation in the new bands. It facilitates ultra-compact size to satisfy out-of-the-lab applications and shows explosive development in the last decade. Microresonators made of $\chi^{(3)}$ nonlinear materials, such as silica, highly doped silica, Si_3N_4, MgF_2, AlN [115], etc. can have high quality factor. Although Kerr microcombs generation has revolutionized the fields in the near-infrared band, such as terabit optical coherent communication, dual-comb spectroscopy, ultrafast ranging, atomic clocks, optical synthesis, etc. [116], it is still not widely developed in MIR, UVR, and VR bands.

When a CW pump field u_{in} with a center frequency of ω_0 is coherently injected into the cavity through a coupler, the boundary condition of the intracavity field u_{in} at the beginning of $m+1$ round trip is related to that at the end of the m round trip, which is described by the iteration step of Ikeda map as [117, 118],

$$u_{m+1}\left(0,T\right) = \theta^{\frac{1}{2}} u_{in} + \left(1-\theta\right)^{\frac{1}{2}} u_m\left(L,T\right) e^{i\phi_0} \tag{5}$$

where T represents the retarded time scale in one roundtrip, θ the power coupling coefficient of coupler, L the roundtrip length of cavity, and ϕ_0 the linear phase accumulation of the field inside the cavity per roundtrip. In each roundtrip, the evolution of $u(z,T)\,|_{z=0}^{L}$ is obtained by a GNLSE governed propagation model, as given by,

$$u\left(z,T\right)_z = -\frac{1}{2}\alpha u + i\sum_{k\geq 2} i^k \frac{1}{k!}\beta_k u_T^{(k)} + i\gamma\left(1+i\tau_s\partial_T\right)\left|u\right|^2 u \tag{6}$$

where z indicates the propagation distance, and τ_s indicates the optical shock time. For high finesse resonators, Eqs. (5) and (6) can be averaged to a mean-field Lugiato-Lefever equation (LLE) [119],

$$t_R u_t\left(t,T\right) = \theta^{\frac{1}{2}} u_{in} - \frac{1}{2}\left(\alpha L + \theta\right) u + i\left[L\sum_{k\geq 2} i^k \frac{1}{k!}\beta_k \partial_T^{(k)} + \gamma L\left(1+i\tau_s\partial_T\right)\left|u\right|^2 - \delta_0\right] u \tag{7}$$

where t_R stands for the round-trip time, and t represents the slow time variable. Strictly, this equation is only valid when t is equal to an integer multiple of t_R. The fast time T scales for the duration of temporal waveform in the resonator. The phase detuning of pump field with respect to the closest resonance peak with order l is expressed as the cavity phase detuning $\delta_0 = 2\pi l - \phi_0$. In addition, if the microresonator is made of materials like Si, the general LLE should be modified to include the free carrier and multi-photon absorption effects [120, 121],

$$\begin{aligned} t_R u_t\left(t,T\right) \;=\; & \theta^{\frac{1}{2}} u_{in} - \left(\frac{1}{2}\alpha L + \frac{1}{2}\theta + i\delta_0\right) u + \left[iL\sum_{k\geq 2}\frac{i^k}{k!}\beta_k \partial_T^{(k)} - \frac{\alpha_{FCA}}{2} + \frac{i}{c}\omega_0 n_{FCD}\right] u \\ & + \left(i\gamma L - L\sum_{n=2}^{4}\frac{1}{n} A_{\mathit{eff}}^{-(n-1)}\beta_{nPA}\left|u\right|^{2(n-2)}\right) \times \left(1+i\tau_s\partial_T\right) \\ & \times \left[u\left(t,T\right)\int_{0}^{\infty} R\left(\eta\right)\left|u\left(t,T-\eta\right)\right|^2 d\eta\right] \end{aligned} \tag{8}$$

For Kerr microcombs generation in the VR region, in 2014, Jung et al. experimentally proposed a method with high-Q AlN microring resonator pumped by a telecom CW laser [115]. The Kerr microcomb at the telecom band was generated first, and then used to generate comb-like spectrum at the VR region through the second harmonic, third harmonic, and sum frequency conversion in the same AlN microring. Similarly, in 2018, Liu et al. experimentally utilized an AlN microring to obtain near-VR comb lines in $720 \sim 840\,\mathrm{nm}$ from a NIR microcombs through spectral translation [122]. The conversion efficiency is as low as $4.1\times10^{-5}\%$. In 2016, Wang et al. experimentally demonstrated green-light frequency comb generation in high-Q $\mathrm{Si_3N_4}$ microring resonators with a conversion efficiency of only 0.04% [123]. The nonlinear processes in this experiment involve third harmonic generation and third-order sum frequency generation, which allows the conversion of NIR frequency combs into green light region. By using a high-Q AlN microring, Guo et al. achieved near VR region Kerr microcombs in 2018 with a high conversion efficiency of 22% [124].

In the NIR region, silica and $\mathrm{Si_3N_4}$ are the most efficient materials for chip-scale Kerr microcomb generation. For example, $\mathrm{Si_3N_4}$ simultaneously possesses relative high Kerr nonlinearity (typically $\sim 0.9\,\mathrm{W^{-1}/m}$), low loss (typically $\sim 0.2\,\mathrm{dB/cm}$), no photon-absorption, and mature fabrication technology compatible with the CMOS foundry. In 2017, Lee et al. experimentally achieved soliton microcombs around 778 and 1064 nm with an on-chip high-Q silica edge microresonator [125]. In

2019, Raja et al. experimentally coupled an III-V-material-based laser diode chip to a high-Q Si$_3$N$_4$ microresonator [126]. With an average power less than 1 W, a soliton microcomb with sub-100-GHz line spacing has been obtained with pump wavelength around 1540 nm. In 2020, Briles et al. experimentally utilized the Si$_3$N$_4$ microresonators to comprehensively study low-power octave-spanning single soliton Kerr microcombs generation in both the 1550 nm and 1064 nm bands [127]. In the same year, Fujii et al. experimentally demonstrated that by engineering the sidewall angle of a small-radius ($\sim$ 100 μm), 3-μm-thick silica wedge microdisk, dispersion tuning in both normal and anomalous regimes can be realized without significantly affecting the free spectral range [128]. The designed microdisk with a wedge angle of 55° was used to generate a 300 nm wide Kerr microcomb in the anomalous dispersion region under pump wavelength around 1550 nm.

In the MIR region, Group IV elements are employed to fabricate the microresonators because their broad transparent windows and negligible nonlinear photon-absorptions in this region. Silicon-based or germanium-based microresonators are promising platforms for MIR Kerr microcombs generation. In 2016, Yu et al. experimentally generated a mode-locked soliton Kerr microcomb in the MIR region covering the spectral range from 2.4 to 4.3 μm [129]. It was found that up to 40% of pump energy was converted to the output comb power. Two years later, in 2018, the same group experimentally demonstrated MIR dual-comb spectroscopy on a SOI microring platform [130]. Figure 9 shows the experimental setup, dual-comb generation, and dual-comb spectroscopy results. A single CW pump source with power as low as 80 mW was used to generate two coherent Kerr microcombs covering 2.6 $\sim$ 4.1 μm in two Si microrings with slightly different free spectral range (FSR). The pump-to-comb conversion efficiencies of two microcombs are found to be both $> 30\%$. Although the microcombs generated are multi-soliton state, the dual-comb spectroscopy could still acquire spectra of acetone at 127 GHz (4.2 cm^{-1}) resolution. They further demonstrated high-throughput label-free MIR dual-comb

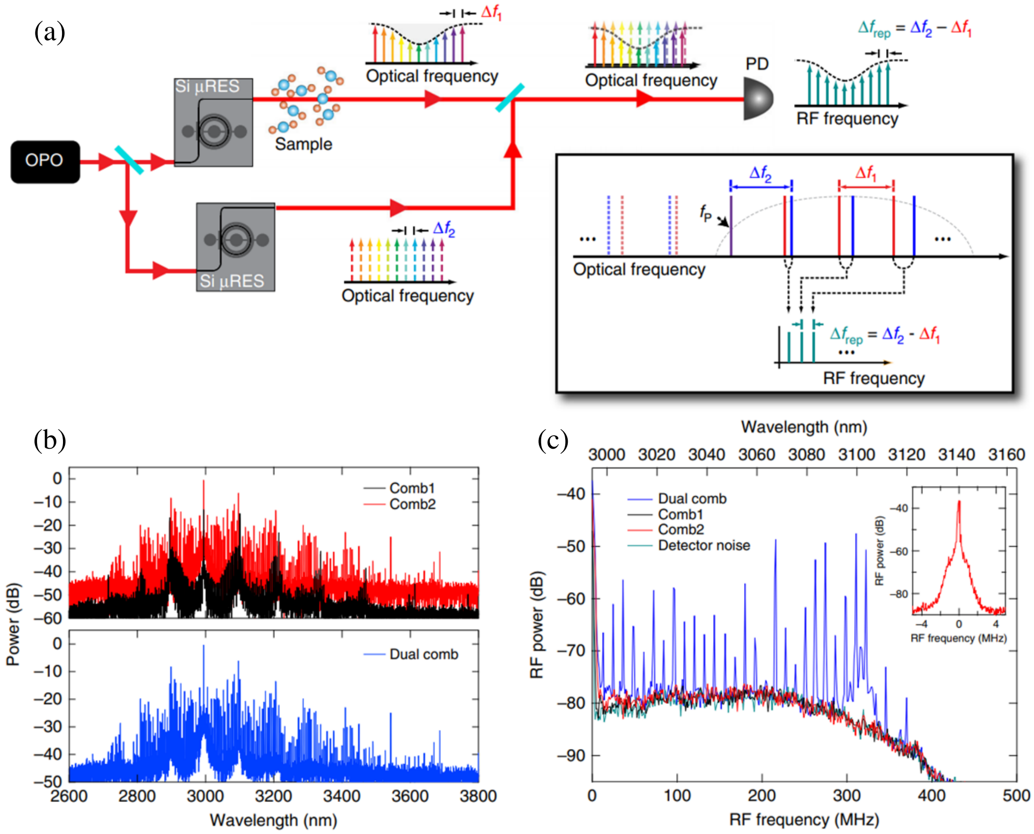

Figure 9. (a) Experimental setup for dual-comb absorption spectroscopy. (b) Spectra of each mode-locked comb (multi-soliton states) and combined M-FT spectrum. (c) RF spectrum from the dual-comb interferometer [130]. Copyright 2018 Nature Publishing Group.

spectroscopy based on Kerr microcombs in Si microfluidic microresonators. The label-free spectroscopy gives a direct detection of targeted molecular regardless of fluorescent labeling. The flow dynamics of an acetone droplet was successfully measured with a high spectral acquisition rate of 25 kHz (40 µs per spectrum, comparable to the state-of-art Michelson based Fourier-transform infrared spectrometer) covering a spectral range from 2900 to 2990 nm [131]. The mitigation of intracavity stimulated Raman scattering when the pump wavelength is shifted to 2 µm band eliminates the Raman–Kerr comb competition, thus facilitating soliton microcombs generation. Gong et al. experimentally generate microcombs around 2 µm in a high-Q z-cut nano-$LiNbO_3$ microring [132]. This is the first experimental demonstration of MIR single soliton Kerr microcomb generation on nano-$LiNbO_3$ platform.

In the respect of theoretical works, in 2018, Guo et al. numerically obtained an octave-spanning Kerr microcombs in a germanium (Ge) microresonator covered from 2.3 to 10.2 µm [133]. The spectral bandwidth and flatness were remarkably enhanced by maintaining dispersion flatness from 3.5 to 10 µm through a mode hybridization technique. The mode hybridization gives abruptly inflection of dispersion profile at the hybridization wavelength, and thus leads to transformation between normal and anomalous dispersion regimes. New nonlinear platforms have been proposed for MIR Kerr microcombs generation. In 2019, Fan et al. numerically showed that a slot waveguide could obtain mode-locked MIR Kerr microcomb in a $LiNbO_3$ microring [134]. With only 50 mW pump power, the generated Kerr microcomb covers from 2810 nm to 4630 nm. In 2019, Anashkina et al. numerically studied MIR Kerr microcomb generation spanning $3 \sim 4$ µm at −30 dB spectrum level in an As_2S_3 microbubble resonator with a potential low pump power of 10 mW [135]. The spectral range of the Kerr microcombs could span more than 700 nm. An effective method for spectrum stretching of Kerr microcombs is to draw support from a post process of SC generation. In this method, a CW source is used as primary pump to generate the Kerr microcomb in a microresonator. The generated Kerr microcomb is filtered to remove the residual CW pump component, and then injected into a strip waveguide for SC generation. The generated broadband SC is used for $f-2f$ self-referencing locking of carrier-envelope phase. This idea has been experimentally achieved by Lamb et al. in 2018. A broadband, 15-GHz repetition-rate frequency comb source is achieved, which is appropriate for optical-frequency comparisons and $f-2f$ self-referencing [136]. The principle, experimental setup, and results for soliton Kerr microcomb and SC generation are shown in Figure 10. Table 2 summarizes the reported schemes for Kerr microcomb generation at VR, NIR, and MIR bands.

Table 2. Reported Kerr microcombs generation in the new bands. Experimental studies are marked with ‘*’.

Region	Material	Structure	Q factor	Range (µm)	Refs.
VR	AlN	Microring	Q_L: 5×10^5	0.517, 0.776, and 1.4 to 1.65	[115]*
VR and NIR	AlN	Microring	Q_L: 1.1×10^6	0.72 to 0.84, and 1.4 to 1.7	[122]*
VR and NIR	SiN	Microring	Q_L: 1.30×10^6	0.502 to 0.58, and 1.327 to 2.082	[123]*
VR and NIR	AlN	Microring	/	0.72 to 0.82, and 1.4 to 1.7	[124]*
VR and NIR	SiO_2	Microring	Q_0: 8×10^7	0.76 to 0.79	[125]*
NIR	Si_3N_4	Microring	$Q_0>1\times10^7$	1.5 to 1.56	[126]*
NIR	$LiNbO_3$	Microring	Q_L: 1.1×10^6	1.68 to 1.8, and 1.88 to 1.96	[132]*
NIR	Si_3N_4	Microring	/	1.1 to 2.4, and 0.86 to 1.7	[127]*
NIR	SiO_2	Microdisk	Q_L: 4.5×10^5	1.4 to 1.7	[128]*
MIR	Si	Microring	Q_L: 2.45×10^5	2.4 to 4.3	[129]*
MIR	Si	Microring	Q: 1×10^5	2.6 to 4.1	[130]*
MIR	Si	Microring	/	2.9 to 2.99	[131]*
MIR	Ge	Microring	Q_0: 4×10^4	2.3 to 10.2	[133]
MIR	$LiNbO_3$	Microring	/	2.81 to 4.63	[134]
MIR	As_2S_3	Microbubble	Q_0: 1×10^6	3 to 4	[135]
VR to MIR	Silica+Si_3N_4	Microdisk + strip	/	0.7 to 2.1	[136]*

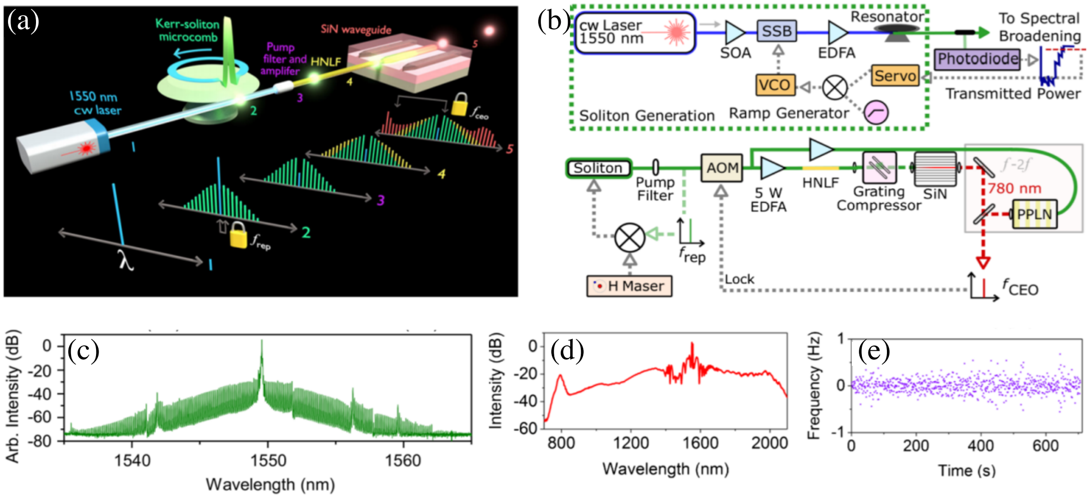

Figure 10. (a) Pictorial representation of frequency-comb generation and spectral evolution through the system. A two-stage approach, first using a highly nonlinear fiber (HNLF) and then using a S_3iN_4 waveguide, is used to achieve broadband spectra from a microcomb. (b) Upper panel: soliton generation and stabilization using the lock technique described in the text. cw, continuous wave; SOA, semiconductor optical amplifier; SSB, single-side band modulator; EDFA, erbium-doped fiber amplifier; VCO, voltage-controlled oscillator. Lower panel: SC generation and frequency-comb stabilization with a S_3iN_4 waveguide. frep, repetition-rate frequency; AOM, acousto-optic modulator; HNLF, highly nonlinear fiber; SiN, silicon nitride; PPLN, periodically poled lithium niobate; f_{CEO}, carrier-envelope offset frequency. (c) Spectrum of a single soliton. (d) Octave-spanning SC generated when the waveguide is pumped with a single soliton. (e) Frequency-counter data for the locked f_{CEO} (1 s gate time) [136]. Copyright 2018 APS.

2.3. Intermodal Four-Wave Mixing

Conventional FWM involves four optical waves (nondegenerate) or three optical waves (degenerate) in a nonlinear medium. For example, in the process of degenerate FWM two pump photons at frequency ω_p are converted into another two photons with new frequencies ω_s and $\omega_{i,}$ satisfying $2\omega_p = \omega_s + \omega_{i,}$. This process obeys the energy and momentum conservation. The efficiency η of FWM can be written as [137]:

$$\eta \propto \sin c\left(\Delta k \frac{L}{2\pi}\right)^2 \tag{9}$$

where Δk represents the phase matching, and L stands for the length of waveguide. The phase matching condition means Δk should be zero to maximize the efficiency. Δk includes a linear part Δk_L and a nonlinear part Δk_{NL}, which are related to the waveguide modes of the pumps, signal and idle. Intermodal FWM requires phase matching among different guided modes. Considering the nondegenerate FWM process, the linear part Δk_L determined by the effective refractive index n_{eff} is given by [137],

$$\Delta k_L = \frac{\omega_{p1}}{c} n_{eff}^{j}\left(\omega_{p1}\right) + \frac{\omega_{p2}}{c} n_{eff}^{q}\left(\omega_{p2}\right) - \frac{\omega_s}{c} n_{eff}^{l}\left(\omega_s\right) - \frac{\omega_i}{c} n_{eff}^{m}\left(\omega_i\right) \tag{10}$$

where p_1, p_2, s, i represent two pumps, signal, and idle, respectively; c is the velocity of light in vacuum; j, q, l, m indicate the orders of guided modes of the first pump, the second pump, the signal, and the idler photon, respectively.

In recent years, intermodal FWM has been preliminarily studied on Si-based MNPWs. In 2018, Signorini et al. studied both the intermodal spontaneous and stimulated FWM through simulation and experiment [137]. The geometrical parameters of waveguide enabled flexible dispersion engineering so that phase matching conditions among different modes could be satisfied. Figure 11 shows the

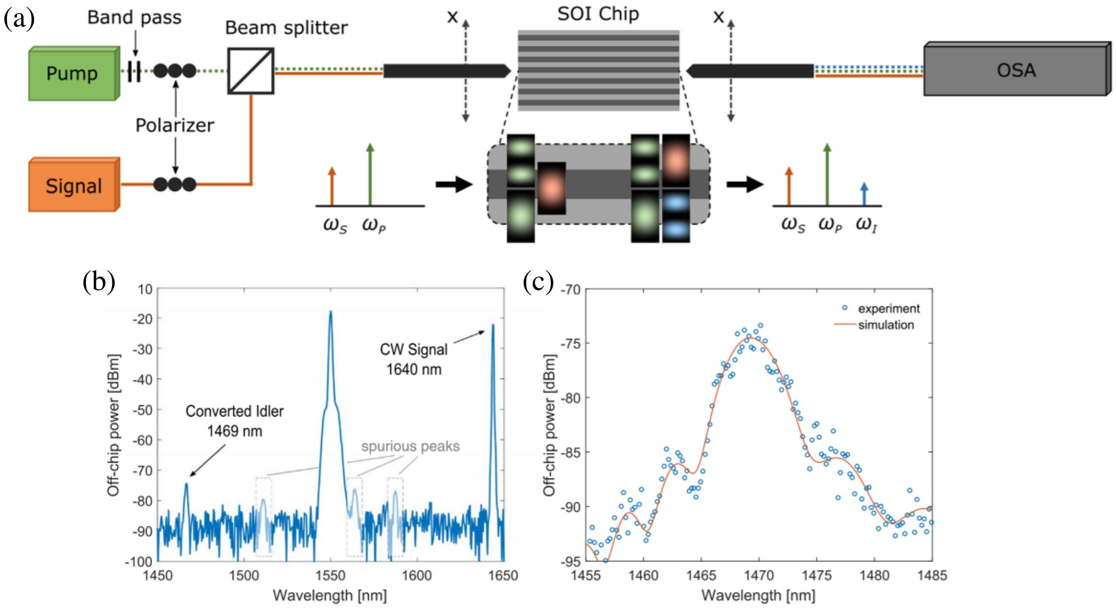

Figure 11. (a) Setup for the stimulated FWM. The pump is initially filtered with two 1550 nm bandpass filters. Then, the pump and signal are mixed by a free-space beam splitter and coupled into the same tapered lensed fiber through a collimator. The input fiber injects the light into the waveguide on the SOI chip. The light is collected from the waveguide by another tapered lensed fiber. The collected light is analyzed with an OSA or a monochromator. In the inset, the waveguide modes are sketched by showing the mode profiles; as an example, the case of the (1, 2, 2, 1) modal combination is considered. For the spontaneous FWM, the setup is the same except for the lack of the input signal. (b) Spectrum of the stimulated FWM with the (1, 2, 2, 1) TE intermodal combination. The stimulating CW signal at 1640 nm is converted into the pulsed idler at 1469 nm. The smaller peaks are spurious signals due to the OSA. (c) Spectrum of the stimulated idler generation efficiency with the intermodal FWM combination (1, 2, 2, 1) TE mode. The blue circles are the measured data, while the orange line is the simulation. The simulated spectrum was shifted by −3.3 dBm in order to match the experimental data [137]. Copyright 2018 OSA.

experimental setup and intermodal FWM results. When the pump was on both the fundamental and 2-nd TE modes, and the signal was on the fundamental TE mode, an idler on the 2-nd TE mode was achieved. They also studied intermodal FWM with other modal combinations up to 3-rd TE and TM modes.

In the same year, Signorini et al. achieved single photon pairs through the intermodal FWM on a Si rib waveguide. The coincidences between the idle at 1.281 µm and the signal at 1.952 µm with the (1, 2, 2, 1) TE modal combination were measured [138]. They proposed asymmetric directional couplers to extract higher-order modes, demonstrating a fully integrated scheme of intermodal FWM. The high tunability of phase matching wavelength and bandwidth of intermodal FWM was studied in their work. In 2019, Lacava et al. used the Bragg scattering (BS) intermodal FWM method to achieve a dual-CW-pumped SOI wavelength converter [139]. The idler and signal were both on the fundamental TE mode, and two pumps were on the 2-nd TE mode. They found that the overall BS FWM efficiency was limited by the TPA and FCA effects in Si. In the same year, they also proposed another scheme to realize the BS intermodal nondegenerate FWM on a fabricated Si-rich silicon nitride platform [140]. Figure 12 shows the experimental setup in this work. The two pump waves on the fundamental mode are in the C-band and could realize efficient phase matching with the signal on the 2-nd TE mode far away in the L-band. Thus, the wavelength conversion over a bandwidth exceeding 40 nm was achieved by intermodal FWM. The conversion efficiency (ratio between the output idler and the output signal power levels) was measured to be −15 dB for a total input pump power of 32 dBm.

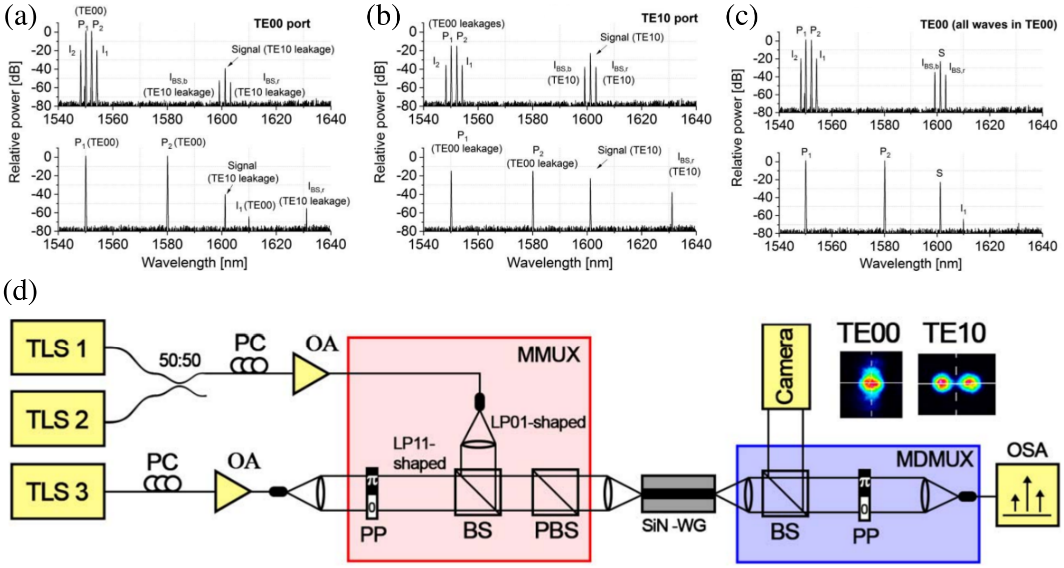

Figure 12. Generated spectra when (a) P_1, P_2 and S were launched in the TE00, TE00 and TE10 modes, respectively; (b) P_1, P_2 and S were launched in the TE00, TE00 and TE10 mode, respectively; (c) P_1, P_2 and S were all launched in the TE00 mode; (d) Experimental setup for the BS FWM. Inset figures: spatial modes distributions at various points in the system [140]. Copyright 2019 OSA.

Further optimization of the waveguide to reduce the loss is claimed to help in achieving higher conversion efficiency. Guo et al. experimentally showed the formation of breather solitons in two microresonator platforms (crystalline MgF_2 and photonic chip-based Si_3N_4 microresonators) dominated by intermodal FWM process. Breather solitons undergo a periodic evolution in their amplitude and duration are found in their experiments [141].

3. NONLINEAR PULSE SHAPING

When an optical pulse with high intensity was injected into a nonlinear medium, its electric field will strongly change the motion state of bound electrons, which results in the so-called polarization intensity. In turn, the electrons will react to incoming pulses and cause the redistribution of pulse frequency components. The intensity distribution in the time domain is changed, and pulse shaping occurs. For example, pulses from the Yb-doped fiber lasers are usually with the Gaussian form. But it can be easily shaped to the parabolic, triangular, and flat-top profiles by means of nonlinear pulse shaping in $\chi^{(3)}$ media [142–144]. Artificial neural networks have been recently used for nonlinear pulse shaping in optical fibers, in which powerful machine-learning models retrieve the parameters of nonlinear propagation from the observed output pulses [145, 146]. In the frequency domain, the spectrum can be equally sliced in multistage parametric mixer with nonlinear pulse shaping [147]. This method is essentially different from the linear pulse shaping [148]. The latter one is often accomplished by using a spatial light modulator (SLM) or bulky electro-optic modulator, in which the phase, amplitude, and polarization of light are changed linearly. While programmable linear pulse shaping technology in the liquid crystal and acousto-optic SLMs have been fulfilled, the nonlinear pulse shaping has unique advantages such as ultrafast response time (femtosecond level) and broad operation bandwidth. More importantly, by using the nonlinear pulse shaping, it is possible to realize a fully passive optical-to-optical controlled module, which is particularly important for the future all-optical devices. Chip-scale MNPWs makes pulse shaping on a chip possible. The current linear pulse shaping in bulky and electrically driven modulators is still difficult to integrate. Due to the inherent large nonlinear refractive index of MNPWs, the power consumption required by nonlinear pulse shaping can be much lower. Different techniques for nonlinear pulse shaping on MNPW platforms are reviewed in the following.

3.1. Pulse Compression

PC is a key technology for generating ultrashort pulses, which are widely used in optical communication systems [149], SC and frequency comb generation [150], ultrafast spectroscopy [151], and biology [152]. While many applications benefit from pulses with ultrashort duration and high average power, it is a challenge to simultaneously achieve both with a laser. For example, a Ti:Sapphire solid-state laser can produce few-cycle pulses, but the average power is usually limited to only a few watts. Conversely, by using a Yb-doped laser one can obtain pulses with an average power over 100 W, the pulse duration is however restricted in a few hundreds of femtoseconds due to the limited gain bandwidth. Therefore, additional PC process outside a laser cavity is necessary. PC techniques include chirp compensation compression, soliton self-compression (SSC), nonlinear absorption assisted compression, and self-similar compression.

Chirp compensation compression is the most typical PC technique that has been employed for a long time [153]. The first step of this technique is to achieve a positive chirp accompanied by nonlinear phase accumulation at a normal dispersion region. Then, the resultant positive chirp is compensated by negative ones introduced by post chirped lens, gratings, or prisms. To design such a system on MNPW platforms, the GVD of the first-stage waveguide should be tailored to be normal. After the optical spectrum is expanded by a strong nonlinear effect in the first-stage waveguide, a successive stage with anomalous GVD cancels the positive chirp. Consequently, the input pulse is temporally compressed. This idea has been confirmed with both simulations and experiments. In 2019, Mei et al. numerically designed a cascaded Si waveguide which is buried in a silica box for PC at pump wavelength of 1550 nm [154]. As shown in Figure 13(a), the cascaded Si waveguide is divided into three segments of A, B, and C. Segment A was used to transfer the input Gaussian pulse to PP by using the self-similar technique within normal dispersion region. Segment B was used to convert the GVD at 1550 nm from positive to negative. Segment C was designed to be a strip Si waveguide whose GVD is anomalous at the pump wavelength. Parabolic pulse compression occurs at section C. Simulation results showed that the input Gaussian pulse first efficiently evolved into a PP, and finally compressed to 35.6 fs. The corresponding evolution of temporal pulses are shown in Figures 13(b), 13(c), and 13(d) respectively for three different self-similar cases. The insets show the pulse propagation in segment B for each case. The largest compression factor among the three self-similar cases is 8.4. The compressed pulse is not only chirp

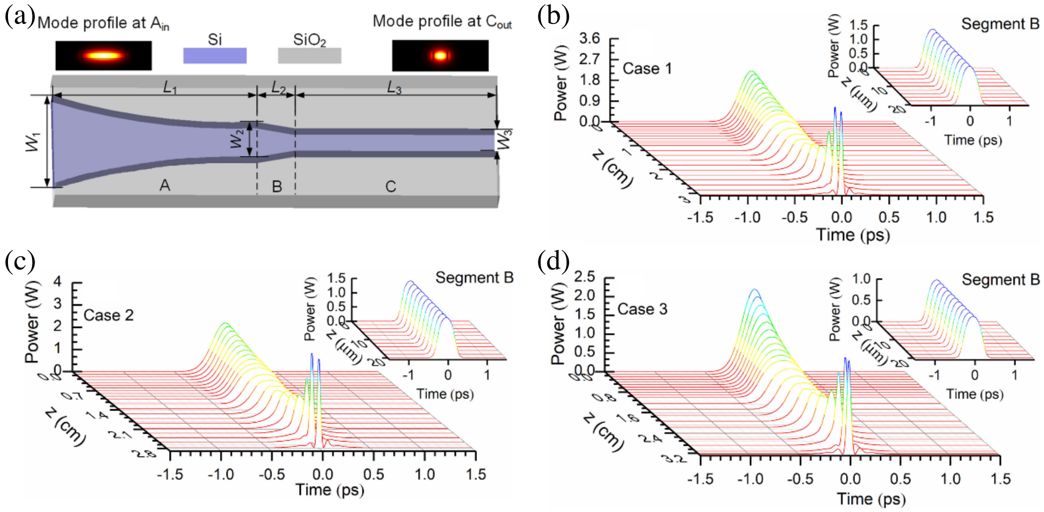

Figure 13. (a) Schematic diagram of cascaded Si waveguides buried in silica box, the mode field distributions at the input of segment A and output of segment C at the pump wavelength of 1550 nm. The evolutions of the temporal pulses in the cascaded Si waveguides for (b) Case 1 ($A_{in} = 300$ fs, $A_{out} = 464.9$ fs and $C_{out} = 37.6$ fs), (c) Case 2 ($A_{in} = 300$ fs, $A_{out} = 443.7$ fs and $C_{out} = 35.6$ fs), and (d) Case 3 ($A_{in} = 300$ fs, $A_{out} = 475.5$ fs and $C_{out} = 45.9$ fs). The insets in (b), (c), and (d) are the evolutions of the temporal pulses in Segment B [154]. Copyright 2019 IEEE.

free, but also has very low pedestals. Tan et al. reported the first experimental demonstration of a chip-scale pulse compressor on specially designed Si nanowire waveguide [155]. The PC scheme uses first-stage nonlinear spectral broadening induced by SPM in a Si nanowire. Temporal compression occurs in an integrated dispersive grating. Leveraging a low input peak power of 10 W, they achieved a compression factor as high as 7 for a 7-ps input pulse. The waveguide structure includes the bended strip waveguide and periodic coupled grating structure. Within the 3-dB bandwidth of the dispersive grating, the group delay was almost linear. The 3-dB transmission bandwidth of grating was 11 nm. It is shown that free carriers do not degrade the PC at a certain low peak power level. The compressed pulse, unfortunately, exhibited severe pedestals because of the imperfect chirp compensation at the leading and trailing edges of the pulse.

SSC is a unique compression technique which can achieve higher-order soliton pulses. For SSC, the required nonlinear effect is much stronger, yielding $L_{NL} < L_D \ll L$ where $L_D = T_0^2/|\beta_2|$ and $L_{NL} = 1/(\gamma P_0)$ are dispersion length and nonlinear length, respectively. Both nonlinearity and dispersion are required to be large for SSC in short propagation length. While $L_{NL} < L_D$ can be inherently satisfied by higher-order soliton injection, the realization of short-length SSC depends on MNPW design. Photonic crystal waveguide (PhCW) is a competitive candidate due to its giant nonlinearity and dispersion enhanced by slow-light effect. Slow-light effect makes the light propagating in PhCWs much slower than in common MNPWs. Consequently, nonlinear accumulation can be significantly enhanced. Moreover, the dispersion of PhCW can be flexibly adjusted by changing parameters such as hole size and hole spacing. Colman et al. reported the first experimental observations of SSC in GaInP PhCWs with periodic dielectric structure [156]. Remarkable pulse narrowing occurs due to the strong interaction between GVD and slow light enhanced SPM effect. As a result, a 3-ps input pulse was compressed to a minimum pulse duration of 580 fs, corresponding to pulse energy of $\sim$ 10 pJ. The small A_{eff} ($10 \sim 13\,\mu\mathrm{m}^2$) combined with slow light enhanced nonlinearity allows for an ultralow power threshold SSC at millimeter propagation length scale. However, the used GaInP is not compatible with current CMOS foundry. Alternatively, Sahin et al. reported the observation of SSC and associated dynamics in a CMOS-compatible ultra-Si-rich nitride (USRN) Bragg grating [157]. The schematic diagram of the designed Bragg grating which employs the silica as under- and over-cladding is shown in Figure 14(a). Due to the special grating structure, the higher-order Bragg soliton was formed with a pulse width of 4.93 ps, as shown in the right panel of Figure 14(b). The pulse width was compressed to 0.86 ps, corresponding to a compression factor of 5.7 and soliton order of 4.65. To further increase the compression factor, Choi et al. reported on-chip SSC by using strip waveguide made of USRN in 2019 [158]. The initial pulse with duration of 2 ps and energy of $\sim$ 16 pJ is pumped at 1550 nm wavelength. The experimental results showed an impressive compression factor of 8.7, which is the largest for a chip-scale MNPW platform to date.

For SSC on Si-PhCW platforms, in 2014, Redondo et al. experimentally reported SSC of picosecond pulse pumped at 1547 nm [159]. The input pulse was compressed from 3.7 to 1.6 ps, and the used energy was as low as 10 pJ. Figures 15(a) and 15(b) show the physical interpretation of this scheme in both time and frequency domain. Different from the nonlinear fiber platforms in which Raman self-frequency shift effects can slow down and compress the pulse, the proposed Si-PhCW exhibits a free-carrier effect that accelerates the pulse propagation accompanied by significant intensity reduction, temporal asymmetry, and compression. The input 3.7-ps pulse was compressed to a minimum duration of 1.6 ps. The corresponding compression factor is 2.3 and compressed peak power is 2.4 W ($\sim$ 9 pJ). This work is the first experimental demonstration of picosecond SSC on Si-PhCW platform at the telecom band.

In the aspect of theoretical works, Amine et al. proposed SSC in highly nonlinear chalcogenide nanowires with ultralow pulse energy [160]. By controlling the diameter of As_2S_3 and As_2Se_3 nanowires to be smaller than pump wavelength, a 5.07-fs pulse in an 0.84 mm-long As_2S_3 photonic nanowire was generated. This near single-cycle pulse was obtained starting from a 250-fs input pulse with 50 pJ energy. Because of the high TPA coefficient of As_2Se_3 glass, the compression of 250 fs was only down to 25.4 fs in a 2.1 mm-long As_2Se_3 nanowire with 10 pJ input pulse energy. In 2014, Lavdas et al. theoretically studied the tapered Si nanowire for SSC [161]. The pump wavelengths in both telecom (1550 nm) and MIR (2100 nm) bands were studied when the input soliton order is up to 10. The linear and nonlinear optical properties, especially the TPA, FCA, and FCD, of the waveguide were found to be controllable in such a tapered structure. Simulation results showed that the compression factor can exceed 10 at

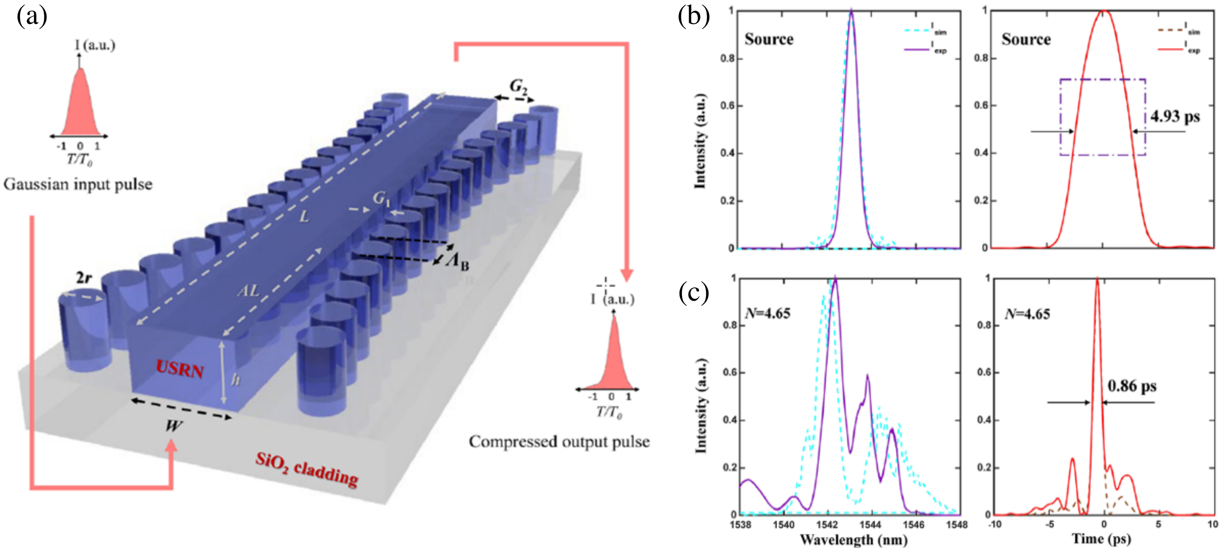

Figure 14. (a) 3D schematic diagram of cladding-modulated Bragg gratings with parameters denoted: pitch (Λ_B), waveguide width (W), height (h), length (L) and pillar radius (r) and gaps (G_1 and G_2). Input and output pulses show the effect of nonlinear pulse propagation along a Bragg grating at wavelengths close to the stop-band for a picosecond pulse. (b) Measured spectral and temporal profiles of the source pulse. (c) Measured spectrum and temporal profile of soliton evolution for $N = 4.65$ [157]. Copyright 2019 Wiley Online Library.

the MIR band.

Nonlinear absorption assisted compression is a special PC technique achieved by employing the FCA effect. The energy of pulse is depleted at the trailing edge, resulting in pulse peak moving towards the leading edge due to free carrier accumulation. Consequently, the pulse duration is reduced. In 2007, Tien et al. experimentally demonstrated this method in Si waveguide [34]. The compression of 400-ps mode-locked pulses at 1560 nm is shown in a 1.7 cm-long Si waveguide. The proposed scheme was confirmed to be wavelength independent, enabling a broadband PC from 1.1 and 2.2 µm. The proposed scheme can be easily implemented with Ge waveguides to facilitate mode-locking up to 3.4 µm. Here, nonlinear absorption properties of Si have been utilized as opposed to Si-Ge Bragg reflector. The initial launched optical pulse with high intensity stimulates the inherent TPA process in Si waveguide when the pumping wavelength is located at telecom band. After that, an electron-hole pair is created instantaneously. Since the lifetime of free carrier is much larger than input pulse width, free-carrier concentration will be built up over the whole pulse duration. Larger energy loss at the trailing edge leads to PC. If the Si MNPW is used as a part of intracavity resonator, mode-locking of long pulse is possible.

Self-similar PC is another efficient technique to achieve pedestal-free and large compression factor PC. It has been theoretically proposed [162, 163] and then numerically confirmed in PCFs [164]. According to the self-similar theory, the evolution of pulse width in a nonlinear medium with varied β_2 and γ is given by,

$$T_{out} = T_{in} \frac{\beta_2(z)\,\gamma(0)}{\gamma(z)\,\beta_2(0)} \tag{11}$$

where T_{out} and T_{in} are the output and input pulse width, and $\gamma(0)$ and $\beta_2(0)$ are the values of $\gamma(z)$ and $\beta_2(z)$ at $z = 0$, respectively. The analytical solutions of $\gamma(z)$ and $\beta_2(z)$ are given by [163],

$$\gamma(z) = \frac{\gamma(0)}{1 - \sigma z}, \tag{12a}$$

$$\beta_2(z) = \beta_2(0)\, e^{-\sigma z}, \tag{12b}$$

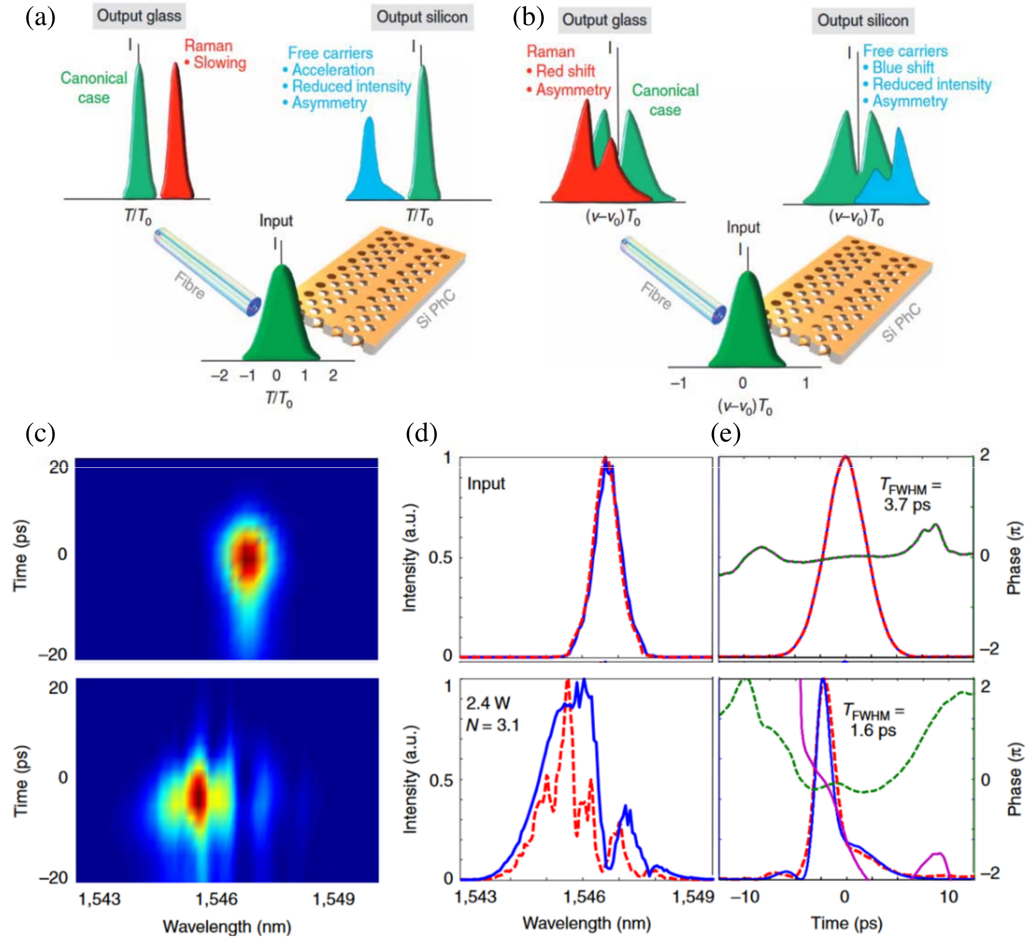

Figure 15. Schematic diagram illustrating the differences between different soliton regimes. (a) Time domain behavior of SSC in the fiber (Raman) and Si PhCWs (free carriers) with anomalous dispersion. (b) Representation of the spectral domain with red Raman (fiber) and blue free-carrier shifts (Si PhCWs) of the pulse energy. (c) Experimental FROG spectrograms of the input (upper panel) and output (lower panel) pulses. (d) measured (dashed red) and modelled (blue) intensity in the spectral domain; (e) measured intensity (dashed red) and phase (dashed green) along with the NLSE-modelled intensity (blue) and phase(magenta) in the time domain following numerical deconvolution [159]. Copyright 2014 Nature Publishing Group.

where $\sigma = \beta_2(0)\xi$, ξ is the initial chip factor of optical pulse. There are three cases for self-similar PC: (i) jointly varied $\gamma(z)$ and $\beta_2(z)$, (ii) varied $\gamma(z)$ and constant $\beta_2(z)$, and (iii) constant $\gamma(z)$ and varied $\beta_2(z)$, the corresponding output pulse width for the three case are as follows,

$$T_{out} = \begin{cases} T_{in}e^{-\sigma z}/(1-\sigma z)\,, & \text{(i)} \\ T_{in}/(1-\sigma z)\,, & \text{(ii)} \\ T_{in}e^{-\sigma z}, & \text{(iii)} \end{cases} \tag{13}$$

where $\sigma > 0$ and $\sigma z < 1$. As described by Eq. (13), the pulse width is decreased with propagation. The self-similar theory can ensure that the propagating pulse is a fundamental soliton over the whole propagation path. The PC factor is proportional to the product σz. Nonlinear photon absorption and free carrier effect will invalidate the self-similar condition, thus materials with larger bandgap than Si (e.g., SiN and chalcogenide) are preferred.

Self-similar PC has been theoretically studied in MNPWs in recent years. In 2016, Mei et al. carefully designed a chalcogenide-silicon hybrid slot waveguide taper to realize self-similar PC

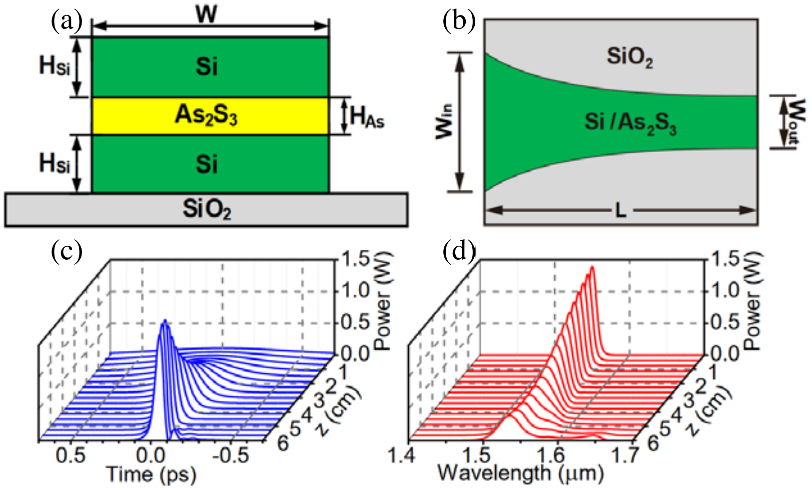

Figure 16. (a) Cross-section, and (b) top view of the designed As_2S_3-Si hybrid slot waveguide taper, where W_{in} and W_{out} represent the widths of the input and output ports, respectively. The evolution of self-similar fundamental soliton compression is shown in the (c) time and (d) frequency domains, respectively [165]. Copyright 2016 IEEE.

numerically when the pumping wavelength is 1.55 μm [165]. Figure 16 shows the designed waveguide structure and compression performance. Within a 6 cm-long taper, a 1-ps fundamental soliton pulse was self-similarly compressed to 81.5 fs, with a compression ratio of 12.3. When the input soliton order is increased to 2, initial pulse width of 1 ps was compressed to 80.3 fs in a reduced waveguide length of 2.54 cm. The corresponding compression ratio is 12.45. The pedestals resulting from higher-order dispersive and nonlinear effects were confirmed to be extremely low. To simplify the waveguide fabrication, Huang recently numerically designed a tapered Si ridge slot waveguide operating at 1.55 μm. An initial 1-ps pulse was compressed to 82.53 fs. The corresponding peak power of the compressed pulse is 7.11 times higher than that of the initial pulse [166]. In 2017, Yuan et al. numerically designed a reverse tapered Si waveguide for self-similar compression at shallow MIR region [167]. A 1-ps long pulse pumped at 2.49 μm was self-similarly compressed to 57.29 fs in a 5.1 cm-long waveguide. The corresponding compression factor is 17.46. This waveguide structure is simple to fabricate and does not show detrimental effects such as high-order dispersion and nonlinear loss. This scheme provides a feasible way for on-chip pulse compressors with both large compression factor and high pulse quality. Nevertheless, the operation region is limited in the MIR bands. To further improve the compression factor of self-similar PC at the MIR bands, Cheng et al. numerically designed a suspended inversely tapered Si strip waveguide for high-degree self-similar PC [168]. The specially designed suspended structure aims at reducing the material loss of silica substrate at the MIR band. A 1.5-ps input fundamental soliton at pump wavelength of 2.25 μm was compressed to 46.73 fs in a 2.79 cm-long Si taper. The generated femtosecond pulse was then utilized to pump another Si strip waveguide for octave-spanning and highly coherent supercontinuum generation. Table 3 summarizes the reported PC in MNPWs by different waveguide structures and compression methods.

From the aspect of compression ratio, nonlinear absorption compression shows the best performance. However, nonlinear absorption only works efficiently for pulses whose durations are comparable with the free carrier lifetime and not less than nanosecond. In addition, the input energy is largely consumed during the compression process, rendering it unsuitable for large-scale on-chip applications. Chirp compensation and SSC are better choices in terms of femtosecond pulse compression. In particular, the latter could work under rather low energy because of the slow-light enhanced nonlinearity. The compression ratio is nevertheless limited by the inherent drawbacks of SSC mechanism. While self-similar compression shows higher compression ratio and better compression quality, the waveguide structure is required to be tapered precisely. This is why there is no experimental realization of self-similar compression so far.

Table 3. PC with different schemes (References marked with "*" indicate experimental studies).

Material	Structure	Mechanism	Ratio	Refs.
Si	Cascaded channel	Chirp compensation	8.4	[154]
Si	Cascaded channel	Chirp compensation	7	[155]*
GaInP	PhCWs	SSC	5.17	[156]*
USRN	FGB	SSC	5.7	[157]*
USRN	Strip	SSC	8.7	[158]*
Si	PhCW	SSC	2.3	[159]*
As_2S_3	Nanowire	SSC	9.84	[160]
Si	Tapered strip	SSC	10	[161]
Si	Strip	Nonlinear absorption	25	[34]*
As_2S_3	Tapered slot	Self-similarity	12.3	[165]
Si	Tapered slot	Self-similarity	12.1	[166]
Si	Inversely tapered ridge	Self-similarity	17.46	[167]
Si	Suspended tapered strip	Self-similarity	32.1	[168]

3.2. Spectral Compression

SPC which occurs in the frequency domain has distinct physical dynamics during the compression process with respect to PC. For SPC, both low- and high-frequency components of injected spectrum move towards to the center frequency due to the interaction between dispersion and $\chi^{(3)}$ nonlinearity. Consequently, the intensity of center frequency component becomes much higher. The compressed spectrum has significantly improved brightness. The narrow-linewidth spectral source finds important applications in the all-optical ADC [169], optical coherence tomography [170], and coherent light source synthesis [171].

Until now, SPC has been widely reported only in fibers. In 2011, Chuang and Huang demonstrated both numerically and experimentally that adiabatic soliton SPC in a dispersion-increasing fiber [172]. An experimental SPC ratio of 15.5 was obtained using 350 fs positively chirped input pulse centered at 1.5 μm. Andresen et al. demonstrated efficient SPC of femtosecond pulses near the zero-dispersion wavelength in nonlinear photonic crystal fibers [173]. The highest measured compression factor is 21, and the spectral brightness increases by a factor of 5. The reports of SPC in MNPWs are still rare due to the short interaction length. In 2016, Mei et al. numerically investigated SPC for PP in a 4 cm-long Si_3N_4 channel waveguide [174]. The resulting maximum SPC ratio reached 25.8 over the whole propagation. Different input temporal profiles like Gaussian and hyperbolic secant were also studied for comparison. Parabolic profile is the best choice among the three initial profiles. This is because all temporal chirp of PP can be fully compensated due to its unique temporal waveform. The spectral pedestals of PP after SPC were as low as -15.5 dB, which is the lowest one among the three kinds of pulse profiles. The same group further numerically studied an efficient SPC of self-frequency shifted soliton in a chalcogenide strip waveguide in 2019. The combination of SPC and SSFS were further utilized in an integratable all-optical quantization scheme [175]. The SPC and SSFS in this work were simultaneously achieved due to joint engineering of dispersion and nonlinearity. Increasing anomalous GVD and decreasing nonlinear coefficient with wavelength are key to this type of SPC. As shown in Figure 17, when the incident peak power is 25 W, the spectrum was compressed from 52.04 nm to 7.23 nm, and the center wavelength is red-shifted by 17 nm. When the incident peak power was increased to 75 W, the spectrum was compressed from 52.04 nm to 10.64 nm, and the center wavelength was red-shifted by 190 nm. In MIR region, Cheng et al. numerically demonstrated SPC of a soliton pulse pumped at 2.4 μm in an adiabatically suspended Si waveguide taper in 2019 [176]. Simulation results showed that high-degree SPC with a factor up to 10.9 can be achieved in a 6-cm length when the input femtosecond pulse is chirp-free. The realization of the method strongly depends on the design of

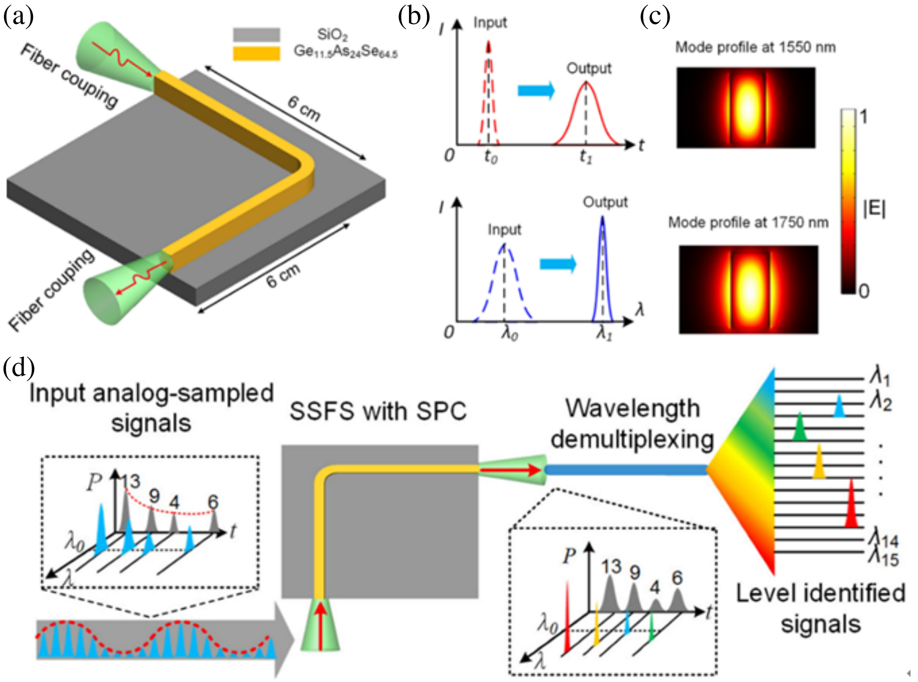

Figure 17. (a) The three-dimensional view and (b) the input and output pulses in the time and frequency domains. (c) Optical mode profiles of quasi-TE mode calculated at wavelengths 1550 and 1750 nm, respectively. (d) Schematic diagram of the all-optical quantization based on the SPC of soliton in the designed waveguide [175]. Copyright 2019 IEEE.

GVD and $\chi^{(3)}$ nonlinearity, i.e., by engineering the profiles of GVD and $\chi^{(3)}$ nonlinearity as a function of propagation distance. The achievable SPC factor is expected to be further improved after the geometric parameters of designed waveguide are further optimized.

3.3. Parabolic Pulse Generation

Special types of pulses can maintain their own shape during propagation and often called "similaritons". Optical soliton is the most typical and simplest example of a similariton that is able to propagate in a homogeneous medium with $\chi^{(3)}$ nonlinearity and anomalous GVD. When the anomalous GVD is slowly varied along the propagation, the parameters of soliton can be changed adiabatically so that the fundamental soliton condition is fulfilled automatically. Similar processes in a tapered medium are regarded as self-similar evolution, which has been analytically described by the well-known self-similar theory. Compared with solitons that do not exist in the normal dispersion regime, PPs keep their shape unchanged in the normal dispersion regime propagation for both active and passive waveguides. This is because PP does not suffer from the optical wave breaking in the normal dispersion regime. This is the main restriction for stable soliton propagation in high-power fiber amplification systems. Unlike soliton formation that requires a certain power threshold, PP has no requirement in initial shape, peak power, width, or phase. Mathematically, PP is the asymptotic solution of NLSE with constant gain coefficient and normal GVD. Input pulses with arbitrary temporal profiles will eventually evolve into PP provided the GVD and nonlinearity characteristics as a function of propagation distance satisfy certain conditions [177]. PP has many important applications in high-power pulse amplification, ultrashort pulse generation, optical cloaking, highly coherent SC generation, etc. Nevertheless, the time-domain profiles from most commercial pulsed laser sources are Gaussian, Lorentzian, or hyperbolic secant. Generation of PP inside a laser cavity without external assistance is challenging.

In the past two decades, several solutions have been proposed to generate PP externally. For example, PP generation has been fulfilled in rare-earth doped fiber amplifiers, such as Yb- and Er-doped fiber amplifiers [178, 179]. PP can be also generated in nonlinear Raman amplifiers [180] in which the gain spectrum is wider. While it is easy to get PP with high power from many amplifiers, active devices raise problems such as increasing system complexity and strong spontaneous emission noise. Therefore, PP generation by passive schemes should be considered [181]. According to the self-similar theory, PP can be generated in passive waveguides if its GVD and nonlinearity profiles are designed suitably. This is because varied GVD and nonlinearity along the propagation are equivalent to the gain imposed by active amplifiers [182]. Therefore, how to design the dispersion and nonlinearity becomes the key problem for PP generation in passive waveguides. Passive generation of PP in dispersion-decreasing tapered fiber [183], GVD-decreasing comb fiber [184], and two cascaded normal GVD fibers have been reported [185]. However, due to the inherently low nonlinearity, inflexible dispersion tailoring, and limited transparent window of single-mode fiber, aforementioned methods usually require long propagation length and limited operation bands. Therefore, PP generation on the MNPW platforms is a promising research direction.

In 2013, Lavdas et al. numerically studied PP generation in tapered Si MNPWs at both telecom ($\lambda = 1.55\,\mu\text{m}$) and MIR ($\lambda = 2.2\,\mu\text{m}$) regions [186]. Simulations results showed that in the normal dispersion regime, the input Gaussian pulse could evolve into PP in tapered Si nanowires with less than 6-mm length. The initial super-Gaussian pulse can evolve into a PP within the smallest waveguide length of 3 mm. The proposed waveguide structures and corresponding simulation results are shown in Figure 18. Lavdas et al. numerically investigated the generation and collision of optical similaritons in dispersion-engineered Si nanowires [187]. Optical similaritons were confirmed to be maintained well in the collision process even with presence of nonlinear absorption. The interaction between similaritons was found to strongly depend on the conditions under which the collision occurs. In 2017, Mei et al. theoretically presented a comprehensive study of PP generation in tapered hydrogenated amorphous Si nanowires due to its relatively large nonlinearity compared with monocrystalline Si [188]. The self-similar theory with single parameter variation is analytically studied to guide the waveguide design. Two tapered nanowires can be designed to be nonlinearity increasing or dispersion decreasing along the propagation. In another report, they also studied the PP generation in a Si taper with jointly engineered dispersion and nonlinearity [189]. GVD and nonlinearity can be varied simultaneously along the propagation. The relationship between GVD and nonlinearity was reconstructed so that the Si taper

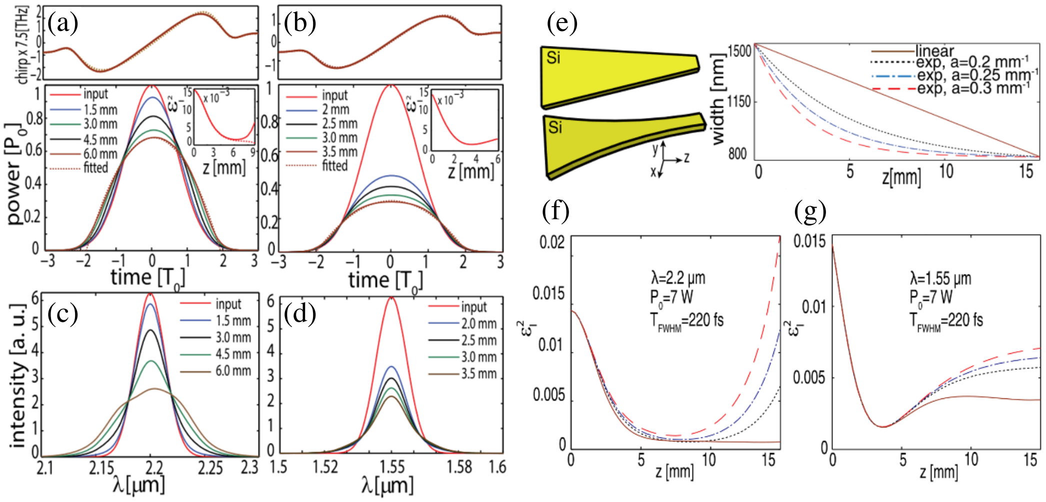

Figure 18. (a) and (b) Temporal pulse at different propagation points and the chirp of the output pulse, for the full model (solid line) and for $\beta_3 = 0$ and $\tau = 0$ (dotted line) (top panels). The insets show mismatch parameter versus z, for the full model (solid line) and for $\beta_3 = 0$ and $\tau = 0$ (dotted line). (c) and (d) The corresponding spectra of temporal pulses in (a) and (b). The panels to the left (right) correspond to $\lambda = 2.2\,\mu\text{m}$ ($\lambda = 1.55\,\mu\text{m}$). (e) Schematics (on the left) and dependence of $w(z)$ for linear and exponential tapers (on the right), (f) and (g) ε_{I^2} versus z for the tapers in (e) [186]. Copyright 2013 OSA.

can be designed by using the bisection algorithm. Multi-wavelength PPs generation were also studied in tapered Si nanowires by Mei et al. [190]. In this work, the coupled inhomogeneous NLSE was derived and employed to model the influence of XPM in the presence of nonlinear absorption and free carrier effects. Simulation results showed that wavelength interval between the pump center wavelengths and waveguide length are two critical factors that determines the quality of generated multi-wavelength PPs.

Although passive generation of PP on MNPW platforms has been theoretically studied, there is still no experimental demonstration so far. Experimental generation of PP in MNPWs should be feasible with the current mature fabrication technology because the required waveguide tapers with similar profiles have already been successfully and accurately fabricated for linear MNPW functionalities. Additionally, the required taper profiles for PP generation is not as strict as that required by self-similar PC, so fabrication defects are tolerable.

4. ALL-OPTICAL SIGNAL PROCESSING

Signal processing is critical for information extraction, transformation, correction, and analysis. According the type of signal to be dealt with, signal processing can be generally classified as two branches, i.e., analog and digital signal processing, which have been utilized in electric devices such as computers, mobile phones, as well as televisions. Due to the growing demand on information capacity, especially the recently developed high throughput 5G technology, cloud computing, and data center, traditional electronics are inadequate because the processing speed is severely limited by the electronic response of ns level [191]. The electron-electron interactions may also induce the inherent aperture jitter as well as comparator ambiguity, which degrade the quality of signal processing. Compared with electrons, photon-photon interactions have superior response time and lower jitter and noise due to the passive operation [192]. Optically assisted signal processing can improve the system performance in which the photons are used as the information carriers [193]. However, this kind of system requires the transition process of optical-to-electrical-to-optical conversion which would inevitably introduce additional noise, response limitation, and system complexity. Consequently, the efficiency of signal processing is reduced. To avoid this drawback of O-E-O conversion, all-optical signal processing (AOSP) in which the electronic signal is not needed anymore has attracted much attention. AOSP not only improves the speed of signal processing but also increases the system capacity. Study on AOSP was initially started from optical switching and temporal de-multiplexing, and has grown into extensive functionalities such as wavelength conversion, format conversion, 3R regeneration, filtering, mode conversion, logic gate, photonic ADC, etc. So far, chip-scale AOSP devices are still underdeveloped compared with the mature electronic signal processor. Several chip-scale AOSP advances are discussed.

4.1. All-Optical Analog-to-Digital Converter

ADC transforms analog signals to digital ones, bridging the real and virtual worlds because most information in our lives is naturally analog. High performance ADCs are the key components in real-time signal acquiring and processing systems, ultra-high speed optical communication systems and advanced radar. However, electronic ADCs show inevitable trade-off on the quantization resolution and operation bandwidth due to the inherent timing jitter of electronic sampling clock aperture and ambiguity of electronic comparator. The effective resolution of traditional electrical ADCs will be severely degraded if the sampling rate is several tens of gigahertz. The development of mode-locked laser sources with ultralow timing jitter (several and even sub-femtoseconds) avoids the trade-off by means of photonic ADC, which uses optical sampling and quantization [194–196]. While traditional electrical ADC has limited response time and bandwidth, photonic ADC can avoid these inherent electronic bottlenecks and is a promising method for future high-speed signal processing [197]. In the past two decades, some key developments for ADC such as time-stretching or time-interleaving techniques that combine with electronic ADCs, phase-shifted optical quantization technique, and all-optical approaches based on nonlinear optical effects have been reported [195, 197, 198]. The former methods still rely on the active device such as electronic ADCs and electro-optic modulators and aim to digitize the electrical analog signals. The latter all-optical ones based on nonlinear optical effects are fully passive, which directly digitize optical analog signals without prior optic-electro conversion. All sub-modules can be accomplished in the optical domain, e.g., the sampling, quantization, and encoding. Consequently, the disadvantage of electrical components can be conquered by only using passive devices. FWM and XPM can be employed to realize high-speed all-optical sampling [199, 200]. The SSFS, SPM, and XPM effects have been used to fulfill high-resolution of all-optical quantization [201, 202].

The principle of all-optical sampling is very similar to the parametric time-division de-multiplexing. The optical analog signal can be sampled through a FWM process at high speed from several to hundreds of gigahertz. To increase the sampling rate, Bres et al. proposed a scheme for real-time processing of arbitrary optical signals named multicast parametric synchronous sampling [203]. The main idea is that by utilizing a multicast FWM process to replicate sampling pump pulses, a multiplication of the

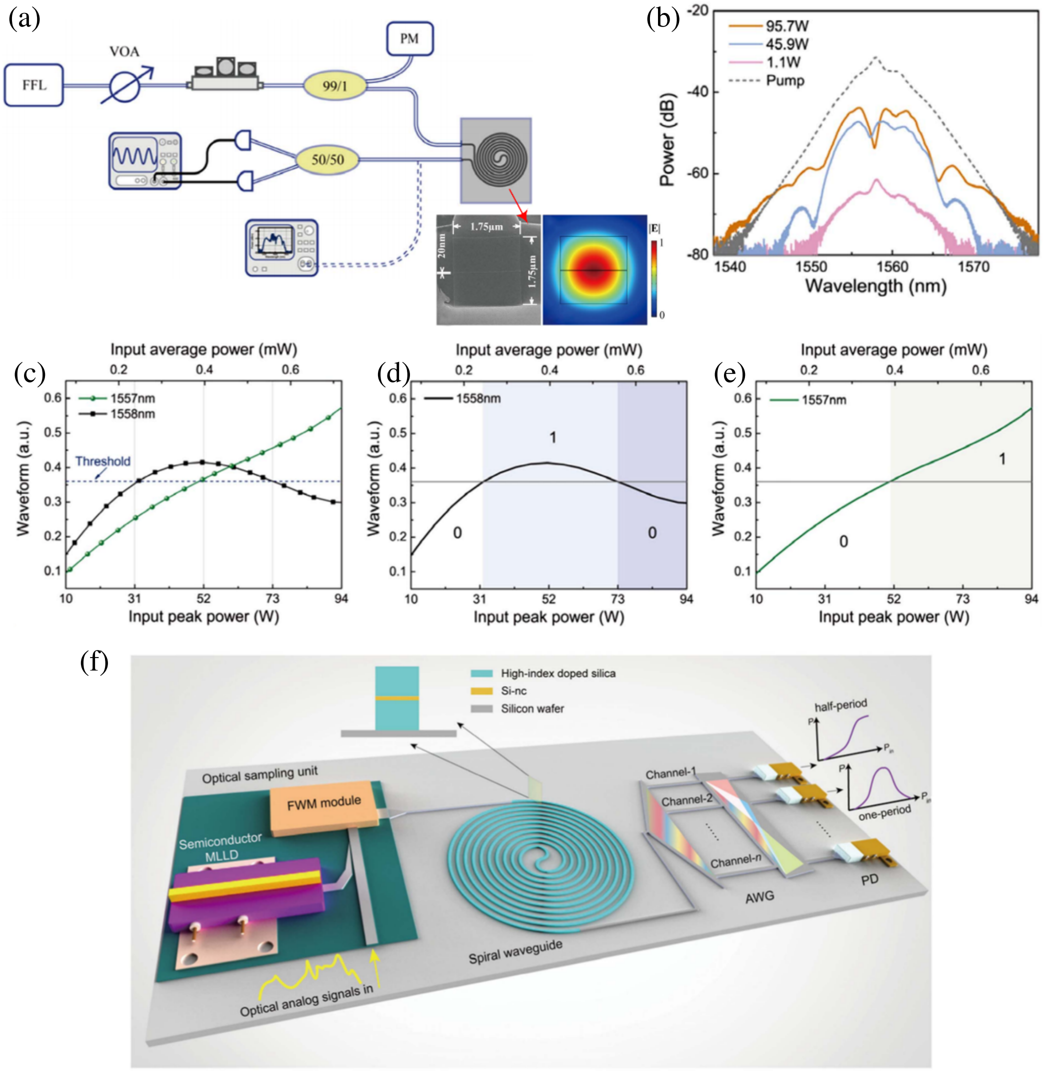

Figure 19. (a) Experimental setup (FFL, femtosecond fiber laser; VOA, variable optical attenuator; PM, power meter). The insertions show SEM image for the waveguide with a thin layer of 20 nm Si-nc in the core center and the corresponding simulated electric field profile of the quasi-TE polarization. (b) Measured spectral profiles at the output of the 50 cm Si-nc loaded waveguide (1.75 μm × 1.75 μm) with different input pump peak powers. (c) Measured power transfer functions of the two quantization channels by filtering the spectrum at the wavelengths of 1557 and 1558 nm, respectively. (d), (e) Power transfer functions of the two channels with binary decision results. (f) Schematic diagram of the proposed all-optical ADC. MLLD, mode-locked laser diode; AWG, arrayed waveguide grating; PD, photodiode [202]. Copyright 2019 OSA.

sampling rate is achieved. The amount of multiplication is proportional to the number of broadcasted replications. Some subsequent works have focused on increasing the number of broadcast replications. However, a large number of replications would make the structure complex and require large parametric gain bandwidth. In particular, the fluctuation of gain efficiency between replicated signals will degrade the sampling performance.

All-optical quantization is another key module for all-optical ADC. All-optical quantization can be divided into three branches from the view of power to intensity, phase, and frequency mapping. Recently, all-optical ADC on nonlinear MNPW platforms has become a hot topic because it meets the requirement of future CMOS-compatible on-chip potential with low power consumption. However, most of the reported works are still theoretical. For example, Miao et al. proposed 2-bit all-optical ADC in photonic crystal waveguide by using intensity quantization [204]. Kang et al. proposed a phase quantization scheme by using the XPM effect in a Si-organic hybrid slot waveguide based nested interferometer structure [205]. For the frequency quantization, Kang et al. proposed a CMOS-compatible 2-bit optical spectral quantization scheme using a Si-nanocrystal-based horizontal slot waveguide [206]. Kang et al. proposed an all-optical quantization scheme by slicing the SC generated in a chalcogenide horizontal slot waveguide [207]. SSFS is another nonlinear effect that can be used to realize frequency-based all-optical quantization since the central wavelength of red-shifted solitons will always be directly proportional to input peak power. Kang et al. designed a chalcogenide-silicon slot waveguide for integratable all-optical spectral quantization [208]. Zhang et al. modified this scheme by designing a cascaded chalcogenide-silicon slot waveguide [209]. While the quantization resolution was improved, the waveguide structure is more complicated because the cascaded structure increases the difficulty in facet coupling. To solve this problem, Mei et al. proposed an integratable all-optical quantization scheme by using the efficient SPC of self-frequency shifted soliton [175].

Experimentally, in 2019, an on-chip 2-bit all-optical ADC was demonstrated on a 50 cm-long strip-loaded hybrid waveguide comprising of Si-nanocrystal (Si-nc) strip and highly doped silica cladding [202]. Figure 19 shows the experimental setup of this scheme. The waveguide simultaneously possesses low loss (0.16 dB/cm), large nonlinearity ($305\,\mathrm{W}^{-1}$/km), and negligible nonlinear absorption, enabling power-efficient operation. The average power of only 0.72 mW, peak power of 94.2 W, and energy consumption of 19.55 pJ/bit fulfilled the 2-bit ADC. This experiment makes the CMOS-compatible and power-efficient all-optical ADC based on $\chi^{(3)}$ nonlinearity a reality. There is potential for fully monolithic solutions for all-optical ADC, in which integrated pulsed laser source and photodiodes are the key components waiting for better solutions.

4.2. All-Optical Logic Gate

The concept of all-optical logic gate (AOLG) with photonic circuits was developed in the mid-1980s [210]. It is one of the basic units in the AOSP system. Nonlinear Fabry-Perot etalons were used to realize the AOLG [211]. However, this kind of device is too bulky to meet the requirement of integration and low power consumption. This barrier prevented the development of the AOLG until the maturation of micro/nano-fabrication technology after 1990s. Schemes of chip-scale AOLG have been proposed by using strip waveguide, nested microresonator array, PhCW, and quantum-dot semiconductor optical amplifier (QD-SOA), etc. Based on these MNPWs, not only simple functions such as AND, OR, XOR, and NOT, but also the complex ones such as adder, multiplier, and comparator can be realized.

In 2017, Wang et al. demonstrated on-chip dual-channel all-optical AND gate using FWM in a multimode Si cascaded directional coupler [212]. The idlers of FWM products in the multimode waveguide carried the AND logic result and output at different ports according to the mode order. Two 5 Gb/s OOK signals are used in the experiment as a proof of concept, resulting in an aggregate bit rate of 10 Gb/s. In 2019, Wu et al. numerically studied the impact of TPA and free-carrier effects on all-optical logic gates in Si waveguides [213]. The conversion efficiency was found to be greatly reduced and the waveform was seriously distorted. Then, a Si-organic hybrid dual-slot waveguide with extremely large nonlinear parameter higher than $1.4 \times 10^{7}\,\mathrm{W}^{-1}$/km and without TPA was designed for FWM-based all-optical logic gates with AND, OR, and XOR functions in the C-band. Power consumption is one of the key performance indices of AOLG. The low loss strip waveguides, nonlinear microresonators with high Q-factors and small mode volume provide power-efficient and scalable solutions for AOLG. Nonlinear effects such as FWM, SPM, and XPM can be observed at a low pump power due to the dramatic

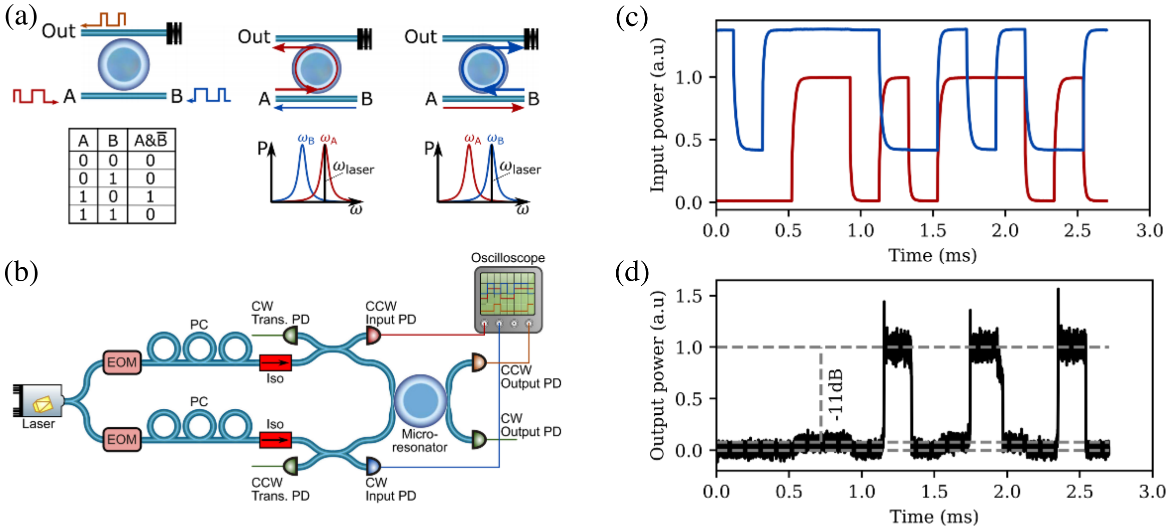

Figure 20. (a) Principle of the logic gate. (b) Experimental setup. A laser beam is split into two branches, corresponding to inputs A and B. Each input is independently amplitude modulated by a Mach-Zender EOM and has its polarization matched to that of the resonant mode using a polarization controller. (b) The measured powers input into the tapered fibers in both directions. Inputs A and B are both amplitude modulated by the same amount, but with B having a positive offset in order to suppress the output when both inputs are HIGH. (c) The measured output field, which can be seen as HIGH only when input A is HIGH and input B is LOW, showing the correct operation of an A&B gate. When both inputs are HIGH the output is not fully suppressed, which can be seen by the slight increase between 0.5 and 1 ms [214]. Copyright 2020 IEEE.

intracavity enhancement of pump energy. Using the FCD effect in Si, the AND and NAND functions at 310 Mbit/s rate were achieved with 10-dB extinction ratio and 2 mW average power consumption. In 2020, Moroney et al. demonstrated an all-optical universal logic gate using counter-propagating light waves at the same operating frequency [214], as shown in Figure 20. A high Q-factor (2×10^8) fused silica microrod resonator acts as the nonlinear medium. Kerr interaction between the two counter-propagating light waves leads to an intensity dependent appreciable refractive index change of the microresonator, which induces a splitting between the resonance frequencies for the two propagating directions. Arbitrary input signals at a power difference of 11 dB between output “1” and “0” states were demonstrated. This method works regardless of the choice of input ports. Accordingly, the gate can be reconfigured to work in different directions with minimal changes required. Despite the laboratory success, the fact that high requirements of robustness and mass fabrication still prevent the commercialization of microresonator-based AOLGs.

On the platform of PhCWs, Jandieri et al. numerically proposed an all-optical multiple-input AND gate on a coupled Kerr-type nonlinear air hole PhCW (C-PCW) in 2018 [215]. The gate can be modified for an all-optical multiple-input OR gate. In 2020, Kumar and Sen numerically studied all-optical NOT gate by using a PhCW-based nonlinear Mach-Zehnder interferometer. Silicon-nc/$\mathrm{SiO_2}$ slot structure comprised the nonlinear arm of the MZI [216]. The device worked in the power range of $28 \sim 60$ mW at a pulse width of 3 ps. The overall dimension of the device could be only $\sim 112 \times 7\,\mu\mathrm{m}^2$. Tolerances of the fabrication defects were also analyzed by introducing random variations in the positions and radius of the air holes. In 2020, Vakhtang et al. presented a conceptual study on the realization of functional and easily scalable all-optical NOT, AND, and NAND logic gates using bandgap solitons in coupled PhCWs [217]. Taking the all-optical NOT logic gate as an example, the schematic view of the structure consisting of three symmetric coupled PhCWs is shown in Figure 21. A CW signal, whose electric field is polarized parallel to the slab plane, with a normalized amplitude of $A = 0.956$ was launched into the coupled PhCWs through the middle Port-2. This port can be viewed as an “enable pin” of the NOT logic gate in which the presence of the CW signal corresponds to the “on” instruction that is common

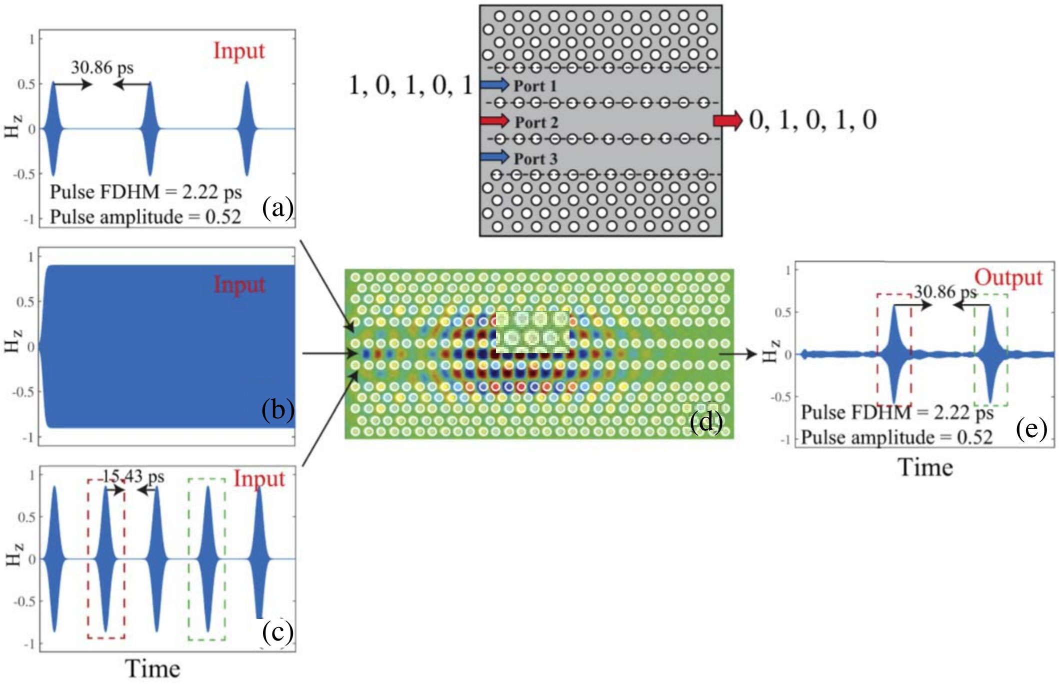

Figure 21. All-optical NOT logic gate: (a) three Gaussian pulses with amplitude of 0.52, full duration at half maximum (FDHM) of 2.22 ps and repetition time of 30.86 ps are launched into Port 1; (b) a CW with amplitude of 0.956 is injected into Port 2; (c) a train with amplitude of 0.812, FDHM of 2.22 ps and repetition time of 15.43 ps is launched into Port 3; (d) magnetic field distribution of the signal pulses; (e) magnetic field of the received signal [217]. Copyright 2020 OSA.

in digital electronics. Signal pulses were launched into Port-1, and another probe pulses with higher amplitude and half of the period were launched into Port-3. The output signal from Port-2 is the part of the probe pulses that does not overlap with the signal pulses, thus achieved the NOT gate operation.

QD-SOA is another candidate for chip-scale AOSP, which has compact volume and harnesses cross-gain modulation (XGM), cross-polarization modulation (XPolM), and XPM effects to realize logic functionality. QD-SOA scheme was proposed because the gain-recovery response (usually $10 \sim 300\,\text{ps}$) is much faster than the bulk SOAs. In 2013, Dimitriadou et al. numerically proposed an all-optical XOR gate using QD-SOA assisted by a detuned optical filter [218]. Pulsed signals at two wavelengths interacted with the QD-SOA and imposed a gain and phase variation on the third CW signal through XGM and XPM. By setting suitable blue-shifted amount, bandwidths, and shapes, the XOR gate could be executed with both logical correctness and high quality. In 2019, Kotb et al. numerically proposed a XOR gate with speeds up to Tbit/s. The logic gate was achieved by using QD-SOA based turbo-switched Mach–Zehnder interferometer [219].

4.3. Ultra-Broadband Radio-Frequency Photonics

Radio-frequency (RF) photonics includes microwave and millimeter wave photonics techniques. The applications cover the fields of telecommunications, radar, sensing, etc. [220]. The history of RF dates back to the 1970s, which is in parallel to the development of fiber optics. RF still attracts lots of interests because numerous new applications have been successively developed, such as ultra-wide-band analog signal transmission and processing, arbitrary waveform generation, phased arrays, photonic ADCs, spectral filters, etc. A typical procedure for RF photonics includes the following three steps. First, the optical carriers are modulated by the ready-for-process RF signal. Then, the optical signal generated by the modulator is processed in the optical domain. Finally, the optical signal processed is converted back to RF signal. Conventional methods for RF signal processing based on solid-state Ti:Sapphire or fiber lasers have little room for improvement. The repetition rate and central frequency of solid-state or fiber laser cannot be adjusted flexibly, which is crucial for the arbitrary waveform generation. New types of source such as microresonator-based Kerr microcomb are a promising candidate to replace conventional multi-wavelength sources for chip-scale RF photonics [221–225], whose comb tooth interval can be flexibly controlled within 10 GHz ∼ 1 THz to fulfill the RF scale.

RF photonics true time delay lines (TTDLs) which are the basic unit in the modern radar and communications systems, can be improved as the number of delay channels increases. Ultra-broadband RF photonics has been applied in TTDLs [226] in which a Kerr microcomb source generated in microresonator provided more than 81 wavelength channels over the C band for microwave signal processing. As a result, not only the performance can be improved, but also the size can be remarkably reduced [227]. This microring has a radius of 592 μm with a free spectral range of 0.4 nm, i.e., ∼ 49 GHz. Due to the ultralow loss of the microring, the resonance linewidth is only 1.2 pm around 1550 nm, resulting in a Q factor as high as 1.2×10^6. In 2018, Xu et al. proposed and experimentally demonstrated RF photonics channelizers using a Kerr microcomb source [228]. With an RF channelizing bandwidth of 90 GHz, a high RF spectral slicing resolution of 1.04 GHz and RF performance up to 19 GHz were experimentally achieved. The operating principle of the RF photonics channelizers is to slice the input RF spectrum into multiple segments, and then a bandwidth within the capability of digital electronics will exist in each segment, so that digital tools can process the analog RF signals. Through electro-optical modulators, the RF spectra are multicasted in all shaped microcomb wavelength channels. Then, a periodic optical filter slices the spectra. Eventually, all channels are separated in demultiplexers and

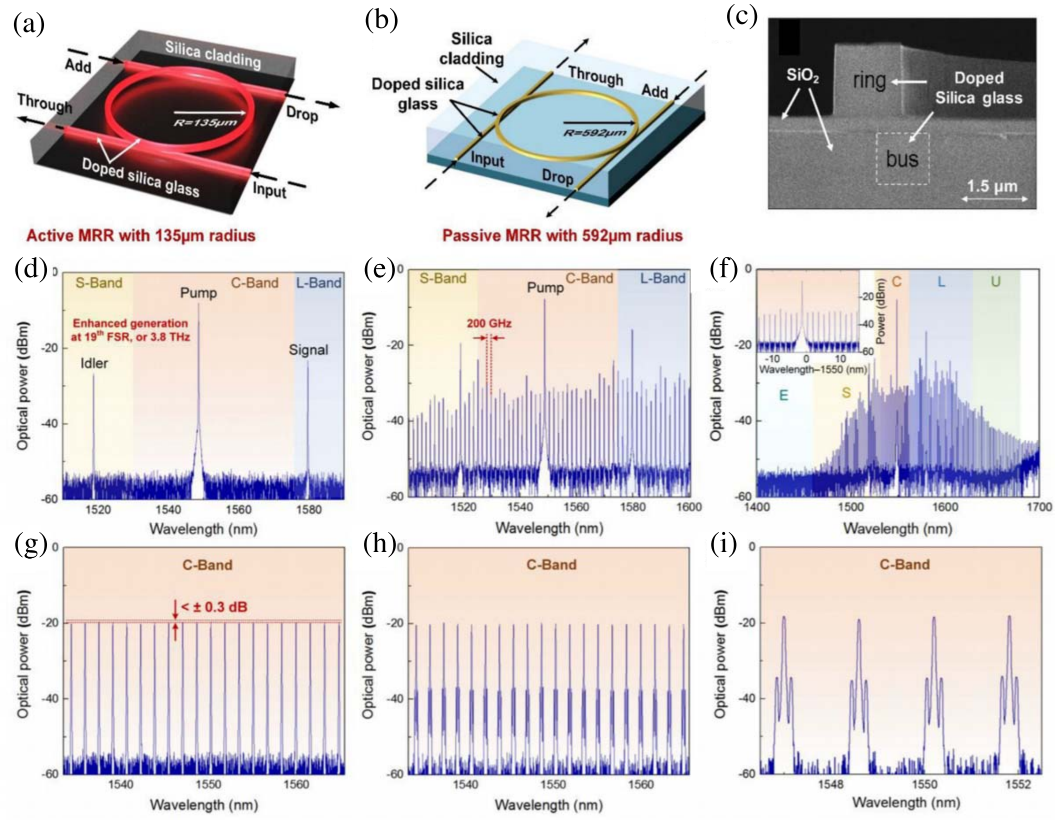

Figure 22. Schematic diagram of (a) 200 GHz-FSR and (b) 49 GHz-FSR microring. (c) SEM image of the cross-section of 200 GHz microring before depositing silica as upper cladding, optical spectra of (d) the primary, (e) secondary combs, (f) Kerr microcomb with 300 nm span, (g) shaped optical comb for channelizer with less than 0.5 dB unflatness, (h) 20 and (i) selected 4 comb lines modulated by RF signals [228]. Copyright 2018 OSA.

converted into the electrical domain for further processing. Figure 22 shows the active microring with 135 µm radius utilized, along with the performance of Kerr microcomb generation and channelization. The Kerr microcomb generated is rather broad, leading to 20 comb lines (channels) covering the whole C-band. The comb lines were then shaped to uniform channel weights and served as multi-wavelength carriers. A phase modulator was then followed to multicast the input RF signal onto each of the comb lines to complete the channelization process.

Quite recently, Hu et al. experimentally demonstrated all-optical reconfigurable RF filters by using soliton state Kerr microcombs [229]. Reconfigurability (shifting the filter passband frequency) was achieved by flexible manipulation of the spectral interference pattern of two-soliton state through controlling the temporal interval between the two solitons. The proposed RF filters have no additional pulse-shaping unit. The synthesized RF filters could be all optically reconfigured through the versatile soliton states switching. The perfect soliton crystals were triggered in a deterministic way to multiply the comb line spacing so that RF passband filtering frequencies can be divided. Figure 23 shows the schematic diagram of the reconfigurable RF photonic filters and the Kerr microcomb generation.

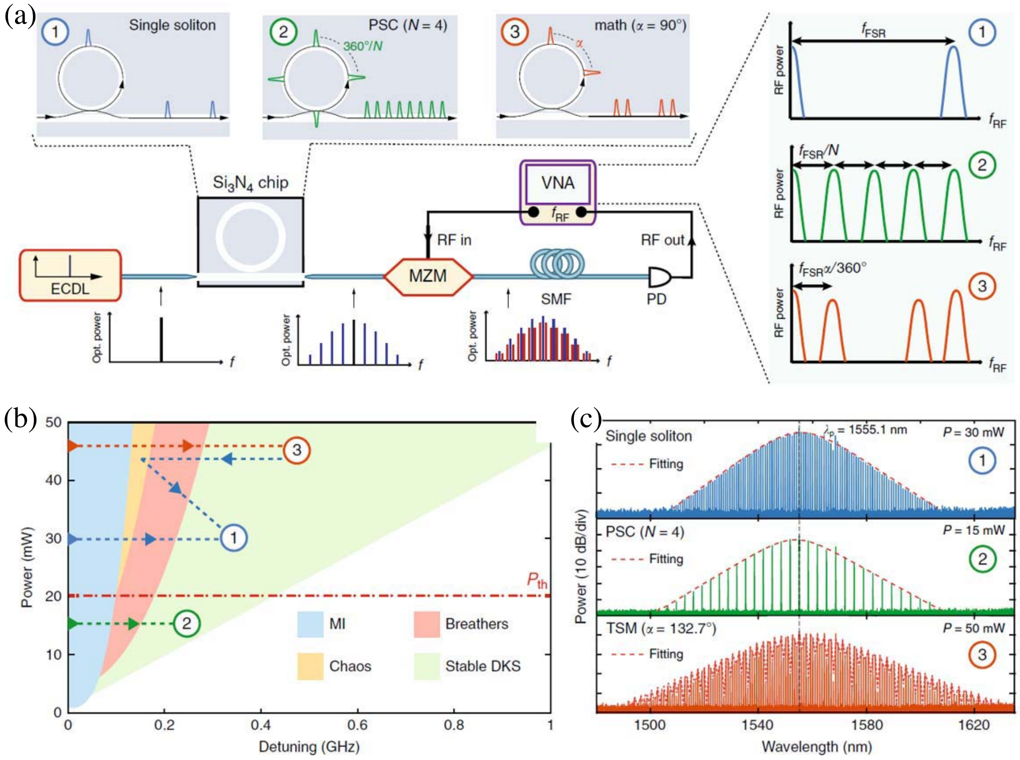

Figure 23. (a) The conceptual setup includes four parts: microcomb generation, RF signal upconversion, dispersive propagation, and photodetection. ECDL means external cavity diode laser, MZM means Mach-Zehnder modulator, PD means photodiode, VNA means vector network analyzer. Different RF filters are synthesized based on soliton state: (1) single-soliton-based RF filter with a passband centered at f_{FSR} (blue); (2) perfect soliton crystals of N equally spaced solitons within one round-trip based RF filters with a passband centered at f_{FSR}/N (green, $N = 4$ is shown); (3) two-soliton microcomb-based RF filters with a passband centered at $f_{FSR}\alpha/360^\circ$ (orange), ($\alpha = 90^\circ$ is shown). (b) Simulated stability diagram of LLE involving the experimental avoided mode crossing (AMX) condition. Four different stability regions are listed: modulation instability (MI, blue), breathers (red), spatio-temporal and transient chaos (chaos, yellow), and stable dissipative Kerr soliton (DKS, green). (c) Examples of experimentally generated spectra at resonance of 1555.1 nm: (1) single-soliton, (2) perfect soliton crystals ($N = 4$), and (3) two-soliton microcomb ($\alpha = 132.7^\circ$) [229]. Copyright 2020 Nature Publishing Group.

5. SUMMARY AND OUTLOOK

In this paper, we have reviewed progress on applications of coherent sources generation, pulse shaping, and all-optical signal processing using $\chi^{(3)}$ nonlinear effects in MNPWs. There are still broad opportunities for future studies. For example, flattened and broadband SC generation beyond $8\,\mu$m with reasonable conversion efficiency (or spectrum brightness) is still lacking on chip-scale platforms. Harnessing fully-fiber-based femtosecond pump sources instead of the solid-state sources is step forward for on-chip SC sources satisfying field-deployable, but is still rarely studied. Generation of on-chip Kerr soliton microcomb, especially the single soliton microcomb, in the UVR, VR, and deep MIR ($> 4\,\mu$m) regions remains challenging. The reported works of on-chip intermodal FWM is still confined to the well-established bands. The great potential on invading the new bands is waiting to be further explored. Experimental realization of on-chip pulse compression with factor larger than 10 has not been reported due to the high loss and short waveguide length of MNPWs. There is still no experimental demonstration of self-similar compression reported so far. For the on-chip AOSP, mass and reconfigurable functionalities assemble on a single chip is the focus of future study. Accompanied with the assistance of AI computing sciences such as machine learning and deep learning, on-chip $\chi^{(3)}$ based AOSP can be more powerful and will undoubtedly contribute to the key units of future monolithic AI photonics chip.

Waveguides made up by newly developed nonlinear materials are being explored to pave the way for on-chip integratable nonlinear photonic circuits (PICs). Besides the traditional nonlinear materials with strong $\chi^{(3)}$ nonlinearity like Group IV semiconductors (Si, Ge, and their derivant), other materials like SiC [230], nano-$LiNbO_3$ [231], and Tantala (Ta_2O_5) [232] are also explored. These heterogeneous nonlinear materials could be combined to constitute hybrid nonlinear optical platforms. As a result, the power efficiency of optical devices can be improved. In addition, multiple zero dispersion points which can be obtained in hybrid MNPWs in the MIR regime is an important technology for flattened and broadband MIR SC generation [233, 234]. The nano-$LiNbO_3$ MNPW has become a research highlight because it can be flexibly controlled by multi-physics fields such as acoustic, thermal, and electric fields [235, 236].

Looking into the future, $\chi^{(3)}$ nonlinearity will be probably investigated in new materials and structures. These materials include the two-dimensional (2D) layered materials [237], epsilon-near-zero (ENZ) materials [238], and plasmonic materials [239]. All these materials are compatible with CMOS foundry because they can be dealt to be very thin to the sub-wavelength scale. The 2D layered materials exhibit giant nonlinearities. They have already enabled diverse new photonic devices fundamentally different from those built upon traditional SiO_2, Si, and chalcogenide platforms. The typical 2D layered materials include graphene [240], oxide graphene [241], MoS_2 [242], etc. An ENZ material can be understood as this: for a given change ($\Delta\varepsilon$) in the permittivity, the resulting change (Δn) in the refractive index n is given by $\Delta n = \Delta\varepsilon/(2\varepsilon^{1/2})$ in a lossless material. This change becomes large when the permittivity becomes small, which suggests that the ENZ frequencies of the material should give rise to strong nonlinear properties. A lot of unusual matter under ENZ conditions and their promise in applications have been reported [243]. The plasmonic platform requires metal layer. The efficiency of this process depends on the type and nanostructure of the employed metal. The resulting strong electromagnetic field significantly enhanced the nonlinear processes [244]. $\chi^{(3)}$ nonlinearity in artificial structures such as metasurface is a growing research direction [245]. Metasurface is a class of structured interfaces whose meta-atoms have spatially varying profiles. This kind of surface can efficiently modify the light-matter interaction with a single layer of meta-atoms. When the meta-atoms of 2D or quais-2D metasurfaces are made up of metallic or dielectric resonators, one can control the photonic characteristic such as polarization, phase, and amplitude at subwavelength resolution is feasible. In addition, the 2D metasurfaces is so thin that compact optical devices and even less optical loss is expected. The $\chi^{(3)}$ nonlinearity can be enhanced through ensemble of new kinds of materials and structures. For example, the ENZ material and metasurface can be combined to broaden the bandwidth of high-nonlinear region [244]. Giant nonlinear response can be realized from plasmonic metasurfaces [246]. Therefore, 2D layered material, ENZ materials, and plasmonic materials might be the future media for all-optical signal processing.

Multimode nonlinear optics has been largely studied in the step-index and grade-index multimode fibers [247]. Although the theory of pulse propagation in a multimode grade-index fiber has been studied more than forty years ago [248], the nonlinear interaction was experimentally observed [249] very recently thanks to the advances in fabrication and computation. Multiple optical modes provide an extra freedom to explore the nonlinear effects with the regard of the complicated modal interaction along the propagation. Up to date, multimode optical soliton propagation [250], spatial beam self-cleaning [251], intermodal nonlinear mixing [252] and geometric parametric instability [253, 254] have been studied in grade-index and step-index fibers. However, multimode nonlinearity in MNPW platforms has not been fully investigated because of the large group-velocity mismatch caused by high refractive index contrast. Tailoring the transverse refractive index distribution of MNPWs to reduce the group-velocity mismatch is potentially a promising way towards the study of multimode nonlinearity in MNPWs. Chip-scale integrated quantum photonics circuits provide implementation paths for the quantum computation, quantum communication, and quantum memory [255]. As a fundamental building block of quantum photonic circuits, single-photon sources have been generated by FWM Bragg scattering [256]. There will be more and more interesting applications of $\chi^{(3)}$ nonlinearities in newly emerged on-chip materials and platforms, which in turn, promotes the research progress of $\chi^{(3)}$ nonlinearities.

ACKNOWLEDGMENT

This work is partly supported by the National Natural Science Foundation of China (62075188, 61875238, 91833303), the National Key Research and Development Program of China (2017YFA0205700), the Natural Science Foundation of Zhejiang Province (LY21F050007), the Ningbo Science and Technology Project (No. 2018B10093), the Fundamental Research Funds for the Central Universities (2019FZA5002), the Research Grants Council, University Grants Committee of Hong Kong SAR (PolyU152241/18E, PolyU152471/16E), and The Hong Kong Polytechnic University (1-BBAJ, 1-ZVGB).

REFERENCES

1. Maiman, T. H., "Stimulated optical radiation in ruby," *Nature*, Vol. 187, No. 4736, 493–494, 1960.
2. Bloembergen, N., *Nonlinear Optics*, 3rd Printing, 1977.
3. Woodbury, E. J. and W. K. Ng, "Ruby laser operation in the near IR," *Proc. IRE*, Vol. 50, 2367, 1962.
4. Maker, P. D., R. W. Terhune, and C. M. Savage, "Intensity-dependent changes in the refractive index of liquids," *Phys. Rev. Lett.*, Vol. 12, 507–509, 1964.
5. Chiao, R. Y., C. H. Townes, and B. P. Stoicheff, "Stimulated Brillouin scattering and coherent generation of intense hypersonic waves," *Phys. Rev. Lett.*, Vol. 12, 592–595, 1964.
6. Carman, R. L., R. Y. Chiao, and P. L. Kelly, "Observation of degenerate stimulated four-photon interaction and four-wave parametric amplification," *Phys. Rev. Lett.*, Vol. 17, 1281–1283, 1966.
7. Kao, K. C. and G. A. Hockham, "Dielectric-fibre surface waveguides for optical frequencies," *Proceedings of the Institution of Electrical Engineers*, Vol. 113, No. 7, 1151–1158, IET Digital Library, 1966.
8. Ippen, E. P., "Low-power quasi-CW Raman oscillator," *Appl. Phys. Lett.*, Vol. 16, 303–305, 1970.
9. Ippen, E. P. and R. H. Stolen, "Stimulated Brillouin scattering in optical fibers," *Appl. Phys. Lett.*, Vol. 21, 539–541, 1972.
10. Stolen, R. H., "Phase-matched-stimulated four-photon mixing in silica-fiber waveguides," *IEEE J. Quan. Electron.*, Vol. 11, 100–103, 1975.
11. Stolen, R. H. and C. Lin, "Self-phase-modulation in silica optical fibers," *Phys. Rev. A*, Vol. 17, 1448–1453, 1978.
12. Chraplyvy, A. R. and J. Stone, "Measurement of cross phase modulation in coherent wavelength-division multiplexing using injection lasers," *Electron. Lett.*, Vol. 20, No. 24, 996–997, 1984.
13. Hasegawa, A. and F. Tappert, "Transmission of stationary nonlinear optical pulses in dispersive dielectric fibers: I. Anomalous dispersion," *Appl. Phys. Lett.*, Vol. 23, 142–144, 1973.

14. Mollenauer, L. F., R. H. Stolen, and J. P. Gordon, "Experimental observation of picosecond pulse narrowing and solitons in optical fibers," *Phys. Rev. Lett.*, Vol. 45, 1095–1098, 1980.
15. Mollenauer, L. F. and R. H. Stolen, "The soliton laser," *Opt. News*, Vol. 10, No. 6, 20_2-21, 1984.
16. Anderson, D. and M. Lisak, "Bandwidth limits due to mutual pulse interaction in optical soliton communication systems," *Opt. Lett.*, Vol. 11, No. 3, 174–176, 1986.
17. Wai, P. K. A., C. R. Menyuk, Y. C. Lee, and H. H. Chen, "Nonlinear pulse propagation in the neighborhood of the zero-dispersion wavelength of monomode optical fibers," *Opt. Lett.*, Vol. 11, 464–488, 1986.
18. Tai, K., A. Hasegawa, and N. Bekki, "Fission of optical solitons induced by stimulated Raman effect," *Opt. Lett.*, Vol. 13, 392–394, 1988.
19. Mitschke, F. M. and L. F. Mollenauer, "Discovery of the soliton self-frequency shift," *Opt. Lett.*, Vol. 11, 659–661, 1986.
20. Corkum, P. B., C. Rolland, and T. Srinivasan-Rao, "Supercontinuum generation in gases," *Phys. Rev. Lett.*, Vol. 57, No. 18, 2268, 1986.
21. Birks, T. A., P. J. Roberts, P. St. J. Russell, D. M. Atkin, and T. J. Shepherd, "Full 2-D photonic bandgaps in silica/air structures," *Electron. Lett.*, Vol. 31, 1941–1942, 1995.
22. Bouwmans, G., F. Luan, J. C. Knight, et al., "Properties of a hollow-core photonic bandgap fiber at 850 nm wavelength," *Opt. Express*, Vol. 11, No. 14, 1613–1620, 2003.
23. Yusoff, Z., J. H. Lee, W. Belardi, et al., "Raman effects in a highly nonlinear holey fiber: Amplification and modulation," *Opt. Lett.*, Vol. 27, No. 6, 424–426, 2002.
24. Nakajima, K., K. Hogari, J. Zhou, et al., "Hole-assisted fiber design for small bending and splice losses," *IEEE Photon. Technol. Lett.*, Vol. 15, No. 12, 1737–1739, 2003.
25. Vienne, G., Y. Xu, C. Jakobsen, et al., "First demonstration of air-silica Bragg fiber," *Optical Fiber Communication Conference*, Vol. 2, 3, Optical Society of America, 2004.
26. Habib, M. S., J. E. Antonio-Lopez, C. Markos, et al., "Single-mode, low loss hollow-core anti-resonant fiber designs," *Opt. Express*, Vol. 27, No. 4, 3824–3836, 2019.
27. Ferrera, M., L. Razzari, D. Duchesne, et al., "Low-power continuous-wave nonlinear optics in doped silica glass integrated waveguide structures," *Nat. Photon.*, Vol. 2, No. 12, 737, 2008.
28. Barrelet, C. J., H. S. Ee, S. H. Kwon, et al., "Nonlinear mixing in nanowire subwavelength waveguides," *Nano Lett.*, Vol. 11, No. 7, 3022–3025, 2011.
29. Li, G., J. Yao, H. Thacker, et al., "Ultralow-loss, high-density SOI optical waveguide routing for macrochip interconnects," *Opt. Express*, Vol. 20, No. 11, 12035–12039, 2012.
30. Solehmainen, K., "Fabrication of microphotonic waveguide components on silicon," *VTT Technical Research Centre of Finland*, 68, 2007.
31. Tsang, H. K., C. S. Wong, T. K. Liang, et al., "Optical dispersion, two-photon absorption and self-phase modulation in silicon waveguides at 1.5 μm wavelength," *Appl. Phys. Lett.*, Vol. 80, No. 3, 416–418, 2002.
32. Astar, W., J. B. Driscoll, X. Liu, et al., "Tunable wavelength conversion by XPM in a silicon nanowire, and the potential for XPM-multicasting," *J. Lightw. Technol.*, Vol. 28, No. 17, 2499–2511, 2010.
33. Liang, T. K. and H. K. Tsang, "Nonlinear absorption and Raman scattering in silicon-on-insulator optical waveguides," *IEEE J. Sel. Top. Quant. Electron.*, Vol. 10, No. 5, 1149–1153, 2004.
34. Tien, E. K., N. S. Yuksek, F. Qian, and Ä. O. Boyraz, "Pulse compression and mode locking by using TPA in silicon waveguides," *Opt. Express*, Vol. 15, No. 10, 6500–6506, 2007.
35. Liang, T. K., H. K. Tsang, I. E. Day, et al., "Silicon waveguide two-photon absorption detector at 1.5 μm wavelength for autocorrelation measurements," *Appl. Phys. Lett.*, Vol. 81, No. 7, 1323–1325, 2002.
36. Reitze, D. H., T. R. Zhang, W. M. Wood, et al., "Two-photon spectroscopy of silicon using femtosecond pulses at above-gap frequencies," *J. Opt. Soc. Am. B*, Vol. 7, No. 1, 84–89, 1990.
37. Eggleton, B. J., B. Luther-Davies, and K. Richardson, "Chalcogenide photonics," *Nat. Photon.*, Vol. 5, No. 3, 141, 2011.

38. Monat, C., B. Corcoran, M. Ebnali-Heidari, et al., "Slow light enhancement of nonlinear effects in silicon engineered photonic crystal waveguides," *Opt. Express*, Vol. 17, No. 4, 2944–2953, 2009.
39. Carletti, L., P. Ma, Y. Yu, et al., "Nonlinear optical response of low loss silicon germanium waveguides in the mid-infrared," *Opt. Express*, Vol. 23, No. 7, 8261–8271, 2015.
40. Ramirez, J. M., V. Vakarin J. Frigerio J, et al., "Ge-rich graded-index $\mathrm{Si}_{1-x}\mathrm{Ge}_x$ waveguides with broadband tight mode confinement and flat anomalous dispersion for nonlinear mid-infrared photonics," *Opt. Express*, Vol. 25, No. 6, 6561–6567, 2017.
41. Carletti, L., M. Sinobad, P. Ma, et al., "Mid-infrared nonlinear optical response of Si-Ge waveguides with ultra-short optical pulses," *Opt. Express*, Vol. 23, No. 25, 32202–32214, 2015.
42. Moss, J. D., R. Morandotti, A. L. Gaeta, et al., "New CMOS-compatible platforms based on silicon nitride and Hydex for nonlinear optics," *Nat. Photon.*, Vol. 7, No. 8, 597–607, 2013.
43. Liu, J., A. S. Raja, M. Karpov, et al., "Ultralow-power chip-based soliton microcombs for photonic integration," *Optica*, Vol. 5, No. 10, 1347–1353, 2018.
44. Stern, B., X. Ji, Y. Okawachi, et al., "Battery-operated integrated frequency comb generator," *Nature*, Vol. 562, No. 7727, 401–405, 2018.
45. Shen, B., et al., "Integrated turnkey soliton microcombs," *Nature*, Vol. 582, 365–369, 2020.
46. Choi, J. W., Z. Han, B. U. Sohn, et al., "Nonlinear characterization of GeSbS chalcogenide glass waveguides," *Sci. Rep.*, Vol. 6, No. 1, 1–8, 2016.
47. Ta'eed, V. G., M. R. E. Lamont, D. J. Moss, et al., "All optical wavelength conversion via cross phase modulation in chalcogenide glass rib waveguides," *Opt. Express*, Vol. 14, No. 23, 11242–11247, 2006.
48. Yeom, D. I., E. C. Mägi, M. R. E. Lamont, et al., "Low-threshold supercontinuum generation in highly nonlinear chalcogenide nanowires," *Opt. Lett.*, Vol. 33, No. 7, 660–662, 2008.
49. Ta'eed, V. G., M. Shokooh-Saremi, L. Fu, et al., "Self-phase modulation-based integrated optical regeneration in chalcogenide waveguides," *IEEE J. Sel. Top. Quant. Electron.*, Vol. 12, No. 3, 360–370, 2006.
50. Siviloglou, G. A., S. Suntsov, R. El-Ganainy, et al., "Enhanced third-order nonlinear effects in optical AlGaAs nanowires," *Opt. Express*, Vol. 14, No. 20, 9377–9384, 2006.
51. Inoue, K., H. Oda, N. Ikeda, et al., "Enhanced third-order nonlinear effects in slowlight photonic-crystal slab waveguides of line defect," *Opt. Express*, Vol. 17, No. 9, 7206–7216, 2009.
52. Moille, G., L. Chang, W. Xie, et al., "Dissipative Kerr Solitons in a III-V microresonator," *Laser & Photon. Rev.*, Vol. 14, No. 8, 2070043, 2020.
53. Combrié, S., Q. V. Tran, A. De Rossi, et al., "High quality GaInP nonlinear photonic crystals with minimized nonlinear absorption," *Appl. Phys. Lett.*, Vol. 95, No. 22, 221108, 2009.
54. Xiong, C., W. H. P. Pernice, X. Sun, et al., "Aluminum nitride as a new material for chip-scale optomechanics and nonlinear optics," *New J. Phys.*, Vol. 14, No. 9, 095014, 2012.
55. Munk, D., M. Katzman, O. Westreich, et al., "Four-wave mixing and nonlinear parameter measurement in a gallium-nitride ridge waveguide," *Opt. Mater. Express*, Vol. 8, No. 1, 66–72, 2018.
56. Pu, M., Y. Liu, et al., "Broadband optical signal processing in AlGaAs-on-insulator waveguides," *Integrated Photonics Research, Silicon and Nanophotonics*, Optical Society of America, ITu2A.1, 2020.
57. Chang, L., W. Xie, H. Shu, et al., "Ultra-efficient frequency comb generation in AlGaAs-on-insulator microresonators," *Nat. Commun.*, Vol. 11, No. 1, 1–8, 2020.
58. Gaeta, A. L., M. Lipson, and T. J. Kippenberg, "Photonic-chip-based frequency combs," *Nat. Photon.*, Vol. 13, No. 3, 158–169, 2019.
59. Dudley, J. M., G. Genty, and S. Coen, "Supercontinuum generation in photonic crystal fiber," *Rev. Mod. Phys.*, Vol. 78, No. 4, 1135, 2006.
60. Lin, Q., O. J. Painter, and G. P. Agrawal, "Nonlinear optical phenomena in silicon waveguides: Modeling and applications," *Opt. Express*, Vol. 15, No. 25, 16604–16644, 2007.

61. Dudley, J. M. and S. Coen, "Coherence properties of supercontinuum spectra generated in photonic crystal and tapered optical fibers," *Opt. Lett.*, Vol. 27, No. 13, 1180–1182, 2002.
62. Raabe, N., T. Feng, T. Witting, et al., "Role of Intrapulse coherence in carrier-envelope phase stabilization," *Phys. Rev. Lett.*, Vol. 119, No. 12, 123901, 2017.
63. Mei, C. and G. Steinmeyer, "Tailoring the waveguide dispersion of nonlinear fibers for supercontinuum generation with superior intrapulse coherence," *J. Opt. Soc. Am. B*, Vol. 37, No. 8, 2485–2497, 2020.
64. Oh, D. Y., K. Y. Yang, C. Fredrick, et al., "Coherent ultra-violet to near-infrared generation in silica ridge waveguides," *Nat. Commun.*, Vol. 8, No. 1, 1–7, 2017.
65. Liu, X., A. W. Bruch, J. Lu, et al., "Beyond 100 THz-spanning ultraviolet frequency combs in a non-centrosymmetric crystalline waveguide," *Nat. Commun.*, Vol. 10, No. 1, 2971, 2019.
66. Lafforgue, C., S. Guerber, J. M. Ramirez, et al., "Broadband supercontinuum generation in nitrogen-rich silicon nitride waveguides using a 300 mm industrial platform," *Photon. Res.*, Vol. 8, No. 3, 2020.
67. Genty, G., S. Coen, and J. M. Dudley, "Fiber supercontinuum sources," *J. Opt. Soc. Am. B*, Vol. 24, No. 8, 1771–1785, 2007.
68. Johnson, A. R., A. S. Mayer, A. Klenner, et al., "Octave-spanning coherent supercontinuum generation in a silicon nitride waveguide," *Opt. Lett.*, Vol. 40, No. 21, 5117–5120, 2015.
69. Okawachi, Y., M. Yu, J. Cardenas, et al., "Coherent, directional supercontinuum generation," *Opt. Lett.*, Vol. 42, No. 21, 4466–4469, 2017.
70. Kuyken, B., M. Billet, F. Leo, et al., "Octave-spanning coherent supercontinuum generation in an AlGaAs-on-insulator waveguide," *Opt. Lett.*, Vol. 45, No. 3, 603–606, 2020.
71. Tremblay, J., M. Malinowski, K. A. Richardson, et al., "Picojoule-level octave-spanning supercontinuum generation in chalcogenide waveguides," *Opt. Express*, Vol. 26, No. 16, 21358–21363, 2018.
72. Dave, U. D., C. Ciret, S.-P. Gorza, et al., "Dispersive-wave-based octave-spanning supercontinuum generation in InGaP membrane waveguides on a silicon substrate," *Opt. Lett.*, Vol. 40, No. 15, 3584–3587, 2015.
73. Singh, N., M. Xin, D. Vermeulen, et al., "Octave-spanning coherent supercontinuum generation in silicon on insulator from 1.06 µm to beyond 2.4 µm," *Light Sci. Appl.*, Vol. 7, No. 1, 17131–17131, 2018.
74. Kou, R., T. Hatakeyama, J. Horng, et al., "Mid-IR broadband supercontinuum generation from a suspended silicon waveguide," *Opt. Lett.*, Vol. 43, No. 6, 1387, 2018.
75. Chiles, J., N. Nader, E. J. Stanton, et al., "Multi-functional integrated photonics in the mid-infrared with suspended AlGaAs on silicon," *Optica*, Vol. 6, No. 9, 1246–1254, 2019.
76. Nader, N., A. Kowligy, J. Chiles, et al., "Infrared frequency comb generation and spectroscopy with suspended silicon nanophotonic waveguides," *Optica*, Vol. 6, No. 10, 1269, 2019.
77. Lau, R. K. W., M. R. E. Lamont, A. G. Griffith, et al., "Octave-spanning mid-infrared supercontinuum generation in silicon nanowaveguides," *Opt. Lett.*, Vol. 39, No. 15, 4518–4521, 2014.
78. Xie, S., N. Tolstik, J. C. Travers, et al., "Coherent octave-spanning mid-infrared supercontinuum generated in As_2S_3-silica double-nanospike waveguide pumped by femtosecond Cr: ZnS laser," *Opt. Express*, Vol. 24, No. 11, 12406–12413, 2016.
79. Sinobad, M., C. Monat, B. Luther-Davies, et al., "Mid-infrared octave spanning supercontinuum generation to 8.5 µm in silicon-germanium waveguides," *Optica*, Vol. 5, No. 4, 360, 2018.
80. Sinobad, M., A. D. Torre, R. Armand, et al., "High coherence at f and 2f of mid-infrared supercontinuum generation in silicon germanium waveguides," *IEEE J. Sel. Top. Quant. Electron.*, Vol. 26, No. 2, 1–8, 2019.
81. Yang, M., Y. Guo, J. Wang, et al., "Mid-IR supercontinuum generated in low-dispersion Ge-on-Si waveguides pumped by sub-ps pulses," *Opt. Express*, Vol. 25, No. 14, 16116, 2017.

82. Yuan, J., Z. Kang, F. Li, et al., "Mid-infrared octave-spanning supercontinuum and frequency comb generation in a suspended germanium-membrane ridge waveguide," *J. Lightw. Technol.*, Vol. 35, 2994–3002, 2017.
83. Jing, S., C. Mei, K. Wang, et al., "Broadband and highly coherent supercontinuum generation in a suspended As_2S_3 ridge waveguide," *Opt. Commun.*, Vol. 428, 227–232, 2018.
84. Cheng, Y., J. Yuan, C. Mei, et al., "Self-similar picosecond pulse compression for supercontinuum generation at mid-infrared wavelength in silicon strip waveguides," *Opt. Commun.*, Vol. 454, 124380, 2019.
85. Li, Z., J. Yuan, C. Mei, et al., "Multi-octave mid-infrared supercontinuum and frequency comb generation in a suspended As_2Se_3 ridge waveguide," *Appl. Opt.*, Vol. 58, No. 31, 8404–8410, 2019.
86. Lai, J., J. Yuan, Y. Cheng, et al., "Dispersion-engineered T-type germanium waveguide for mid-infrared supercontinuum and frequency comb generations in all-normal dispersion region," *OSAC*, Vol. 3, No. 9, 2320–2331, 2020.
87. Yu, M., B. Desiatov, Y. Okawachi, et al., "Coherent two-octave-spanning supercontinuum generation in lithium-niobate waveguides," *Opt. Lett.*, Vol. 44, 1222–1225, 2019.
88. Lu, J., X. Liu, A. W. Bruch, et al., "Ultraviolet to mid-infrared supercontinuum generation in single-crystalline aluminum nitride waveguides," *Opt. Lett.*, Vol. 45, No. 16, 4499–4502, 2020.
89. Gaeta, A. L., M. Lipson, and T. J. Kippenberg, "Photonic-chip-based frequency combs," *Nat. Photonics*, Vol. 13, 158–169, 2019.
90. Hon, N. K., R. Soref, and B. Jalali, "The third-order nonlinear optical coefficients of Si, Ge, and $Si_{1-x}Ge_x$ in the mid-wave and longwave infrared," *J. Appl. Phys.*, Vol. 110, 011301, 2011.
91. Wang, T., N. Venkatram, J. Gosciniak, Y. Cui, G. Qian, W. Ji, and D. T. H. Tan, "Multi-photon absorption and third-order nonlinearity in silicon at mid-infrared wavelengths," *Opt. Express*, Vol. 21, 32192–32198, 2013.
92. Shen, L., N. Healy, P. Mehta, T. D. Day, J. R. Sparks, J. V. Badding, and A. C. Peacock, "Nonlinear transmission properties of hydrogenated amorphous silicon core fibers towards the mid-infrared regime," *Opt. Express*, Vol. 21, 13075–13083, 2013.
93. Carletti, L., M. Sinobad, P. Ma, Y. Yu, D. Allioux, R. Orobtchouk, M. Brun, S. Ortiz, P. Labeye, J. M. Hartmann, S. Nicoletti, S. Madden, B. Luther-Davies, D. J. Moss, C. Monat, and C. Grillet, "Mid-infrared nonlinear optical response of Si-Ge waveguides with ultra-short optical pulses," *Opt. Express*, Vol. 23, 32202–32214, 2015.
94. Agrawal, G. P., *Nonlinear Fiber Optics, Nonlinear Science at the Dawn of the 21st Century*, 195–211, Springer, Berlin, Heidelberg, 2000.
95. Tan, D. T. H., K. Ikeda, P. C. Sun, et al., "Group velocity dispersion and self-phase modulation in silicon nitride waveguides," *Appl. Phys. Lett.*, Vol. 96, 061101, 2010.
96. Levy, J. S., A. Gondarenko, M. A. Foster, et al., "CMOS-compatible multiple-wavelength oscillator for on-chip optical interconnects," *Nat. Photonics*, Vol. 4, 37–40, 2010.
97. Cardenas, J., S. Miller, Y. Okawachi, et al., "Parametric frequency conversion in silicon carbide waveguides," *CLEO: Science and Innovations*, 1–3, Optical Society of America, 2015.
98. Jung, H., C. Xiong, K. Y. Fong, X. Zhang, and H. X. Tang, "Optical frequency comb generation from aluminum nitride microring resonator," *Opt. Lett.*, Vol. 38, 2810–2813, 2013.
99. Belt, M., M. L. Davenport, J. E. Bowers, and D. J. Blumenthal, "Ultra-low-loss Ta_2O_5-core/SiO_2-clad planar waveguides on Si substrates," *Optica*, Vol. 4, 532–536, 2017.
100. Guan, X., H. Hu, L. K. Oxenløwe, and L. H. Frandsen, "Compact titanium dioxide waveguides with high nonlinearity at telecommunication wavelengths," *Opt. Express*, Vol. 26, No. 2, 1055–1063, 2018.
101. Hausmann, B. J. M., I. Bulu, V. Venkataraman, P. Deotare, et al., "Diamond nonlinear photonics," *Nat. Photonics*, Vol. 8, 369–374, 2014.
102. Pu, M., H. Hu, L. Ottaviano, et al., "Ultra-efficient and broadband nonlinear AlGaAs-on-insulator chip for low-power optical signal processing," *Laser & Photon. Rev.*, Vol. 12, 1800111, 2018.

103. Dolgaleva, K., W. C. Ng, L. Qian, and J. S. Aitchison, "Compact highly-nonlinear AlGaAs waveguides for efficient wavelength conversion," *Opt. Express*, Vol. 19, 12440–12455, 2011.
104. Xiang, B.-X., et al., "Supercontinuum generation in lithium niobate ridge waveguides fabricated by proton exchange and ion beam enhanced etching," *Chinese Phys. Lett.*, Vol. 34, No. 2, 24203–024203, 2017.
105. Fan, Z., K. Yan, L. Zhang, J. Qin, J. Chen, R. Wang, and X. Shen, "Design and fabrication of As_2Se_3 chalcogenide waveguides with low optical losses," *Appl. Opt.*, Vol. 59, 1564–1568, 2020.
106. Al-kadry, A., C. Baker, M. El Amraoui, Y. Messaddeq, and M. Rochette, "Broadband supercontinuum generation in As_2Se_3 chalcogenide wires by avoiding the two-photon absorption effects," *Opt. Lett.*, Vol. 38, 1185–1187, 2013.
107. Duchesne, D., M. Ferrera, et al., "Efficient self-phase modulation in low loss, high index doped silica glass integrated waveguides," *Opt. Express*, Vol. 17, No. 3, 1865–1870, 2009.
108. Kuyken, B., T. Ideguchi, S. Holzner, et al., "An octave-spanning mid-infrared frequency comb generated in a silicon nanophotonic wire waveguide," *Nat. Commun.*, Vol. 6, No. 1, 1–6, 2015.
109. Carlson, D. R., D. D. Hickstein, A. Lind, et al., "Self-referenced frequency combs using high-efficiency silicon-nitride waveguides," *Opt. Lett.*, Vol. 42, No. 12, 2314–2317, 2017.
110. Lee, K. F., N. Granzow, M. A. Schmidt, et al., "Mid-infrared frequency combs from coherent supercontinuum in chalcogenide and optical parametric oscillation," *Opt. Lett.*, Vol. 39, No. 7, 2056–2059, 2014.
111. Guo, H., C. Herkommer, A. Billat, et al., "Mid-infrared frequency comb via coherent dispersive wave generation in silicon nitride nanophotonic waveguides," *Nat. Photon.*, Vol. 12, No. 6, 330–335, 2018.
112. Guo, H., W. Weng, J. Liu, et al., "Nanophotonic supercontinuum based mid-infrared dual-comb spectroscopy," *Optica*, Vol. 7, 1181–1188, 2020.
113. Grassani, D., E. Tagkoudi, H. Guo, et al., "Mid infrared gas spectroscopy using efficient fiber laser driven photonic chip-based supercontinuum," *Nat. Commun.*, Vol. 10, No. 1, 1553, 2019.
114. Tagkoudi, E., D. Grassani, F. Yang, et al., "Parallel gas spectroscopy using mid-infrared supercontinuum from a single Si_3N_4 waveguide," *Opt. Lett.*, Vol. 45, No. 7, 2195–2198, 2020.
115. Jung, H., R. Stoll, X. Guo, et al., "Green, red and IR frequency comb line generation from single IR pump in AlN microring resonator," *Optica*, Vol. 1, No. 6, 396–399, 2014.
116. Kippenberg, T. J., A. L. Gaeta, M. Lipson, et al., "Dissipative Kerr solitons in optical microresonators," *Science*, Vol. 361, eaan8083, 2018.
117. Haelterman, M., S. Trillo, and S. Wabnitz, "Dissipative modulation instability in a nonlinear dispersive ring cavity," *Opt. Commun.*, Vol. 91, Nos. 5–6, 401–407, 1992.
118. Kang, Z., F. Li, J. H. Yuan, et al., "Deterministic generation of single soliton Kerr frequency comb in microresonators by a single shot pulsed trigger," *Opt. Express*, Vol. 26, No. 14, 18563–18577, 2018.
119. Coen, S., H. G. Randle, T. Sylvestre, et al., "Modeling of octave-spanning Kerr frequency combs using a generalized mean-field Lugiato-Lefever model," *Opt. Lett.*, Vol. 38, 37–39, 2013.
120. Lau, R. K. W., M. R. E. Lamont, Y. Okawachi, et al., "Effects of multiphoton absorption on parametric comb generation in silicon microresonators," *Opt. Lett.*, Vol. 40, No. 12, 2778–2781, 2015.
121. Bao, C., L. Zhang, L. C. Kimerling, et al., "Soliton breathing induced by stimulated Raman scattering and self-steepening in octave-spanning Kerr frequency comb generation," *Opt. Express*, Vol. 23, No. 14, 18665–18670, 2015.
122. Liu, X., C. Sun, B. Xiong, et al., "Generation of multiple near-visible comb lines in an AlN microring via $\chi^{(2)}$ and $\chi^{(3)}$ optical nonlinearities," *Appl. Phys. Lett.*, Vol. 113, No. 17, 171106, 2018.
123. Wang, L., L. Chang, N. Volet, et al., "Frequency comb generation in the green using silicon nitride microresonators," *Laser & Photonics Rev.*, Vol. 10, No. 4, 631–638, 2016.

124. Guo, X., C.-L. Zou, H. Jung, et al., "Efficient generation of a near-visible frequency comb via Cherenkov-like radiation from a Kerr microcomb," *Phys. Rev. Appl.*, Vol. 10, No. 1, 014012, 2018.
125. Lee, S. H., D. Y. Oh, Qi-Fan Yang, et al., "Towards visible soliton microcomb generation," *Nat. Commun.*, Vol. 8, No. 1, 1295, 2017.
126. Raja, A. S., A. S. Voloshin, H. Guo, et al., "Electrically pumped photonic integrated soliton microcomb," *Nat. Commun.*, Vol. 10, No. 1, 1–16, 2019.
127. Briles, T. C., S.-P. Yu, T. E. Drake, et al., "Generating octave-bandwidth soliton frequency combs with compact, low-power semiconductor lasers," *Phys. Rev. Appl.*, Vol. 14, No. 1, 014006, 2020.
128. Fujii, L., M. Inga, J. H. Soares, et al., "Dispersion tailoring in wedge microcavities for Kerr comb generation," *Opt. Lett.*, Vol. 45, No. 12, 3232–3235, 2020.
129. Yu, M., Y. Okawachi, A. G. Griffith, et al., "Mode-locked mid-infrared frequency combs in a silicon microresonator," *Optica*, Vol. 3, No. 8, 854–860, 2016.
130. Yu, M., Y. Okawachi, A. G. Griffith, et al., "Silicon-chip-based mid-infrared dual-comb spectroscopy," *Nat. Commun.*, Vol. 9, No. 1, 1869, 2018.
131. Yu, M., Y. Okawachi, A. G. Griffith, et al., "Microfluidic mid-infrared spectroscopy via microresonator-based dual-comb source," *Opt. Lett.*, Vol. 44, No. 17, 4259–4262, 2019.
132. Gong, Z., X. Liu, Y. Xu, et al., "Soliton microcomb generation at 2 μm in z-cut lithium niobate microring resonators," *Opt. Lett.*, Vol. 44, No. 12, 3182, 2019.
133. Guo, Y., J. Wang, Z. Han, et al., "Power-efficient generation of two-octave mid-IR frequency combs in a germanium microresonator," *Nanophotonics*, Vol. 7, No. 8, 1461–1467, 2018.
134. Fan, W., Z. Lu, W. Li, et al., "Low-threshold 4/5 octave-spanning mid-infrared frequency comb in a $LiNbO_3$ microresonator," *IEEE Photonics J.*, Vol. 11, No. 6, 1–7, 2019.
135. Anashkina, E. A., M. P. Marisova, A. A. Sorokin, et al., "Numerical simulation of mid-infrared optical frequency comb generation in chalcogenide As_2S_3 microbubble resonators," *Photonics*, Vol. 6, No. 2, 55, 2019.
136. Lamb, E. S., D. R. Carlson, D. D. Hickstein, et al., "Optical-frequency measurements with a Kerr-microcomb and photonic-chip supercontinuum," *Phys. Rev. Appl.*, Vol. 9, No. 2, 024030, 2018.
137. Signorini, S., S. Piccione, M. Ghulinyan, et al., "Are on-chip heralded single photon sources possible by intermodal four wave mixing in silicon waveguides," *Quantum Photonic Devices*, Vol. 10733, 107330G, 2018.
138. Signorini, S., M. Mancinelli, M. Borghi, et al., "Intermodal four-wave mixing in silicon waveguides," *Photon. Res.*, Vol. 6, No. 8, 805–814, 2018.
139. Lacava, C., M. A. Ettabib, T. D. Bucio, et al., "Intermodal bragg-scattering four wave mixing in silicon waveguides," *J. Lightw. Technol.*, Vol. 37, No. 7, 1680–1685, 2019.
140. Lacava, C., T. D. Bucio, A. Z. Khokhar, et al., "Intermodal frequency generation in silicon-rich silicon nitride waveguides," *Photon. Res.*, Vol. 7, 615–621, 2019.
141. Guo, H., E. Lucas, M. H. P. Pfeiffer, et al., "Intermode breather solitons in optical microresonators," *Phys. Rev. X*, Vol. 7, No. 4, 041055, 2017.
142. Boscolo, S., A. I. Latkin, and S. K. Turitsyn, "Passive nonlinear pulse shaping in normally dispersive fiber systems," *J. Quantum Elect.*, Vol. 44, No. 12, 1196–1203, 2008.
143. Boscolo, S. and C. Finot, "Nonlinear pulse shaping in fibers for pulse generation and optical processing," *International Journal of Optics*, 2012, DOI: 10.1155/2012/159057.
144. Luo, A., M. Liu, X. Wang, et al., "Few-layer MoS_2-deposited microfiber as highly nonlinear photonic device for pulse shaping in a fiber laser," *Photon. Res.*, Vol. 3, No. 2, A69–A78, 2015.
145. Boscolo, S. and C. Finot, "Artificial neural networks for nonlinear pulse shaping in optical fibers," arXiv preprint arXiv:2002.08815, 2020.
146. Boscolo, S. and C. Finot, "Nonlinear pulse shaping in optical fibres with a neural network," *Nonlinear Photonics*, NpTu1E. 1, Optical Society of America, 2020.

147. Ataie, V., E. Myslivets, B. P.-P. Kuo, et al., "Spectrally equalized frequency comb generation in multistage parametric mixer with nonlinear pulse shaping," *J. Lightw. Technol.*, Vol. 32, No. 4, 840–846, 2014.
148. Weiner, A. M., "Ultrafast optical pulse shaping: A tutorial review," *Opt. Commun.*, Vol. 284, No. 15, 3669–3692, 2011.
149. Wang, D., L. Huo, Q. Wang, et al., "Performance optimization of ultra-short optical pulse generation based on Mamyshev reshaping and its application in 100-Gb/s and 200-Gb/s optical time-division multiplexing," *Opt. Commun.*, Vol. 364, 76–82, 2016.
150. Mitrofanov, A. V., D. A. Sidorov-Biryukov, M. M. Nazarov, et al., "Ultraviolet-to-millimeter-band supercontinua driven by ultrashort mid-infrared laser pulses," *Optica*, Vol. 7, No. 1, 15–19, 2020.
151. Maiuri, M., M. Garavelli, and G. Cerullo, "Ultrafast spectroscopy: State of the art and open challenges," *J. Am. Chem. Soc.*, Vol. 142, No. 1, 3–15, 2019.
152. Mitra, K. and S. Miller, *Short Pulse Laser Systems for Biomedical Applications*, Springer, Germany, 2017.
153. Treacy, E., "Optical pulse compression with diffraction gratings," *IEEE J. Quant. Electron.*, Vol. 5, No. 9, 454–458, 1969.
154. Mei, C., K. Wang, J. Yuan, et al., "Self-similar propagation and compression of the parabolic pulse in silicon waveguide," *J. Lightw. Technol.*, Vol. 37, No. 9, 1990–1999, 2019.
155. Tan, D. T. H., P. C. Sun, and Y. Fainman, "Monolithic nonlinear pulse compressor on a silicon chip," *Nat. Commun.*,, Vol. 1, No. 1, 1–6 2010.
156. Colman, P., C. Husko, S. Combrié, et al., "Temporal solitons and pulse compression in photonic crystal waveguides," *Nat. Photon.*, Vol. 4, No. 12, 862–868, 2010.
157. Sahin, E., A. Blanco-Redondo, P. Xing, et al., "Bragg soliton compression and fission on CMOS-compatible ultra-silicon-rich nitride," *Laser & Photon. Rev.*, Vol. 13, 1900114, 2019.
158. Choi, J. W., B. U. Sohn, G. F. R. Chen, et al., "Sub-ps optical pulse compression in ultra-silicon-rich nitride waveguides," *Nonlinear Optics*, NM3B. 4, OSA, 2019.
159. Redondo, A. B., C. Husko, D. Eades, et al., "Observation of soliton compression in silicon photonic crystals," *Nat. Commun.*, Vol. 5, No. 1, 1–8, 2014.
160. Amine, B. S., C. Rim, and Z. Mourad, "Soliton-self compression in highly nonlinear chalcogenide photonic nanowires with ultralow pulse energy," *Opt. Express*, Vol. 19, No. 21, 19955–19966, 2011.
161. Lavdas, S., J. B. Driscoll, R. R. Grote, et al., "Pulse compression in adiabatically tapered silicon photonic wires," *Opt. Express*, Vol. 22, No. 6, 6296–6312, 2014.
162. Li, Q., P. K. A. Wai, K. Senthilnathan, et al., "Modeling self-similar optical pulse compression in nonlinear fiber Bragg grating using coupled-mode equations," *J. Lightw. Technol.*, Vol. 29, No. 9, 1293–1305, 2011.
163. Kruglov, V. I., A. C. Peacock, and J. D. Harvey, "Exact solutions of the generalized nonlinear Schrödinger equation with distributed coefficients," *Phys. Rev. E*, Vol. 71, No. 5, 056619, 2005.
164. Li, F., Q. Li, J. Yuan, et al., "Highly coherent supercontinuum generation with picosecond pulses by using self-similar compression," *Opt. Express*, Vol. 22, No. 22, 27339–27354, 2014.
165. Mei, C., F. Li, J. Yuan, et al., "High degree picosecond pulse compression in chalcogenide-silicon slot waveguide taper," *J. Lightw. Technol.*, Vol. 34, No. 16, 3843–3852, 2016.
166. Huang, J., M. S. A. Gandhi, and Q. Li, "Self-similar chirped pulse compression in the tapered silicon ridge slot waveguide," *IEEE J. Sel. Top. Quant. Electron.*, Vol. 26, No. 2, 1–8, 2019.
167. Yuan, J., J. Chen, F. Li, et al., "Mid-infrared self-similar compression of picosecond pulse in an inversely tapered silicon ridge waveguide," *Opt. Express*, Vol. 25, No. 26, 33439–33450, 2017.
168. Cheng, Y., J. Yuan, C. Mei, et al., "Self-similar picosecond pulse compression for supercontinuum generation at mid-infrared wavelength in silicon strip waveguides," *Opt. Commun.*, Vol. 454, 124380, 2020.
169. Kang, Z., J. Yuan, S. Li, et al., "Six-bit all-optical quantization using photonic crystal fiber with soliton self-frequency shift and pre-chirp spectral compression techniques," *Chinese Phys. B*, Vol. 22, No. 11, 114211, 2013.

170. Huber, R., M. Wojtkowski, and J. G. Fujimoto, "Fourier Domain Mode Locking (FDML, A new laser operating regime and applications for optical coherence tomography," *Opt. Express*, Vol. 14, No. 8, 3225–3237, 2006.
171. Andresen, E. R., V. Birkedal, J. Thøgersen, et al., "Tunable light source for coherent anti-Stokes Raman scattering micro spectroscopy based on the soliton self-frequency shift," *Opt. Lett.*, Vol. 31, No. 9, 1328–1330, 2006.
172. Chuang, H. P. and C. B. Huang, "Wavelength-tunable spectral compression in a dispersion-increasing fiber," *Opt. Lett.*, Vol. 36, No. 15, 2848–2850, 2011.
173. Andresen, E. R., J. Thøgersen, and S. R. Keiding, "Spectral compression of femtosecond pulses in photonic crystal fibers," *Opt. Lett.*, Vol. 30, No. 15, 2025–2027, 2005.
174. Mei, C., J. Yuan, K. Wang, et al., Chirp-free spectral compression of parabolic pulses in silicon nitride channel waveguides," *2016 21st Opto Electronics and Communications Conference (OECC) held jointly with 2016 International Conference on Photonics in Switching (PS)*, 1–3, IEEE, 2016.
175. Mei, C., J. Yuan, F. Li, et al., "Efficient spectral compression of wavelength-shifting soliton and its application in integratable all-optical quantization," *IEEE Photonics J.*, Vol. 11, No. 1, 1–15, 2019.
176. Cheng, Y., J. Yuan, C. Mei, et al., "Mid-infrared spectral compression of soliton pulse in an adiabatically suspended silicon waveguide taper," *IEEE Photonics J.*, Vol. 11, No. 4, 4500911, 2019.
177. Fermann, M. E., V. I. Kruglov, B. C. Thomsen, et al., "Self-similar propagation and amplification of parabolic pulses in optical fibers," *Phys. Rev. Lett.*, Vol. 84, No. 26, 6010, 2000.
178. Limpert, J., T. Schreiber, T. Clausnitzer, et al., "High-power femtosecond Yb-doped fiber amplifier," *Opt. Express*, Vol. 10, No. 14, 628–638, 2002.
179. Ozeki, Y., Y. Takushima, K. Aiso, et al., "High repetition-rate similariton generation in normal dispersion erbium-doped fiber amplifiers and its application to multi-wavelength light sources," *IEICE T. Electron.*, Vol. 88, No. 5, 904–911, 2005.
180. Finot, C.. G. Millot, C. Billet, et al., "Experimental generation of parabolic pulses via Raman amplification in optical fiber," *Opt. Express*, Vol. 11, No. 13, 1547–1552, 2003.
181. Boscolo, S., A. I. Latkin, and S. K. Turitsyn, "Passive nonlinear pulse shaping in normally dispersive fiber systems," *IEEE J. Quant. Electron.*, Vol. 44, No. 12, 1196–1203, 2008.
182. Kruglov, V. I. and J. D. Harvey, "Asymptotically exact parabolic solutions of the generalized nonlinear Schrödinger equation with varying parameters," *J. Opt. Soc. Am. B*, Vol. 23, No. 12, 2541–2550, 2006.
183. Hirooka, T. and M. Nakazawa, "Parabolic pulse generation by use of a dispersion-decreasing fiber with normal group-velocity dispersion," *Opt. Lett.*, Vol. 29, No. 5, 498–500, 2004.
184. Jiang, G., Y. Fu, Y. Huang, et al., "Generation of the self-similar parabolic pulses by designing comb-like profiled dispersion fiber based on alternately arranged single-mode fibers and dispersion-shifted fibers," *Optik*, Vol. 124, 5328–5331, 2013.
185. Finot, C., L. Provost, P. Petropoulos, et al., "Parabolic pulse generation through passive nonlinear pulse reshaping in a normally dispersive two segment fiber device," *Opt. Express*, Vol. 15, No. 3, 852–864, 2007.
186. Lavdas, S., J. B. Driscoll, H. Jiang, et al., "Generation of parabolic similaritons in tapered silicon photonic wires: Comparison of pulse dynamics at telecom and mid-infrared wavelengths," *Opt. Lett.*, Vol. 38, No. 19, 3953–3956, 2013.
187. Lavdas, S., J. B. Driscoll, et al., "Generation and collision of optical similaritons in dispersion-engineered silicon photonic nanowires," *Nanoengineering: Fabrication, Properties, Optics, and Devices X. International Society for Optics and Photonics*, Vol. 8816, 8816DJ, 2013.
188. Mei, C., F. Li, J. Yuan, et al., "Comprehensive analysis of passive generation of parabolic similaritons in tapered hydrogenated amorphous silicon photonic wires," *Sci. Rep.*, Vol. 7, No. 1, 3814-1-14, 2017.

189. Mei, C., J. Yuan, F. Li, et al., "Generation of parabolic pulse in a dispersion and nonlinearity jointly engineered silicon waveguide taper," *Opt. Commun.*, Vol. 448, 48–54, 2019.
190. Mei, C., J. Yuan, F. Li, et al., "Passive generation of the multi-wavelength parabolic pulses in tapered silicon nanowires," *IEEE Access*, Vol. 8, 77631–77641, 2020.
191. Jones, N., "How to stop data centres from gobbling up the world's electricity," *Nature*, Vol. 561, No. 7722, 163–167, 2018.
192. Minzioni, P., C. Lacava, T. Tanabe, et al., "Roadmap on all-optical processing," *J. Opt.*, Vol. 21, No. 6, 063001, 2019.
193. Willner, A. E., D. Gurkan, A. B. Sahin, et al., "All-optical address recognition for optically-assisted routing in next-generation optical networks," *IEEE Commun. Mag.*, Vol. 41, No. 5, S38–S44, 2003.
194. Mahjoubfar, A., D. V. Churkin, S. Barland, et al., "Time stretch and its applications," *Nat. Photon.*, Vol. 11, No. 6, 341, 2017.
195. Kang, Z., X. Zhang, J. Yuan, et al., "Resolution-enhanced all-optical analog-to-digital converter employing cascade optical quantization operation," *Opt. Express*, Vol. 22, No. 18, 21441–21453, 2014.
196. Tian, Y., J. Qiu, Z. Huang, et al., "On-chip integratable all-optical quantizer using cascaded step-size MMI," *Opt. Express*, Vol. 26, No. 3, 2453–2461, 2018.
197. Valley, G. C., "Photonic analog-to-digital converters," *Opt. Express*, Vol. 15, No. 5, 1955–1982, 2007.
198. Miyoshi, Y., S. Namiki, and K. I. Kitayama, "Performance evaluation of resolution-enhanced ADC using optical multiperiod transfer functions of NOLMs," *IEEE Journal of Selected Topics in Quantum Electronics*, Vol. 18, No. 2, 779–784, 2012.
199. Andrekson, P. A. and M. Westlund, "Nonlinear optical fiber based high resolution all-optical waveform sampling," *Laser & Photonics Rev.*, Vol. 1, No. 3, 231–248, 2007.
200. Nuño, J., M. Gilles, M. Guasoni, et al., "All-optical sampling and magnification based on XPM-induced focusing," *Opt. Express*, Vol. 24, No. 22, 24921–24929, 2016.
201. Nishitani, T., T. Konishi, and K. Itoh, "Resolution improvement of all-optical analog-to-digital conversion employing self-frequency shift and self-phase-modulation-induced spectral compression," *IEEE J. Sel. Top. Quant. Electron.*, Vol. 14, No. 3, 724–732, 2008.
202. Li, Y., K. Zhu, Z. Kang, et al., "CMOS-compatible high-index doped silica waveguide with an embedded silicon-nanocrystal strip for all-optical analog-to-digital conversion," *Photon. Res.*, Vol. 7, No. 10, 1200–1208, 2019.
203. Bres, C. S., N. Alic, A. H. Gnauck, et al., "Multicast parametric synchronous sampling," *IEEE Photon. Technol. Lett.*, Vol. 20, No. 14, 1222–1224, 2008.
204. Miao, B., C. Chen, A. Sharkway, et al., "Two-bit optical analog-to-digital converter based on photonic crystals," *Opt. Express*, Vol. 14, No. 17, 7966–7973, 2006.
205. Kang, Z., J. Yuan, X. Zhang, et al., "On-chip integratable all-optical quantizer using strong cross-phase modulation in a silicon-organic hybrid slot waveguide," *Sci. Rep.*, Vol. 6, No. 1, 1–12, 2016.
206. Kang, Z., J. Yuan, X. Zhang, et al., "CMOS-compatible 2-bit optical spectral quantization scheme using a silicon-nanocrystal-based horizontal slot waveguide," *Sci. Rep.*, Vol. 4, No. 1, 1–9, 2014.
207. Kang, S., J. Yuan, Z. Kang, et al., "All-optical quantization scheme by slicing the supercontinuum in a chalcogenide horizontal slot waveguide," *J. Opt.*, Vol. 17, No. 8, 085502, 2015.
208. Kang, X., J. Yuan, Z. Kang Z, et al., "Integratable all-optical spectral quantization scheme based on chalcogenide-silicon slot waveguide," *Opt. Commun.*, Vol. 355, 479–484, 2015.
209. Zhang, J., K. Wang, J. Yuan, et al., "All-optical spectral quantization scheme based on cascaded chalcogenide-silicon slot waveguides," *Opt. Eng.*, Vol. 57, No. 4, 045102, 2018.
210. Keyes, R. W., "Optical logic-in the light of computer technology," *Optica Acta: Int. J. Opt.*, Vol. 32, No. 5, 525–535, 1985.
211. Tsuda, H. and T. Kurokawa, "Construction of an all-optical flip-flop by combination of two optical triodes," *Appl. Phys. Lett.*, Vol. 57, No. 17, 1724–1726, 1990.

212. Wang, J. M., M, Luo, Y, Qiu et al., "Dual-channel AND logic gate based on four-wave mixing in a multimode silicon waveguide," *IEEE Photonics J.*, Vol. 9, No. 4, 1–6, 2017.
213. Wu, W., Q. B. Sun, L. R. Wang, et al., "Influence of two-photon absorption and free-carrier effects on all-optical logic gates in silicon waveguides," *Appl. Phys. Express*, Vol. 12, 042005, 2019.
214. Moroney, N., L. D. Bino, M. T. M. Woodley, et al., "Logic gates based on interaction of counterpropagating light in microresonators," *J. Lightw. Technol.*, Vol. 38, No. 6, 1414–1419, 2020.
215. Jandieri, V., R. Khomeriki, and D. Erni, "Realization of true all-optical AND logic gate based on nonlinear coupled air-hole type photonic crystal waveguides," *Opt. Express*, Vol. 26, No. 16, 19845–19853, 2018.
216. Kumar, S. and M. Sen, "Integrable all-optical NOT gate using nonlinear photonic crystal MZI for photonic integrated circuit," *J. Opt. Soc. Am. B*, Vol. 37, No. 2, 359–369, 2020.
217. Vakhtang, J., K. Ramaz, O. Tornike, et al., "Functional all-optical logic gates for true time-domain signal processing in nonlinear photonic crystal waveguides," *Opt. Express*, Vol. 28, No. 12, 18317–18331, 2020.
218. Dimitriadou, E. and K. E. Zoiros, "All-optical XOR gate using single quantum-dot SOA and optical filter," *J. Lightw. Technol.*, Vol. 31, No. 23, 3813–3821, 2013.
219. Kotb, A., K. E. Zoiros, and C. Guo, "1 Tb/s all-optical XOR and AND gates using quantum-dot semiconductor optical amplifier-based turbo-switched Mach-Zehnder interferometer," *J. Comput. Electron.*, Vol. 18, No. 2, 628–639, 2019.
220. Capmany, J. and D. Novak, "Microwave photonics combines two worlds," *Nat. Photon.*, Vol. 1, No. 6, 319–330, 2007.
221. Supradeepa, V. R., et al., "Comb-based radio frequency photonic filters with rapid tunability and high selectivity," *Nat. Photon.*, Vol. 6, No. 3, 186–194, 2012.
222. Li, J., H. Lee, T. Chen, et al., "Low-pump-power, low-phase-noise, and microwave to millimeter-wave repetition rate operation in microcombs," *Phys. Rev. Lett.*, Vol. 109, No. 23, 233901, 2012.
223. Liang, W., D. Eliyahu, V. S. Ilchenko, et al., "High spectral purity Kerr frequency comb radio frequency photonic oscillator," *Nat. Commun.*, Vol. 6, No. 1, 1–8, 2015.
224. Nguyen, T. G., M. Shoeiby, S. T. Chu, et al., "Integrated frequency comb source based Hilbert transformer for wideband microwave photonic phase analysis," *Opt. Express*, Vol. 23, No. 17, 22087–22097, 2015.
225. Xue, X., Y. Xuan, H. J. Kim, et al., "Programmable single-bandpass photonic RF filter based on Kerr comb from a microring," *J. Light. Technol.*, Vol. 32, No. 20, 3557–3565, 2014.
226. Xu, X., J. Wu, T. G. Nguyen, et al., "Photonic microwave true time delays for phased array antennas using a 49 GHz FSR integrated optical micro-comb source," *Photon. Res.*, Vol. 6, No. 5, B30–B36, 2018.
227. Wu, J., X. Xu, T. G. Nguyen, et al., "RF photonics: An optical microcombs' perspective," *IEEE J. Sel. Top. Quant. Electron.*, Vol. 24, No. 4, 1–20, 2018.
228. Xu, X., J. Wu, T. G. Nguyen, et al., "Broadband RF channelizer based on an integrated optical frequency Kerr comb source," *J. Lightw. Technol.*, Vol. 36, No. 19, 4519–4526, 2018.
229. Hu, J., J. He, J. Liu, et al., "Reconfigurable radiofrequency filters based on versatile soliton microcombs," *Nat. Commun.*, Vol. 11, No. 1, 1–9, 2020.
230. Yu, X., B. Ding, H. Lu, et al., "Third-order optical nonlinearity in nonstoichiometric amorphous silicon carbide films," *J. Alloy. Compd.*, Vol. 794, 518–524, 2019.
231. Tumuluri, A., M. S. S. Bharati, S. V. Rao, et al., "Structural, optical and femtosecond third-order nonlinear optical properties of $LiNbO_3$ thin films," *Mater. Res. Bull.*, Vol. 94, 342–351, 2017.
232. Sierra, J. H., R. C. Rangel, R. E. Samad, et al., "Low-loss pedestal Ta_2O_5 nonlinear optical waveguides," *Opt. Express*, Vol. 27, No. 26, 37516–37521, 2019.
233. Zhang, L., Q. Lin, Y. Yue, et al., "Silicon waveguide with four zero-dispersion wavelengths and its application in on-chip octave-spanning supercontinuum generation," *Opt. Express*, Vol. 20, No. 2, 1685–1690, 2012.

234. Guo, Y., Z. Jafari, L. J. Xu, et al., "Ultra-flat dispersion in an integrated waveguide with five and six zero-dispersion wavelengths for mid-infrared photonics," *Photon. Res.*, Vol. 7, No. 11, 1279–1286, 2019.

235. Shao, L.. M. Yu, S. Maity, et al., "Microwave-to-optical conversion using lithium niobate thin-film acoustic resonators," *Optica*, Vol. 6, No. 12, 1498–1505, 2019.

236. Chauvet, M., F. Henrot, L. Gauthier-Manuel, et al., "Periodically poled $LiNbO_3$ ridge waveguides on silicon for second-harmonic generation," *Silicon Photonics and Photonic Integrated Circuits V. International Society for Optics and Photonics*, Vol. 9891, 98910S, 2016.

237. Autere, A., H. Jussila, Y. Dai, et al., "Nonlinear optics with 2D layered materials," *Adv. Mater.*, Vol. 30, No. 24, 1705963, 2018.

238. Alam, M. Z., I. De Leon, and R. W. Boyd, "Large optical nonlinearity of indium tin oxide in its epsilon-near-zero region," *Science*, Vol. 352, No. 6287, 795–797, 2016.

239. Kauranen, M. and A. V. Zayats, "Nonlinear plasmonics," *Nat. Photon.*, Vol. 6, No. 11, 737, 2012.

240. Feng, M., H. Zhan, and Y. Chen, "Nonlinear optical and optical limiting properties of graphene families," *Appl. Phys. Lett.*, Vol. 96, No. 3, 033107, 2010.

241. Liu, Z., Y. Wang, X. Zhang, et al., "Nonlinear optical properties of graphene oxide in nanosecond and picosecond regimes," *Appl. Phys. Lett.*, Vol. 94, No. 2, 021902, 2009.

242. Liu, L., K. Xu, X. Wan, et al., "Enhanced optical Kerr nonlinearity of MoS_2 on silicon waveguides," *Photon. Res.*, Vol. 3, No. 5, 206–209, 2015.

243. Alam, M. Z., S. A. Schulz, J. Upham, et al., "Large optical nonlinearity of nanoantennas coupled to an epsilon-near-zero material," *Nat. Photon.*, Vol. 12, No. 2, 79–83, 2018.

244. Neira, A. D., N. Olivier, M. E. Nasir, et al.,"Eliminating material constraints for nonlinearity with plasmonic metamaterials," *Nat. Commun.*, Vol. 6, No. 1, 1–8, 2015.

245. Li, G., S. Zhang, and T. Zentgraf, "Nonlinear photonic metasurfaces," *Nat. Rev. Mater.*, Vol. 2, No. 5, 1–14, 2017.

246. Lee, J., M. Tymchenko, C. Argyropoulos, et al., "Giant nonlinear response from plasmonic metasurfaces coupled to intersubband transitions," *Nature*, Vol. 511, No. 7507, 65–69, 2014.

247. Horak, P. and F. Poletti, "Multimode nonlinear fibre optics: theory and applications," *Recent Progress in Optical Fiber Research*, 3–25, 2012.

248. Gloge, D. and E. A. J. Marcatili, "Multimode theory of graded-core fibers," *Bell System Technical Journal*, Vol. 52, No. 9, 1563–1578, 1973.

249. Wright, L. G., D. N. Christodoulides, and F. W. Wise, "Controllable spatiotemporal nonlinear effects in multimode fibres," *Nat. Photon.*, Vol. 9, No. 5, 306–310, 2015.

250. Renninger, W. H. and F. W. Wise, "Optical solitons in graded-index multimode fibres," *Nat. Commun.*, Vol. 4, No. 1, 1–6, 2013.

251. Krupa, K., A. Tonello, B. M. Shalaby, et al., "Spatial beam self-cleaning in multimode fibres," *Nat. Photon.*, Vol. 11, No. 4, 237–241, 2017.

252. Demas, J., P. Steinvurzel, B. Tai, et al., "Intermodal nonlinear mixing with Bessel beams in optical fiber," *Optica*, Vol. 2, No. 1, 14–17, 2015.

253. Wright, L. G., S. Wabnitz, D. N. Christodoulides, et al., "Ultrabroadband dispersive radiation by spatiotemporal oscillation of multimode waves," *Phys. Rev. Lett.*, Vol. 115, No. 22, 223902, 2015.

254. Krupa, K., A. Tonello, A. Barthélémy, et al., "Observation of geometric parametric instability induced by the periodic spatial self-imaging of multimode waves," *Phys. Rev. Lett.*, Vol. 116, No. 18, 183901, 2016.

255. Elshaari, A. W., W. Pernice, K. Srinivasan, et al., "Hybrid integrated quantum photonic circuits," *Nat. Photon.*, Vol. 14, 285–298, 2020.

256. Singh, A., Q. Li, S. Liu, Y. Yu, X. Lu, C. Schneider, et al., "Quantum frequency conversion of a quantum dot single-photon source on a nanophotonic chip," *Optica*, Vol. 6, No. 5, 563–569, 2019.